

Study of the reaction $p_1 p \rightarrow p \pi^+ n$ with polarized beam from 1.18 to 1.98 GeV/c

A. B. Wicklund, M. W. Arenton,* D. S. Ayres, R. Diebold, E. N. May,
L. J. Nodulman, and J. R. Sauer†
Argonne National Laboratory, Argonne, Illinois 60439

E. C. Swallow
Elmhurst College, Elmhurst, Illinois 60126

M. M. Calkin,‡ M. D. Corcoran, J. Hoftiezer,§ H. E. Miettinen, and G. S. Mutchler
Rice University, Houston, Texas 77251
(Received 29 September 1986)

We present density-matrix elements and single-spin correlations for the reaction $p_1 p \rightarrow p \pi^+ n$ at 1.18, 1.47, 1.71, and 1.98 GeV/c, using both longitudinal and transverse beam polarizations. For the $p_1 p \rightarrow \Delta^{++} n$ subprocess we find quite different energy dependence for the helicity- $\frac{1}{2}$ and helicity- $\frac{3}{2}$ Δ^{++} -production asymmetries. The helicity- $\frac{1}{2}$ asymmetry has p_{lab} dependence similar to the polarization in $p_1 p \rightarrow \pi^+ d$, while the helicity- $\frac{3}{2}$ asymmetry changes sign between 1.18 and 1.47 GeV/c. By fitting the production angle dependence of the spin correlations, we obtain joint moments which are easily related to the partial-wave structure. We have carried out a partial-wave analysis with the moments data. We find that the production wave intensities are qualitatively consistent with the elastic phase-shift analyses, and the phases vary smoothly with p_{lab} . From the absence of Breit-Wigner phase behavior, we conclude that the dinucleon resonances seen in the pp elastic waves are not true coupled-channel Breit-Wigner states in NN and $N\Delta$.

I. INTRODUCTION

Medium-energy nucleon-nucleon interactions have been the focus of renewed interest in recent years, largely due to the observation of resonancelike structures in the proton-proton elastic waves.¹ These "dibaryon resonances," which appear as half loops in the Argand plots, seem to occur only in channels which have strong inelastic couplings (the 1D_2 and 3F_3 channels, in particular). Consequently, clarification of the nature of these "resonances" requires systematic studies of the inelastic reactions at intermediate energies. In this paper we describe experimental results from such a study; we present a complete set of density-matrix elements (DME's) and single-spin correlations (SSC's) for the reaction

$$p_1 p \rightarrow p \pi^+ n, \quad (1)$$

together with the results of a partial-wave analysis.

The experiment was carried out with the Effective Mass Spectrometer (EMS), using the polarized proton beam from the Argonne Zero-Gradient Synchrotron (ZGS). Data were taken at 1.18, 1.47, 1.71, and 1.98 GeV/c, corresponding to kinetic energies of 0.57, 0.81, 1.01, and 1.25 GeV; the results are based on statistics of 200 000, 758 000, 742 000, and 686 000 events, respectively, at these energies, and include both longitudinal and transverse spin correlations. Similar data, restricted to

forward Δ^{++} production ($-t \leq 1.5 \text{ GeV}^2$), were obtained in a companion experiment from 3 to 12 GeV/c (Ref. 2). Together these data describe the evolution of the quasi-two-body reaction

$$p_1 p \rightarrow \Delta^{++} n \quad (2)$$

from the "resonance" region to the high-energy domain.

A complete description of $p_1 p \rightarrow p \pi^+ n$, including non- Δ^{++} contributions (from nonresonant S - and P -wave $p \pi^+$ isobars), requires a total of 18 DME's and SSC's for each bin in $M_{p \pi^+}$ and Θ_Δ , where Θ_Δ denotes the center-of-mass (c.m.) production angle for the $p \pi^+$ system. Therefore, the EMS experiment was designed to cover a broad range in Δ^{++} mass and decay angles, and 0° to 180° in Θ_Δ . The full Θ_Δ coverage is especially important because it permits expansion of each of the DME's and SSC's in functions of $\cos \Theta_\Delta$. The resulting expansion coefficients ("joint moments") give an economical description of the data, and are simply related to products of partial waves.

Previous bubble-chamber experiments^{3,4} have obtained cross sections and DME's for $pp \rightarrow p \pi^+ n$ in this energy range, albeit with limited statistics. In addition, high-statistics data have recently become available on one- and two-spin correlations,⁵⁻⁹ but these data tend to cover limited kinematical ranges and do not permit isolation of a complete set of SSC's and joint moments. Although these

measurements have been compared with theoretical predictions with varying degrees of success, it is our view that a more systematic approach, leading to a phenomenological partial-wave expansion, is needed both to isolate the behavior of the “resonant” waves and to facilitate more comprehensive theoretical comparisons.

Regarding the goals of a partial-wave analysis, we remark that the effects of a dibaryon resonance should be quite spectacular and easily identifiable in $p_1 p \rightarrow p \pi^+ n$. Specifically, if the dibaryons behave like coupled-channel Breit-Wigner resonances, then (1) they must couple strongly to the ΔN channel by unitarity and (2) they should give rise to $\sim 180^\circ$ phase advances in the $pp \rightarrow \Delta N$ waves. The first property signifies that they should be clearly visible in $pp \rightarrow \Delta N$; the second implies easily detectable effects in the energy dependence of the resonance candidates, which we take to be the 1D_2 and 3F_3 waves. Of course, the dibaryons need not behave like coupled-channel Breit-Wigner resonances; they may be due to threshold effects in $pp \rightarrow \Delta N$ or to virtual ΔN bound states. Theoretical interpretations have been advanced both with^{10–14} and without^{15–23} explicit coupled-channel resonances.

To justify these two expectations—the dominance of ΔN couplings and the 180° phase advance—in a little more detail, consider the hypothesis of Breit-Wigner behavior for the 1D_2 or 3F_3 waves. First, the elastic phase-shift analyses^{24–27} (PSA) suggest $\Gamma_{el}/\Gamma_{tot} \sim 0.2$ for these waves, and as a result the inelastic resonance cross sections $pp \rightarrow \text{dibaryon} \rightarrow NN\pi \rightarrow \dots$ must be several millibarns for a Breit-Wigner parametrization. In that case, given the known cross sections for $pp \rightarrow NN\pi$, $pp \rightarrow \Delta N$, and $pp \rightarrow NN\pi\pi$, consistency with unitarity would require the dominant couplings to be to the ΔN channel.²⁸ We note that at lower energies the reaction $pp \rightarrow d\pi^+$ could account for a substantial share of the 1D_2 inelasticity. However, it is clear from both energy²⁹ and spin dependence (see below) that deuteron formation occurs as a final-state interaction from the $pp \rightarrow NN\pi$ and $pp \rightarrow \Delta N$ channels. Thus the important physical partial-wave amplitudes are those for the dominant $pp \rightarrow \Delta N$ process, irrespective of whether the final-state nucleons are free or bound.

Retaining only the pp and ΔN channels, the 1D_2 and 3F_3 waves can be approximated by the familiar unitary parametrization

$$T = \begin{pmatrix} \frac{(\eta e^{2i\delta_{pp}} - 1)}{2i} & \frac{(1 - \eta^2)^{1/2}}{2} e^{i(\delta_{pp} + \delta_{\Delta N})} \\ \frac{(1 - \eta^2)^{1/2}}{2} e^{i(\delta_{pp} + \delta_{\Delta N})} & \frac{(\eta e^{2i\delta_{\Delta N}} - 1)}{2i} \end{pmatrix}. \quad (3)$$

The off-diagonal elements in Eq. (3) describe the $pp \rightarrow \Delta N$ transitions ${}^1D_2 \rightarrow {}^5S_2$ and ${}^3F_3 \rightarrow {}^5P_3$ (we ignore smaller transitions with D - and F -wave final states).³⁰ Two of the parameters in Eq. (3), η and δ_{pp} , are in principle known from the elastic PSA. In particular, from the behavior of $1 - \eta^2$, the inelastic 1D_2 and 3F_3 cross sections are known

to develop broad peaks near 600 and 800 MeV, respectively, which together account for 50 to 60% of the total inelastic rate. The third parameter in Eq. (3), $\delta_{\Delta N}$, cannot be obtained from the elastic PSA, but can only be determined by measuring the phase of the transition amplitude. In particular, it can be shown that in the case of a two-channel Breit-Wigner plus background parametrization, the transition phase is given by

$$\delta_{pp} + \delta_{\Delta N} = \phi_R + \delta_{pp}^B + \delta_{\Delta N}^B, \quad (4)$$

where ϕ_R [= $\arctan(M_R \Gamma / M_R^2 - M^2)$] is the Breit-Wigner phase and δ_{pp}^B and $\delta_{\Delta N}^B$ are phase shifts describing possible nonresonant background amplitudes.³¹ The 180° phase advance in ϕ_R should be reflected in a 180° advance in the transition phase. Since δ_{pp} is known to vary by only a few degrees over the 1D_2 and 3F_3 “resonances,” any strong energy dependence in the transition phase would have to come from $\delta_{\Delta N}$; for a Breit-Wigner parametrization, the $\sim 180^\circ$ phase advance in $\delta_{\Delta N}$ would be consistent with the constraint noted above that $\Gamma_{\Delta N}$ accounts for most of the resonance width. In the absence of two-channel Breit-Wigner behavior, for example, if the dibaryons are due to threshold effects or virtual bound states, both $\delta_{\Delta N}$ and the transition phase would be expected to vary little with energy or even decrease over the “resonance” width.³² We conclude that in the absence of experimental information on $\delta_{\Delta N}$, and with only the PSA data on η and δ_{pp} , it is *a priori* impossible to distinguish between conventional and Breit-Wigner resonance interpretations of the dibaryons. On the other hand, because of the dominance of the ΔN couplings, we can expect $\delta_{\Delta N}$ to behave quite differently for these two kinds of interpretations. Thus, the unknown phase behavior in $pp \rightarrow \Delta N$ forms the central motivation for our study.

In the remainder of this paper we present the measured DME’s and SSC’s, together with the formalism needed to carry out partial-wave analysis. The organization of the paper is as follows: Sec. II summarizes the experiment and data analysis; Sec. III covers the density matrix and joint moments formalism; Sec. IV reviews the measured DME’s and SSC’s as functions of $M_{p\pi^+}$ and Θ_Δ ; Sec. V is a digression on the empirical relation between $pp \rightarrow p\pi^+n$ and $pp \rightarrow \pi^+d$, and also on effects of proton-neutron final-state interactions; Sec. VI reviews the behavior of the joint moments; Sec. VII summarizes the results of partial-wave fits to the joint moments; and Sec. VIII concludes with a summary; additional formalism detailing our pion-exchange fits and $\Delta^+ - \Delta^{++}$ isobar interference are relegated to Appendices A and B.

II. EXPERIMENT AND DATA ANALYSIS

The Effective Mass Spectrometer, shown in Fig. 1, has been extensively described elsewhere.³³ For the present experiment, the salient aspects include the polarized beam transport system, which effectively allowed all three Cartesian components for the beam proton spin vector,

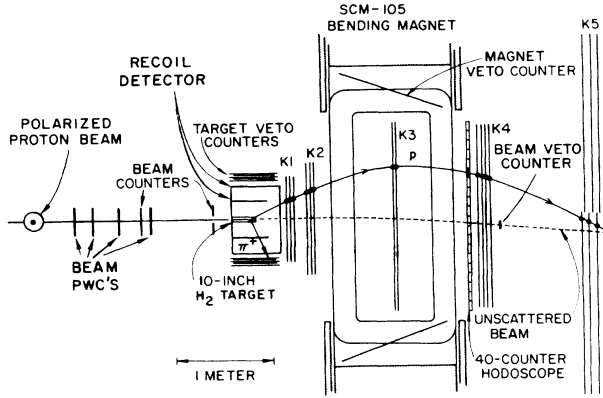


FIG. 1. Experimental plan view with typical $p\pi^+n$ event topology overlaid.

and the spectrometer itself, which included a large-aperture magnetic detector for forward tracks and a recoil detector for wide-angle tracks. The forward spectrometer used magnetostrictive spark chambers for track finding, while the recoil detector used proportional mode readout which was available at the trigger level. The recoil detector has been described elsewhere,³⁴ and its performance in other EMS experiments has been documented.³³ We proceed to summarize in turn the polarized beam, the trigger and event selection, and the extraction of acceptance-corrected angular distributions. More details on this experiment and analysis may be found in Ref. 35.

A. Polarized beam

The beam-transport system allowed both transverse and longitudinal spin directions at the hydrogen target. Primary beam protons, with polarization along the vertical direction, were extracted into the secondary beam line with a septum magnet, at a typical rate of 10^4 per 1-sec beam spill. A superconducting solenoid in the secondary beam line, in combination with the dipole bending magnets, could be used to obtain spin parallel or antiparallel to the beam direction at the hydrogen target, depending on solenoid polarity. Thus, the data taking involved a sequence of transverse (solenoid off), parallel, and antiparallel running. In addition, the proton spin was flipped on alternate accelerator cycles before injection into the ZGS; this rapid spin reversal minimized systematic errors in comparison of spin-up and -down counting rates.

The triggers included elastic scattering along with the inelastic events of interest. The left-right elastic asymmetries, measured during transverse running, were compared with existing elastic data³⁶ to obtain the beam polarizations: (56 ± 6) , (77 ± 6) , (77 ± 6) , and $(76 \pm 7)\%$, respectively, at 1.18, 1.42, 1.71, and 1.98 GeV/c (the errors are dominated by systematic uncertainties in the analyzing powers at these energies). To monitor the beam polarization during parallel and antiparallel running, a relative polarimeter located in the primary beam line was

used;³⁷ this was calibrated with the transverse data.

For the parallel and antiparallel running, the spin orientation was not precisely longitudinal at the hydrogen target. The deviation from longitudinal, expressed as a rotation angle in the horizontal plane, was calculated from the beam-transport geometry to be 25.4° , 13.7° , 3.6° , and -8.5° , respectively, at 1.18, 1.47, 1.71, and 1.98 GeV/c. The longitudinal spin correlations presented below have been corrected for this effect using appropriate combinations of parallel and transverse spin correlation measurements. The transverse correlations themselves are, of course, not affected by this complication.

B. Triggering and event selection

The information recorded by the EMS for each event included (1) the incident beam direction, using eight proportional-mode readout planes upstream from the target, (2) the direction and momentum of forward tracks (e.g., those with production angles from 0° to $\sim 45^\circ$) which traversed all or part of the spectrometer magnet, (3) the direction of "recoil" tracks (e.g., with production angles from $\sim 30^\circ$ to $\sim 160^\circ$) which traversed the recoil detector, and (4) additional tagging information from scintillation counters which surrounded the target and lined the upstream half of the spectrometer magnet; the target box provided a crude calorimeter to differentiate recoil charged particles, γ rays, and neutrons. Typical resolutions on the track measurements were 1 mrad on the beam direction, 1 mrad on forward-track directions, 0.5% on $\delta p/p$, and ± 15 mrad on the recoil direction.

The trigger scheme was designed to select two-prong events from the possible reactions

$$pp \rightarrow pp, \quad (5a)$$

$$pp \rightarrow \pi^+ d, \quad (5b)$$

$$pp \rightarrow p_f \pi_s^+(n), \quad (5c)$$

$$pp \rightarrow p_s \pi_f^+(n), \quad (5d)$$

$$pp \rightarrow pp(\pi^0), \quad (5e)$$

where we distinguish "fast" and "slow" like-charged tracks in the final states of interest (5c) and (5d). In addition, the two-prong triggers included background events from the reactions

$$pp \rightarrow pn \pi^+ \pi^0, pp \pi^0 \pi^0, nn \pi^+ \pi^+, d \pi^+ \pi^0 \quad (6)$$

and leakage from the four-prong topology

$$pp \rightarrow pp \pi^+ \pi^-. \quad (7)$$

Bubble-chamber surveys³ indicate that for 1.18, 1.47, and 1.71 GeV/c the two-pion background contaminations are negligible (less than 0.5% of the total cross section). At 1.98 GeV/c, reactions (6) make up $\sim 2.5\%$ of the total cross section; the four-prong reaction (5b) makes up $\sim 1.4\%$ of the total, but can be suppressed in software using the tracking and scintillation-counter information. Thus, we ignore the two-pion final states in the following discussion, keeping in mind that they may represent a few-percent background in the 1.98-GeV/c data.

The two-prong trigger made use of fast anode signals from the recoil detector, and scintillation signals from the 40-element hodoscope downstream from the magnet (see Fig. 1). In addition, all triggers required a good beam definition (based on beam-line aperture counters) and were in anticoincidence with a downstream beam-veto counter, which suppressed spurious triggers. Three coincidences were obtained from these trigger components: namely, two hodoscope hits, one hodoscope and one anode hit, and only one hodoscope hit. A countdown circuit was used to suppress the single hodoscope trigger. Each coincidence was designed to cover certain parts of phase space and to provide monitoring capability for possible biases in the other triggers. After event reconstruction the two-prong triggers consisted of two broad categories: (A) events with two forward momentum-analyzed charged tracks (mostly from triggers with two hodoscope hits), and (B) events with a single momentum-analyzed track and one wider angle track having only directional information (mostly from triggers with one hodoscope and one anode hit).

The events with two momentum-analyzed tracks ("type A") came almost entirely from reactions (5c)–(5e); the correct hypothesis was easily obtained from a one-constraint fit. For example, the missing-mass resolution for $pp \rightarrow p_1\pi_2^+(x)$ was ± 20 MeV or better on M_x , depending on energy. A very small fraction of these type-A events could be attributed to the $d\pi^+$ final state [reaction (5b)]; this gave a four-constraint fit, which was useful in checking the spectrometer alignment and energy-loss calculations. The type-A $pp \rightarrow p\pi^+(n)$ events also served to calibrate the behavior of recoil neutrons in the target scintillator box.

The majority of the events of interest, the "type-B" events having only one momentum-analyzed track, corresponded to a zero-constraint fit for the one-pion production reactions (5c)–(5e). These events would be useless at higher energies, due to backgrounds from the multipion-production reactions. However, for the relatively low energies of this experiment, the two-pion final states are negligible in the cross sections, whereas the $p\pi^+n$ final state of interest happens to account for a very large fraction of the inelastic cross section³ (e.g., $\sim 76\%$ at 1.47 GeV/c). In order to utilize the $p\pi^+n$ events, it is necessary first to reject the copious $pp \rightarrow pp$ and $pp \rightarrow \pi^+d$ events (5a) and (5b), using kinematical constraints on missing mass and coplanarity; second, to reject the $pp\pi^0$ final states (5e) using a simple kinematical cut; and third to resolve possible ambiguities between the $p_f\pi_5^+(n)$ and $p_s\pi_f^+(n)$ final states (5c) and (5d) of interest. We proceed to summarize these three steps.

Figure 2 shows the missing-mass-squared distribution for the type-B events at 1.98 GeV/c for the hypothesis $pp \rightarrow p(x)$. A missing-mass cut, $M_x^2 - M_p^2 > 0.15$ GeV², was used at all energies to separate the inelastic candidates from the tail of the elastic peak (the M_x^2 resolution is of course better at the lower energies). Note that the M_x^2 spectrum for the higher-mass inelastic events looks more or less as expected: a small peak associated with the $p\Delta^+$ final state, together with a smooth spectrum due mainly to $\Delta^{++}n$ events. The separation of $pp \rightarrow \pi^+d$ events was easily accomplished with cuts on missing mass for the

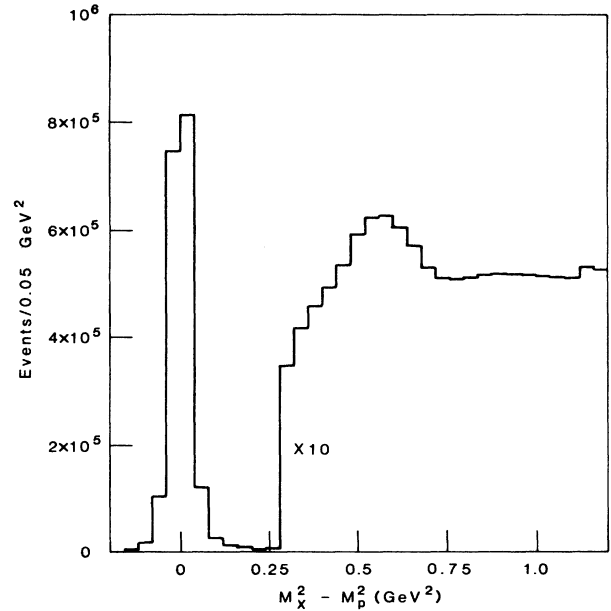


FIG. 2. Missing-mass spectrum for $pp \rightarrow p(x)$ at 2 GeV/c, showing the elastic peak at $M_x^2 - M_p^2 = 0$ and the inelastic continuum. The event rate is scaled up by a factor of 10 for $M_x^2 - M_p^2 > 0.28$ GeV² for illustrative purposes.

$pp \rightarrow d(x)$ hypothesis, together with the two angle constraints on the recoil charged track; this identification problem has been discussed elsewhere as part of a study of the $pp \rightarrow \pi^+d$ reaction.³⁸ We verified by Monte Carlo studies that the loss of genuine $p\pi^+n$ events due to this antiselection on elastic and $d\pi^+$ final states was entirely negligible.

We note that both the $pp \rightarrow pp$ and $pp \rightarrow \pi^+d$ reactions were invaluable in monitoring the experiment. Both served to provide alignment constants for the spectrometer and the recoil detector, to calibrate the performance of the target scintillator box with recoil protons and pions, to monitor the efficiency of the recoil detector and the fast anode trigger with recoil protons and pions, and to monitor the reconstruction probability for "nonsense" tracks (i.e., unphysical extra tracks in the recoil detector or the magnetostrictive wire chambers).

The rejection of $pp\pi^0$ final states depended on the properties of the zero-constraint fit. Consider the hypothesis $pp \rightarrow x_1x_2(x_3)$, where x_1 is momentum analyzed, x_2 is direction analyzed only, and x_3 is the undetected neutral particle. For mass assignments M_1 , M_2 , and M_3 the general solutions for the track-2 momentum take the form

$$|p_2| = \frac{-b \pm (b^2 - 4ac)^{1/2}}{2a}, \quad (8)$$

$$a = 4(M_x^2 - |p_1|^2 \cos^2\theta), \quad (9a)$$

$$b = 4(M_3^2 - M_2^2 - M_x^2) |p_1| \cos\theta, \quad (9b)$$

$$c = 4M_x^2 M_2^2 - (M_3^2 - M_2^2 - M_x^2)^2. \quad (9c)$$

Here M_x is the missing mass for $pp \rightarrow x_1(x)$, and θ is the

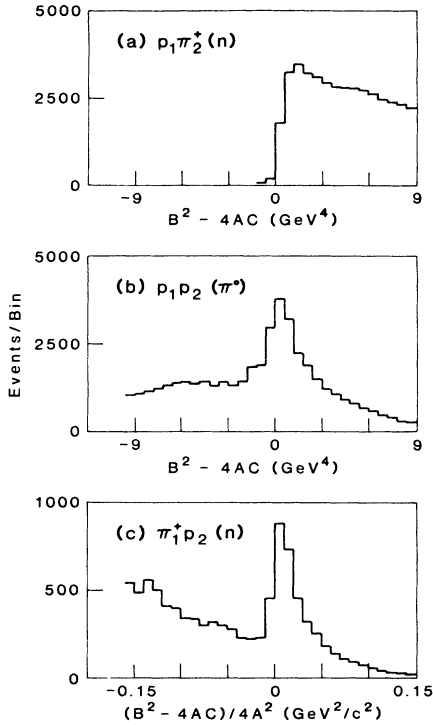


FIG. 3. Distribution of the radicand for the zero-constraint fits at 1.47 GeV/c for the hypotheses (a) $pp \rightarrow p_1 \pi_2^+(n)$, (b) $pp \rightarrow p_1 p_2(\pi^0)$, and (c) $pp \rightarrow \pi_1^+ p_2(n)$.

opening angle between particles (1) and (2). There is no physical solution to Eq. (8) for the case $(b^2 - 4ac) < 0$, and this is the basis for rejection of $pp\pi^0$ final states. Figure 3 illustrates the selection process. Figure 3(a) shows $(b^2 - 4ac)$ for the $p_1 \pi_2^+(n)$ hypothesis at 1.47 GeV/c; essentially all events satisfy $(b^2 - 4ac) > 0$. Figure 3(b) shows the same for the $p_1 p_2(\pi^0)$ hypothesis; there is a jump in the distribution above $b^2 - 4ac \approx 0$ due to production of genuine $pp\pi^0$ events, superposed on a broad background of $p\pi^+n$ events. By cutting on $(b^2 - 4ac) < -1.5$ GeV⁴, we retain $\sim 90\%$ of the genuine $p\pi^+n$ events, while rejecting essentially all of the $pp\pi^0$ contamination (the cuts were optimized by Monte Carlo studies).

After rejecting the pp , π^+d , and $pp\pi^0$ final states, 90 to 95% of the remaining events satisfy the hypothesis $x_1 x_2 x_3 = p_1 \pi_2^+ n$ but not $\pi_1^+ p_2 n$; for these events the forward momentum-analyzed track is unambiguously a proton. It also turns out that for these events there is a unique solution to Eq. (8): namely, only the plus sign in Eq. (8) gives $|p_2| > 0$. The remaining 5 to 10% of the events are ambiguous in that they satisfy both $p_1 \pi_2^+ n$ and $\pi_1^+ p_2 n$. Figure 3(c) shows the normalized quantity $(b^2 - 4ac)/4a^2$ for the $\pi_1^+ p_2 n$ hypothesis for all events after antiselection on pp , π^+d , and $pp\pi^0$ final states. There is a clear jump in this distribution at $(b^2 - 4ac) \approx 0$ threshold, corresponding to production of genuine $\pi_1^+ p_2 n$ events over a small background of $p_1 \pi_2^+ n$. This signal can be enhanced somewhat using the tags from the target scintillator box and magnet counters, and also by requir-

ing $-b/2a > 0$ in Eq. (8). Monte Carlo studies indicate that with these extra requirements the contamination of $p_1 \pi_2^+ n$ events in the $\pi_1^+ p_2 n$ signal is less than 10% [cut on $(b^2 - 4ac) > 0$ for $\pi_1^+ p_2 n$]. Unfortunately, the small sample of $\pi_1^+ p_2 n$ events suffers a quadratic ambiguity, in that Eq. (8) yields two physical solutions with $|p_2| > 0$. About 35% of these ambiguities can be resolved by range, since protons with small $|p_2|$ cannot escape the 2-in.-diam. hydrogen target (the range cutoff was calibrated using elastic events). The remaining $\pi_1^+ p_2 n$ events have two solutions for $|p_2|$, with momentum values which differ by 100 to 200 MeV/c. The kinematics are such that these ambiguous events occur for center-of-mass production angles $\Theta_\Delta < 0$, and the ambiguity is equivalent to having poorer resolution on Θ_Δ . We have included the ambiguous events by appropriately weighting both solutions. In addition, we have verified that exclusion of the ambiguous events from the analysis (with appropriate modification of the acceptance) does not alter the DME's and spin correlations within the statistical errors.

Additional selections were used to help reduce possible multipion backgrounds. Specifically a small fraction of events was rejected due to the presence of extra tracks in the recoil detector or the upstream spark chambers, or due to inconsistent hit patterns in the target-scintillator box (as noted above, these cuts were calibrated with the $pp \rightarrow pp$ and $pp \rightarrow \pi^+ d$ reactions). By repeating the full moments analysis with and without these additional selections we verified that the DME's and spin correlations were insensitive to these cuts; of course the overall cross section was sensitive to the inclusion of background (these cuts reduced the measured cross section by $\sim 5\%$ at 1.98 GeV/c, and much less at the lower momenta). Overall corrections were calculated for trigger inefficiency (5%), pion decays, recoil detector inefficiency (5–10%), spectrometer reconstruction inefficiency ($\sim 2\%$), and losses due to secondary interactions (5–10%). These corrections were included with the geometrical acceptance in the efficiency calculations, and we estimate an overall normalization uncertainty of $\pm 10\%$ associated with these corrections.

C. Acceptance corrections and moments analysis

The $p\pi^+n$ events were binned in $M_{p\pi^+}$ (20-MeV bins) and $\cos\Theta_\Delta$ (28 bins altogether), where Θ_Δ is the c.m. production angle of the $p\pi^+$ system. The events in each bin were fitted to the most general parity-conserving moments expansion:

$$\begin{aligned} \frac{d^4\sigma}{dM_{p\pi^+} d\cos\Theta_\Delta d\Omega} = & \sum_{L,M} A_{LM} \text{Re} Y_L^M(\theta, \phi) \\ & + P_x B_{LM} \text{Im} Y_L^M(\theta, \phi) \\ & + P_y C_{LM} \text{Re} Y_L^M(\theta, \phi) \\ & + P_z D_{LM} \text{Im} Y_L^M(\theta, \phi), \end{aligned} \quad (10)$$

where $\Omega = (\theta, \phi)$ gives the proton direction in the $p\pi^+$ rest

frame (RF). The Cartesian components of the beam polarization refer to a system of axis with z parallel to the beam direction and y along the production normal defined by $\mathbf{p}_{\text{beam}} \times \mathbf{p}_{p\pi^+}$. The coefficients A_{LM} were obtained by spin averaging the data in each bin; D_{LM} were obtained by comparison of spin-parallel and antiparallel data, with corrections to account for the spin alignment as noted in Sec. II A above; B_{LM} and C_{LM} were obtained from spin-up and -down transverse data, using the relations

$$P_x = P_\perp \sin\psi, \quad (11a)$$

$$P_y = P_\perp \cos\psi, \quad (11b)$$

where P_\perp is the transverse polarization and ψ is the azimuthal orientation of the spin vector (vertical laboratory axis) with respect to the production normal. The geometrical acceptance at any point in phase space can be defined by an allowed range in the angle ψ :

$$\epsilon(M_{p\pi^+}, \Theta_\Delta, \theta, \phi) = \frac{1}{2\pi} \int_{\text{allowed}} d\psi. \quad (12)$$

The allowed ψ range was defined analytically by fiducial cuts, which were imposed on the events to obtain the spin-averaged coefficients A_{LM} . It is easy to show that once the A_{LM} are determined, the coefficients B_{LM} , C_{LM} , and D_{LM} can be obtained without reference to the acceptance and without imposition of corresponding fiducial cuts on the events. Note that small additional corrections are needed in Eq. (12) to account for nongeometrical losses (pion decays, secondary interactions, and detector inefficiencies), and these can be included either directly in Eq. (12) or as weighting factors in the events.

We used several slightly different methods to obtain the acceptance corrected A_{LM} with equivalent results. The most useful method involved binning the events further in the angles θ and ϕ . The problem then reduced to fitting the observed bin populations to obtain A_{LM} , using the relation

$$n_i = F \left[\sum_{L,M} A_{LM} \text{Re} Y_L^M(\theta_i, \phi_i) \right] \epsilon(\theta_i, \phi_i) dM d \cos\Theta_\Delta d\Omega, \quad (13)$$

where F is the incident flux (in events/mb).

The corresponding maximum-likelihood analysis³⁹ involves minimizing the quantity

$$\ln(L) = \sum_i (n_i \ln p_i - p_i), \quad (14)$$

$$\begin{aligned} \pm P_z \sum D_{LM} \text{Im} Y_L^M(\theta_i, \phi_i) \rightarrow \pm P_\parallel \sum [\sin\alpha \cos\psi B_{LM} \text{Im} Y_L^M(\theta_i, \phi_i) - \sin\alpha \sin\psi C_{LM} \text{Re} Y_L^M(\theta_i, \phi_i) \\ + \cos\alpha D_{LM} \text{Im} Y_L^M(\theta_i, \phi_i)], \end{aligned} \quad (17)$$

where α is the angle offset of the parallel spin vector in the horizontal laboratory plane, and P_\parallel is the average parallel polarization. Since B_{LM} and C_{LM} can be determined separately from the transverse data, it is straightforward to solve for D_{LM} , making the substitution (17) in the likelihood function of Eq. (16).

The Pauli principle imposes an important constraint on

where

$$p_i = \langle n_i \rangle$$

is the expected bin population for bin i given by the right-hand side (RHS) of Eq. (13). An equivalent result can be obtained by a least-squares fit to Eq. (13).

The spin correlations were also obtained by binning in θ and ϕ , this time separating the spin-up and -down samples. Consider the determination of D_{LM} , assuming equal fluxes for spin up and spin down, and ignoring, for simplicity, the aforementioned angle offset in the spin-parallel running. In each θ_i, ϕ_i bin, the event populations can be fitted to the expression

$$\begin{aligned} n_i(\uparrow, \downarrow) = F \left[\sum A_{LM} \text{Re} Y_L^M(\theta_i, \phi_i) \right. \\ \left. \pm P_z \sum D_{LM} \text{Im} Y_L^M(\theta_i, \phi_i) \right] \\ \times \epsilon(\theta_i, \phi_i) dM d \cos\Theta_\Delta d\Omega. \end{aligned} \quad (15)$$

The logarithm of the likelihood function takes the form

$$\begin{aligned} \ln(L_\uparrow L_\downarrow) = \sum_{i(\uparrow)} [n_i(\uparrow) \ln p_i(\uparrow) - p_i(\uparrow)] \\ + \sum_{i(\downarrow)} [n_i(\downarrow) \ln p_i(\downarrow) - p_i(\downarrow)], \end{aligned} \quad (16)$$

where

$$p_i(\uparrow, \downarrow) = \langle n_i(\uparrow, \downarrow) \rangle$$

is again the expected bin population for spin up or down, given by the RHS of Eq. (15). If A_{LM} are fixed in Eq. (15) from the previous fits, then the geometrical acceptance $\epsilon(\theta, \phi)$ drops out in minimizing Eq. (16) for D_{LM} . This is a generalization of the fact, familiar from elastic scattering, that the spin dependence in principle involves only ratios of spin-up and -down event rates, in which the acceptance cancels.

The above discussion is oversimplified for purposes of illustration. To obtain the transverse correlations B_{LM} and C_{LM} , it was necessary to record not only sums of events in each (θ_i, ϕ_i) bin [e.g., $n_i(\uparrow, \downarrow)$ in Eq. (16)], but also sums over $\sin\psi$, $\cos\psi$, $\sin^2\psi$, $\sin\psi \cos\psi$, and $\cos^2\psi$; these are needed to separate the P_x and P_y dependence once the expression (11) for P_x and P_y is substituted into Eq. (10). Furthermore, for the spin "parallel" analysis, it is necessary to make the substitution in Eq. (15)

the spin-averaged A_{LM} . We used an s -channel coordinate system in fitting the moments, so that (θ, ϕ) refer to the proton direction in the $p\pi^+$ RF, with y along the production normal and z along the direction $\mathbf{p}_{p\pi^+}$ in the overall c.m. (equivalently, along $-\mathbf{p}_n$ in the $p\pi^+$ (RF). The decay angles (θ, ϕ) are defined by

$$\sin\theta \sin\phi = \mathbf{p}_p \cdot \hat{\mathbf{y}}, \quad (18a)$$

$$\sin\theta \cos\phi = \mathbf{p}_p \cdot (\hat{\mathbf{y}} \times \hat{\mathbf{z}}), \quad (18b)$$

$$\cos\theta = \mathbf{p}_p \cdot \hat{\mathbf{z}}. \quad (18c)$$

The Pauli principle then requires

$$\sigma(\Theta_\Delta, \theta, \phi) = \sigma(\pi - \Theta_\Delta, \theta, \phi + \pi), \quad (19)$$

and consequently

$$A_{LM}(\pi - \Theta_\Delta) = (-1)^M A_{LM}(\Theta_\Delta) \quad (20)$$

in Eq. (9). In our analysis of the A_{LM} , we folded the data and the acceptance about $\Theta_\Delta = 90^\circ$, consistent with Eq. (19). We then checked the fit predictions against the measured event-rate projections in θ and ϕ for each bin in $M_{p\pi^+}$ and Θ_Δ . The fits were satisfactory for both forward and backward production in $\cos\Theta_\Delta$, except for small systematic discrepancies which were clearly associated with the trigger topology. In particular, the events which were reconstructed with a forward momentum-analyzed pion in the spectrometer and a recoil proton seemed to have a systematically low ($\sim 80\%$) recovery efficiency compared with the more common topologies involving forward protons. Although the effect was not completely understood, once a consistent set of A_{LM} are determined, the spin correlations should be insensitive to small systematic errors in the efficiency calculations.

We note that the A_{LM} moments were checked for positivity; that is, in each $(\cos\Theta_\Delta, M_{p\pi^+})$ bin, the cross section was checked for positivity over a fine grid in θ, ϕ . In a very few bins where negative cross sections were obtained (these coincided with regions of zero acceptance in θ, ϕ) the A_{LM} were pulled, consistent with the statistical error

matrix, to satisfy positivity. Similar checks were performed with the polarization coefficients, but these were not corrected to ensure positivity. Consequently, for a few bins ($< 1\%$), the transverse or longitudinal spin correlations were larger than the unpolarized cross sections, but this would be expected given the size of the measured asymmetries and the statistical errors on the coefficients.

III. FORMALISM

In this section we summarize the formalism needed to interpret the spherical harmonics expansion of Sec. II. First we recast the spherical harmonics in a density-matrix representation (III A), and then in the joint-moments representation (III B). In III C we enumerate some key relations involving helicity and partial-wave amplitudes and develop the numerical coefficients relating joint moments and partial-wave products. In III D we discuss the isobar contributions to the $p\pi^+n$ final state. Further details on pion-exchange and isobar interference effects are included in the Appendices.

A. Density-matrix expansion

The higher L ($L \geq 3$) coefficients in the spherical harmonics expansion turned out to be negligible for $M_{p\pi^+} \lesssim 1.3$ GeV, except for kinematical regions close to threshold for the final-state proton-neutron system, as discussed in Sec. V. The absence of $L \geq 3$ terms is, of course, consistent with the dominance of S - and P -wave $p\pi^+$ isobars, as might be expected for low $p\pi^+$ masses. We can replace the $L \leq 2$ spherical harmonics expansion with a density-matrix representation:

$$\begin{aligned} \frac{d^4\sigma}{dM_{p\pi^+} d\cos\Theta_\Delta d\Omega} &= \frac{d^2\sigma}{dM_{p\pi^+} d\cos\Theta_\Delta} \frac{1}{4\pi} \\ &\times [(\rho_{11} + P_y \rho_{11})(3 \cos^2\theta + 1) + (\rho_{33} + P_y \rho_{33})(3 \sin^2\theta) - (\rho_{31} + P_y \rho_{31})(4\sqrt{3} \sin\theta \cos\theta \cos\phi) \\ &- (P_x \rho_{31} + P_z \rho_{31})(4\sqrt{3} \sin\theta \cos\theta \sin\phi) - (\rho_{3-1} + P_y \rho_{3-1})(2\sqrt{3} \sin^2\theta \cos 2\phi) \\ &- (P_x \rho_{3-1} + P_z \rho_{3-1})(2\sqrt{3} \sin^2\theta \sin 2\phi) + (\rho_{s1} + P_y \rho_{s1})(4 \cos\theta) \\ &+ (\rho_{s-1} + P_y \rho_{s-1})(4 \sin\theta \cos\phi) + (P_x \rho_{s-1} + P_z \rho_{s-1})(4 \sin\theta \sin\phi)] . \end{aligned} \quad (21)$$

The nomenclature for the spin-averaged DME's ρ_{11} , ρ_{33} , ρ_{31} , and ρ_{3-1} is standard. The spin correlations are designated by the symbols $P_i \rho_{jk}$; these refer to the spin dependence of the angular distribution for 100% polarization for Cartesian component P_i . The terms involving ρ_{s1} and ρ_{s-1} allow for interference of S - and P -wave $p\pi^+$ isobars. Since $\rho_{11} + \rho_{33} = \frac{1}{2}$, integration over θ and ϕ yields two observables: the cross section, $d^2\sigma/dM_{p\pi^+} d\cos\Theta_\Delta$, and the integrated left-right asymmetry

$$A_y = 2P_y \rho_{11} + 2P_y \rho_{33}. \quad (22)$$

While the cross section and A_y are frame invariant, the numerical values of the DME's and SSC's are in general different for the s - and t -channel frames, both because of the different definitions of the decay angles θ and ϕ , and because the beam polarization components P_x and P_z refer to different axes. The s -channel frame is convenient for partial-wave analysis and also because the Pauli prin-

principle has a simpler expression in the s channel [Eq. (18)]. However, the unpolarized DME's turn out to have smoother behavior in the t channel. For reference, we define the s - and t -channel z axes for the four "particles" in $p_B p_T \rightarrow (p\pi^+) n$ in Table I. The y axis is common for the four particles and is frame invariant ($\hat{y} = \mathbf{p}_b \times \mathbf{p}_{p\pi^+}$). Thus, the t -channel (θ, ϕ) angles are defined as in Eq. (17), with \hat{z}_s replaced by \hat{z}_t ; the beam polarization components P_x and P_z are likewise referenced to the beam proton axes listed in Table I.

B. Joint-moments expansion

At low energies, it is convenient to further expand the individual DME's and SSC's in functions of the $p\pi^+$ c.m. production angle Θ_Δ . We have used the general expression

$$\frac{d\sigma}{d\cos\Theta_\Delta} P_i \rho_{jk} = \frac{\sigma}{2} \sum_L a_{MN}^L(P_i \rho_{jk}) d_{MN}^L(\cos\Theta_\Delta). \quad (23a)$$

The differential cross section itself is expanded as

$$\frac{d\sigma}{d\cos\Theta_\Delta} = \frac{\sigma}{2} \sum_L a_{00}^L \left[\frac{d\sigma}{d\cos\Theta_\Delta} \right] d_{00}^L(\cos\Theta_\Delta), \quad (23b)$$

where the normalization is specified by $a_{00}^0(d\sigma/d\cos\Theta_\Delta) = 1$ and

$$\sigma = \int_{-1}^1 \frac{d\sigma}{d\cos\Theta_\Delta} d\cos\Theta_\Delta. \quad (23c)$$

The joint moments depend, of course, on the $M_{p\pi^+}$ interval.

The indices (M, N) in the moments expansion are specific to each DME. The index L takes on only even values for the unpolarized DME's because of the Pauli principle [Eq. (18)]; for the spin correlations L can take all values consistent with the indices (M, N) . Each joint moment can be expressed as a sum of partial-wave products. For the unpolarized DME's these sums take the form

$$\frac{\sigma}{2} a_{MN}^L(\rho_{ij}) = \sum_{\alpha, \beta} C_{\alpha\beta}^{SS} \text{Re}(S_\alpha S_\beta^*) + C_{\alpha\beta}^{TT} \text{Re}(T_\alpha T_\beta^*), \quad (24)$$

where S_α (T_α) are partial waves for singlet (triplet) initial proton-proton spin states. For the polarized DME's these sums take the form

TABLE I. Definition of s - and t -channel z axes (\hat{z}_s, \hat{z}_t) for the four "particles" in $pp \rightarrow (p\pi^+)n$; the subscripts refer to beam proton, target proton, $p\pi^+$ isobar, and recoil neutron, respectively ($b, t, p\pi^+$, and n). The momentum vectors are evaluated in the rest frame of the respective particles.

Particle	z_s	z_t
Beam proton	$-\hat{\mathbf{p}}_t$	$-\hat{\mathbf{p}}_{p\pi^+}$
$p\pi^+$ system	$-\hat{\mathbf{p}}_n$	$+\hat{\mathbf{p}}_b$
Target proton	$-\hat{\mathbf{p}}_b$	$-\hat{\mathbf{p}}_n$
Recoil neutron	$-\hat{\mathbf{p}}_{p\pi^+}$	$+\hat{\mathbf{p}}_t$

$$\frac{\sigma}{2} a_{MN}^L(P_i \rho_{jk}) = \sum_{\alpha, \beta} C_{\alpha\beta}^{ST} \text{Im}(S_\alpha T_\beta^*) \quad (25a)$$

or

$$\frac{\sigma}{2} a_{MN}^L(P_i \rho_{jk}) = \sum_{\alpha, \beta} C_{\alpha\beta}^{TT} \text{Im}(T_\alpha T_\beta^*), \quad (25b)$$

depending on whether L is even or odd. For example, for the integrated asymmetry A_y , the singlet-triplet (ST) interferences contribute to odd L and the triplet-triplet (TT) to even L ; since $(M, N) = (1, 0)$ for the A_y expansion, the ST terms give A_y symmetric in $\cos\Theta_\Delta$, and the TT terms give A_y antisymmetric. The same symmetry relation holds for A_y in $pp \rightarrow \pi^+ d$. In general, depending on the spin correlation, ST terms can correspond to either even or odd L , with the opposite relation for TT terms. Table II provides a breakdown of the (L, M, N) values allowed for each ρ_{jk} and $P_i \rho_{jk}$, the correspondence between even and odd L and ST and TT terms, and the $\cos\Theta_\Delta$ symmetry of the ST and TT series.

We digress to clarify the behavior of the DME's near $\cos\Theta_\Delta = \pm 1$. From the moments expansion it is clear that some of the spin correlations, for example, A_y , $P_y \rho_{11}$, and $P_y \rho_{33}$, vanish at $\cos\Theta_\Delta = \pm 1$ because of angular-momentum conservation, as do the unpolarized DME's ρ_{31} , ρ_{3-1} , and ρ_{s-1} ; these DME's give explicit $\cos\phi$ dependence, and ϕ is undefined for $\cos\Theta_\Delta = \pm 1$. However, the correlations $P_y \rho_{31}$, $P_x \rho_{31}$, $P_y \rho_{s-1}$, and $P_x \rho_{s-1}$ have $(M, N) = (0, 0)$ in the moments expansion and so need not vanish at $\cos\Theta_\Delta = \pm 1$. This may seem paradoxical since these SSC's are also associated with ϕ dependence in the DME expansion [Eq. (21)]. In fact, the amplitude structure imposes the constraints

$$P_y \rho_{31}(\cos\Theta_\Delta = \pm 1) = \mp P_x \rho_{31}(\cos\Theta_\Delta = \pm 1), \quad (26a)$$

$$P_y \rho_{s-1}(\cos\Theta_\Delta = \pm 1) = \mp P_x \rho_{s-1}(\cos\Theta_\Delta = \pm 1). \quad (26b)$$

With these constraints, the spin dependence from these SSC's behaves like $P_\perp \cos(\phi \pm \psi)$ near $\cos\Theta_\Delta = \pm 1$, where ψ is defined by Eq. (11). Unlike ϕ alone, the angle $(\phi \pm \psi)$ is defined for $\cos\Theta_\Delta = \pm 1$; it is the azimuthal orientation of the $p\pi^+$ decay normal with respect to the spin vector. This kind of correlation is exactly what would be expected from off-shell $\pi^+ p_t \rightarrow \pi^+ p$ elastic scattering. We have not imposed the constraints implied by Eq. (26) on the measured joint moments.

C. Amplitude relationships

Consider the s -channel helicity amplitudes for production of any $p\pi^+$ isobar; we label the $p\pi^+$ isobars by indices j and l (total and orbital angular momentum, respectively). We use lower case j and l deliberately, reserving J and L to label the production waves. We adopt the normalization

$$\frac{d^2\sigma}{dM_{p\pi^+} d\cos\Theta_\Delta} = \frac{\pi}{k^2} \sum_{M, \lambda_b, \lambda_t, \lambda_n} |A_{\lambda_n \lambda_t}^{M \lambda_b}|^2, \quad (27)$$

where k is the initial proton-proton c.m. momentum, and M, λ_b, λ_t , and λ_n are the helicities for the $p\pi^+$ isobar and the beam, target, and recoil nucleons, respectively. Parity

TABLE II. For each observable we list the d functions used in the joint-moments expansion and the allowed L values. We also indicate the parity of these functions (even or odd) under reflections about $\Theta_\Delta=90^\circ$. For the unpolarized DME's there is only one series; for the spin correlations we list the singlet-triplet and triplet-triplet series separately.

Observable	d function	(Singlet-singlet + triplet-triplet)			
$d\sigma/d\cos\Theta_\Delta$	d_{00}^L	$L=0,2,4$	(even)		
ρ_{11}	d_{00}^L	$L=0,2,4$	(even)		
ρ_{33}	d_{00}^L	$L=0,2,4$	(even)		
ρ_{31}	d_{01}^L	$L=2,4,6$	(odd)		
ρ_{3-1}	d_{02}^L	$L=2,4,6$	(even)		
ρ_{s1}	d_{00}^L	$L=0,2,4$	(even)		
ρ_{s-1}	d_{01}^L	$L=2,4,6$	(odd)		
		(Singlet-triplet)		(triplet-triplet)	
A_y	d_{10}^L	$L=1,3,5$	(even)	$L=2,4,6$	(odd)
$P_y\rho_{11}$	d_{10}^L	$L=1,3,5$	(even)	$L=2,4,6$	(odd)
$P_y\rho_{33}$	d_{10}^L	$L=1,3,5$	(even)	$L=2,4,6$	(odd)
$P_y\rho_{31}$	d_{00}^L	$L=1,3,5$	(odd)	$L=0,2,4$	(even)
$P_y\rho_{3-1}$	d_{01}^L	$L=1,3,5$	(even)	$L=2,4,6$	(odd)
$P_x\rho_{31}$	d_{00}^L	$L=0,2,4$	(even)	$L=1,3,5$	(odd)
$P_x\rho_{3-1}$	d_{01}^L	$L=2,4,6$	(odd)	$L=1,3,5$	(even)
$P_z\rho_{31}$	d_{01}^L	$L=2,4,6$	(odd)	$L=1,3,5$	(even)
$P_z\rho_{3-1}$	d_{02}^L	$L=2,4,6$	(even)	$L=3,5,7$	(odd)
$P_y\rho_{s1}$	d_{10}^L	$L=1,3,5$	(even)	$L=2,4,6$	(odd)
$P_y\rho_{s-1}$	d_{00}^L	$L=1,3,5$	(odd)	$L=0,2,4$	(even)
$P_x\rho_{s-1}$	d_{00}^L	$L=0,2,4$	(even)	$L=1,3,5$	(odd)
$P_z\rho_{s-1}$	d_{01}^L	$L=2,4,6$	(odd)	$L=1,3,5$	(even)

conservation in production gives the constraint

$$A_{-\lambda_n-\lambda_t}^{-M-\lambda_b}(\Theta_\Delta) = (-1)^{j+(3/2)+M+\lambda_b+\lambda_n+\lambda_t} \eta_j A_{\lambda_n\lambda_t}^{M\lambda_b}(\Theta_\Delta), \quad (28)$$

where $\eta_j = (-1)^{l+1}$ is the intrinsic parity of the $p\pi^+$ system, and $j + \frac{3}{2}$ is the spin sum over the four "particles" participating in the reaction. The Pauli principle imposes the symmetry

$$A_{\lambda_n\lambda_t}^{M\lambda_b}(\Theta_\Delta) = (-1)^{M+\lambda_n+\lambda_b+\lambda_t} A_{\lambda_n\lambda_b}^{M\lambda_t}(\pi-\Theta_\Delta). \quad (29)$$

The helicity amplitudes can be expanded in a partial-wave series:

$$A_{\lambda_n\lambda_t}^{M\lambda_b}(\Theta_\Delta) = \sum_{J,L_i,L_f,S_i,S_f} d_{\lambda\mu}^J(\Theta_\Delta) W(J,j,l,L_i,S_i,L_f,S_f) \times C_{M\lambda_b\lambda_n\lambda_t}^{JjL_iS_iL_fS_f}, \quad (30a)$$

where

$$C_{M\lambda_b\lambda_n\lambda_t}^{JjL_iS_iL_fS_f} = \langle J\lambda | S_i\lambda L_i 0 \rangle \langle S_i\lambda | \frac{1}{2}\lambda_b \frac{1}{2} - \lambda_t \rangle \times \langle JM | S_f M L_f 0 \rangle \langle S_f M | jM \frac{1}{2} - \lambda_n \rangle \times (2L_i+1)(2L_f+1)^{1/2} (-1)^{\lambda_n-\lambda_t}, \quad (30b)$$

and where $\lambda = \lambda_b - \lambda_t$, $\mu = M - \lambda_n$. The partial waves $W(J,j,l,L_i,S_i,L_f,S_f)$ are labeled according to total J , to-

tal initial- and final-state orbital momenta and spin ($L_{i,f}$ and $S_{i,f}$), and $p\pi^+$ isobar (j,l). Expansion (30) automatically satisfies the Pauli principle and parity conservation with the obvious restrictions that $(-1)^{L_i+S_i} = +1$, and $(-1)^{L_i+L_f+l+1} = +1$. In applications we will use standard terminology for the amplitudes $W(J, \dots)$, namely, ${}^{2S_i+1}(L_i)_{2J+1} \rightarrow {}^{2S_f+1}(L_f)_{2J+1}$ (for example, ${}^1D_2 \rightarrow {}^5S_2$, ${}^3F_3 \rightarrow {}^5P_3$, etc).

Integrated over the production angle, Eqs. (27) and (30) imply the normalization

$$\frac{d\sigma}{dM_{p\pi^+}} = \frac{2\pi}{k^2} \sum_{J,L,S_i,j,l} (2J+1) |W(J,j,l,L_i,S_i,L_f,S_f)|^2. \quad (31)$$

For $pp \rightarrow \Delta^{++}n$, the partial-wave amplitudes can presumably be factorized in the limit of small Γ_Δ into a production wave and a mass-dependent Δ^{++} Breit-Wigner line shape, e.g.,

$$W(J,j,l,L_i,S_i,L_f,S_f) = W_p(J,j,l,L_i,S_i,L_f,S_f) F_{jl}(M_{p\pi^+}), \quad (32a)$$

where

$$1 = \int dM_{p\pi^+} |F_{jl}(M_{p\pi^+})|^2. \quad (32b)$$

In that case, the normalization of Eq. (31) is consistent with the optical theorem for $pp \rightarrow pp$ elastic scattering; integrated over $M_{p\pi^+}$, the total cross section for $pp \rightarrow \Delta^{++}n$ would take the form

$$\sigma(pp \rightarrow \Delta^{++}n) = \frac{2\pi}{k^2} \sum_{J,L,S,l,j} (2J+1) |W_p(J,j,l,L_i,S_i,L_f,S_f)|^2, \quad (33)$$

exactly analogous to the expression for $\sigma(pp \rightarrow pp)$. For a two-channel S matrix involving pp and ΔN , we would have

$$W_p(J,j,l,L_i,S_i,L_f,S_f) = \left[\frac{3}{4} \right]^{1/2} \frac{(1-\eta^2)^{1/2}}{2} e^{i\delta_{pp} + \delta_{\Delta N}}, \quad (34a)$$

where $(\frac{3}{4})^{1/2}$ takes care of isospin conservation [$\sigma(\Delta N) = \frac{4}{3}\sigma(\Delta^{++}n)$]. The corresponding elastic waves normalized as in Eq. (33) would take the form

$$W(J,L_i,S_i) = \frac{\eta e^{2i\delta_{pp}} - 1}{2i}. \quad (34b)$$

The extra factor of 2 in the optical theorem of Eq. (33) is required by the Pauli principle for $pp \rightarrow pp$ and $pp \rightarrow \Delta N$ (see Ref. 40).

To obtain the dependence on the $p\pi^+$ decay angles θ and ϕ , we write the associated helicity amplitudes

$$T_{\lambda_n \lambda_i}^{\lambda_p \lambda_b}(\Theta_\Delta, \theta, \phi) = \sum_M A_{\lambda_n \lambda_i}^{M \lambda_b}(\Theta_\Delta) e^{i(M-\lambda_n)\phi} d_{M \lambda_p}^j(\theta) g_{j l \lambda}, \quad (35a)$$

where

$$g_{j l 1/2} = +1, \quad (35b)$$

$$g_{j l -1/2} = (-1)^{j+l-1/2} \quad (35c)$$

guarantee parity conservation in the $p\pi^+$ isobar decay. The phase conventions implied by Eq. (35a) for the T amplitudes are such that the final-state proton and neutron have their helicities λ_p and λ_n quantized along z axes in the $p\pi^+n$ three-body plane, with common y axis given by the normal to this plane (for the A amplitudes λ_n refers to the production helicity frame). The full angular distribution can then be expressed as

$$\frac{d^4\sigma}{dM_{p\pi^+} d \cos\Theta_\Delta d\Omega} = \frac{\pi}{k^2} \sum_{\lambda_b, \lambda_b', \lambda_p, \lambda_n, \lambda_i} (T_{\lambda_n \lambda_i}^{\lambda_p \lambda_b} \rho_{\lambda_b \lambda_b'}^b T_{\lambda_n \lambda_i}^{\lambda_p \lambda_b'})^* \frac{2j+1}{8\pi}. \quad (36)$$

The beam spin-density matrix is given by

$$\rho_{\lambda_b \lambda_b'}^b = (1 + \mathbf{P} \cdot \boldsymbol{\sigma})_{\lambda_b \lambda_b'}. \quad (37)$$

The formalism can be extended to include other spin observables; for example, the target density matrix ρ^t can be inserted in Eq. (36) to generate spin-spin correlations.

By comparison of Eqs. (21), (30), (35), and (36), we can expand each DME in terms of helicity amplitudes $A_{\lambda_n \lambda_i}^{M \lambda_b}$ or partial-wave amplitudes $W(J,j,l,L_i,S_i,L_f,S_f)$. We have displayed the helicity-amplitude expansion in Ref. 2.

Table III gives the expansion of some of the joint moments $a_{MN}^L(P_i \rho_{jk})$ in terms of partial-wave products. This table is abbreviated to include only the most prominent $pp \rightarrow \Delta^{++}n$ transitions expected at low energies; more extensive tables, including non- Δ^{++} isobars, are available from the authors. Note that in this discussion we have considered only $p\pi^+$ isobars, so that the coefficients in Table III are independent of $M_{p\pi^+}$ (any $M_{p\pi^+}$ dependence must be inserted in the partial-wave amplitudes). For use in Sec. VII we have displayed some of the spin-spin correlations as well; for those observables we use common $\mathbf{x}, \mathbf{y}, \mathbf{z}$ axes for beam and target proton, with \mathbf{z} along the beam momentum and $\mathbf{x} = \mathbf{y} \times \mathbf{z}$. [Note that for the helicity expansion of Eq. (36), the target proton \mathbf{z} axis is opposite the beam momentum.]

D. Isobar contributions

Although the previous formalism is quite general, we will consider only the $l=0$ and 1 $p\pi^+$ isobars; we designate the nonresonant $j^P = \frac{1}{2}^\pm$ isobars by s and p ($l=0$ and 1), and $j^P = \frac{3}{2}^+$ by Δ . Again, we reserve S, P, D upper case labels for the production waves (L_i or L_f). In the mass range of interest, we expect the production waves to be much larger for Δ than for s, p waves, and consequently we expect Δ - Δ , s - Δ , and p - Δ interferences to be much more important than s - s , s - p , or p - p contributions. The s - Δ interferences are isolated in the correlations $\rho_{s1}, \rho_{s-1}, P_y \rho_{s-1}, P_x \rho_{s-1},$ and $P_z \rho_{s-1}$. The p - Δ interferences are mixed with the Δ - Δ terms in the remaining twelve observables and cannot be separated without a model.

Figure 4 illustrates the pion-exchange production mechanisms. Charged-pion exchange [Fig. 4(a)] would result in direct production of $s, p,$ and Δ isobars in proportion to the corresponding π^+p elastic waves. Neutral-pion exchange (Fig. 4(b)) would result in direct production of Δ^+ and also $I = \frac{1}{2}$ π^+n isobars via virtual $\pi^0 p \rightarrow \pi^+ n$; these in turn would contribute to the $s, p,$ and Δ isobars in the $p\pi^+$ system. The Δ^+ production component is expected to be the dominant π^0 -exchange contribution, and this is examined further below. The $I = \frac{1}{2}$ π^+n isobars are expected to be quite small relative to the Δ^{++}/Δ^+ amplitudes or the $I = \frac{3}{2}$ s - and p -wave $p\pi^+$ isobars from charged-pion exchange. This is because (1) the phase shifts $\delta(S_{11}), \delta(P_{11}),$ and $\delta(P_{13})$ are quite small in the relevant π^+n mass range, and (2) these isobars are suppressed by an isospin factor of $\frac{1}{3}$, as compared with the $p\pi^+$ isobars. Consequently we ignore $I = \frac{1}{2}$ π^+n production altogether.

We have used a version of the Williams model⁴¹ (WM) to describe the charged-pion-exchange contributions of Fig. 4(a). Details of the WM are summarized in Appendix A, and fit parameters at each energy are listed in Table IV. The model has been shown to work fairly well at higher energies and low momentum transfers.² However, the WM assumes relatively real production amplitudes,

TABLE III. Expansion of the joint moments $(\sigma/2)a_{MN}^L(P_i\rho_{jk})$ in partial-wave products as defined by Eqs. (24) and (25). The columns labeled W and W'^* list the partial-wave amplitudes. For each W, W'^* entry, the columns to the right list the expansion coefficients $C_{\alpha\beta}$ in Eqs. (24) and (25); multiplying $C_{\alpha\beta}$ by the partial-wave product gives the corresponding contribution to the observables $(\sigma/2)a_{MN}^L$ which are indicated by the column headers (for brevity the columns are labeled simply by a_{MN}^L). We have separated singlet-singlet (SS), triplet-triplet (TT), and singlet-triplet (ST) partial-wave entries as indicated. For brevity we have included only the first three moments for each $P_i\rho_{jk}$, and we have retained only the most important Δ -production waves corresponding to initial states ${}^1S_0, {}^3P_{0,1,2}, {}^1D_2, {}^3F_{2,3}, {}^1G_4$, and 3H_5 . Also for brevity, we have listed only the ρ_{11} and ρ_{33} observables for the two-spin correlations. The zero- and two-spin coefficients are for $\text{Re}(WW'^*)$, while the single-spin are for $\text{Im}(WW'^*)$. To simplify the normalization, we have extracted a factor $(\pi/k^2)[(2J+1)(2J'+1)]^{1/2}$ from each coefficient (J, J' refer to the total J for waves W, W' , respectively). Each coefficient should be multiplied by this factor before performing the expansions of Eqs. (24) and (25).

W	W'^*	a_{00}^0	$\rho_{11}(SS)$ a_{00}^2	a_{00}^4	a_{00}^0	$\rho_{33}(SS)$ a_{00}^2	a_{00}^4	a_{01}^2	$\rho_{31}(SS)$ a_{01}^4	a_{01}^6	a_{02}^2	$\rho_{3-1}(SS)$ a_{02}^4	a_{02}^6
${}^1S_0 \rightarrow {}^5D_0$	${}^1S_0 \rightarrow {}^5D_0$	0.500											
${}^1S_0 \rightarrow {}^5D_0$	${}^1D_2 \rightarrow {}^5S_2$		1.000					0.354				0.707	
${}^1D_2 \rightarrow {}^5S_2$	${}^1D_2 \rightarrow {}^5S_2$	0.250	0.250		0.250	-0.250		0.354				-0.354	
${}^1S_0 \rightarrow {}^5D_0$	${}^1G_4 \rightarrow {}^5D_4$			1.604					0.518			0.732	
${}^1D_2 \rightarrow {}^5S_2$	${}^1G_4 \rightarrow {}^5D_4$		1.031	0.573		0.573	-0.573	0.162	0.739			0.324	-0.523
${}^1G_4 \rightarrow {}^5D_4$	${}^1G_4 \rightarrow {}^5D_4$	0.321	0.383	0.338	0.179	0.128	-0.063	0.180	0.291	0.304		-0.361	-0.274
W	W'^*	a_{00}^0	$\rho_{11}(TT)$ a_{00}^2	a_{00}^4	a_{00}^0	$\rho_{33}(TT)$ a_{00}^2	a_{00}^4	a_{01}^2	$\rho_{31}(TT)$ a_{01}^4	a_{01}^6	a_{02}^2	$\rho_{3-1}(TT)$ a_{02}^4	a_{02}^6
${}^3P_0 \rightarrow {}^3P_0$	${}^3P_0 \rightarrow {}^3P_0$	0.500											
${}^3P_1 \rightarrow {}^3P_1$	${}^3P_1 \rightarrow {}^3P_1$	0.125	0.063		0.375	0.188						-0.265	
${}^3P_1 \rightarrow {}^3P_1$	${}^3P_1 \rightarrow {}^5P_1$	0.335	0.168		-0.335	-0.168		0.237				-0.237	
${}^3P_1 \rightarrow {}^5P_1$	${}^3P_1 \rightarrow {}^5P_1$	0.425	-0.088		0.075	0.038		-0.106				0.159	
${}^3P_0 \rightarrow {}^3P_0$	${}^3P_2 \rightarrow {}^3P_2$		0.894					0.474					
${}^3P_1 \rightarrow {}^3P_1$	${}^3P_2 \rightarrow {}^3P_2$		0.290			0.871		-0.411				0.411	
${}^3P_1 \rightarrow {}^5P_1$	${}^3P_2 \rightarrow {}^3P_2$		0.390			-0.390		0.367				0.184	
${}^3P_2 \rightarrow {}^3P_2$	${}^3P_2 \rightarrow {}^3P_2$	0.275	0.238		0.225	0.113		0.106				-0.159	
${}^3P_0 \rightarrow {}^3P_0$	${}^3P_2 \rightarrow {}^5P_2$							0.158				-0.632	
${}^3P_1 \rightarrow {}^3P_1$	${}^3P_2 \rightarrow {}^5P_2$		-0.290			0.290		-0.274				-0.137	
${}^3P_1 \rightarrow {}^5P_1$	${}^3P_2 \rightarrow {}^5P_2$		-0.390			-0.130		-0.306				0.674	
${}^3P_2 \rightarrow {}^3P_2$	${}^3P_2 \rightarrow {}^5P_2$	-0.150	-0.075		0.150	0.075		-0.177				0.389	
${}^3P_2 \rightarrow {}^5P_2$	${}^3P_2 \rightarrow {}^5P_2$	0.075	0.038		0.425	-0.388		0.212				0.053	
${}^3P_0 \rightarrow {}^3P_0$	${}^3F_2 \rightarrow {}^3P_2$		-1.095					-0.581					
${}^3P_1 \rightarrow {}^3P_1$	${}^3F_2 \rightarrow {}^2P_2$		0.237			0.712		-0.335				0.335	
${}^3P_1 \rightarrow {}^5P_1$	${}^3F_2 \rightarrow {}^3P_2$		0.318			-0.318		0.300				0.150	
${}^3P_2 \rightarrow {}^3P_2$	${}^3F_2 \rightarrow {}^3P_2$		-0.166	-0.630		-0.079	0.630	-0.074	-0.813			0.111	0.575
${}^3P_2 \rightarrow {}^5P_2$	${}^3F_2 \rightarrow {}^3P_2$		0.026	-0.210		-0.026	0.210	0.062	-0.271			-0.136	0.192
${}^3F_2 \rightarrow {}^3P_2$	${}^3F_2 \rightarrow {}^3P_2$	0.275	0.271	0.129	0.225	0.129	-0.129	0.121	0.166			-0.182	-0.117
${}^3P_0 \rightarrow {}^3P_0$	${}^3F_2 \rightarrow {}^5P_2$							-0.194				0.775	
${}^3P_1 \rightarrow {}^3P_1$	${}^3F_2 \rightarrow {}^5P_2$		-0.237			0.237		-0.224				-0.112	
${}^3P_1 \rightarrow {}^5P_1$	${}^3F_2 \rightarrow {}^5P_2$		-0.318			-0.106		-0.250				0.550	
${}^3P_2 \rightarrow {}^3P_2$	${}^3F_2 \rightarrow {}^5P_2$		0.026	-0.210		-0.026	0.210	0.062	-0.271			-0.136	0.192
${}^3P_2 \rightarrow {}^5P_2$	${}^3F_2 \rightarrow {}^5P_2$		-0.026	0.210		0.271	-0.210	-0.148	0.271			-0.037	-0.192
${}^3F_2 \rightarrow {}^3P_2$	${}^3F_2 \rightarrow {}^5P_2$	-0.150	-0.086	0.086	0.150	0.086	-0.086	-0.202	0.111			0.444	-0.078
${}^3F_2 \rightarrow {}^5P_2$	${}^3F_2 \rightarrow {}^5P_2$	0.075	0.043	-0.043	0.425	-0.443	0.043	0.242	-0.055			0.061	0.039
${}^3P_1 \rightarrow {}^3P_1$	${}^3F_3 \rightarrow {}^5P_3$		-0.383	-0.287		0.383	0.287	-0.429	-0.371			0.090	0.262
${}^3P_1 \rightarrow {}^5P_1$	${}^3F_3 \rightarrow {}^5P_3$		-1.029	0.129		-0.171	-0.129	-0.374	0.166			-0.323	-0.117
${}^3P_2 \rightarrow {}^3P_2$	${}^3F_3 \rightarrow {}^5P_3$		-0.148	-0.371		0.148	0.371	-0.227	-0.479			0.280	0.339
${}^3P_2 \rightarrow {}^5P_2$	${}^3F_3 \rightarrow {}^5P_3$		0.148	0.371		0.544	-0.371	-0.262	0.479			0.210	-0.339
${}^3F_2 \rightarrow {}^3P_2$	${}^3F_3 \rightarrow {}^5P_3$		-0.121	-0.303		0.121	0.303	-0.186	-0.391			0.229	0.277
${}^3F_2 \rightarrow {}^5P_2$	${}^3F_3 \rightarrow {}^5P_3$		0.121	0.303		0.444	-0.303	-0.214	0.391			0.171	-0.277
${}^3F_3 \rightarrow {}^5P_3$	${}^3F_3 \rightarrow {}^5P_3$	0.300	0.257	0.043	0.200	0.043	-0.043	0.182	0.055			-0.273	-0.039
${}^3P_1 \rightarrow {}^3P_1$	${}^3H_5 \rightarrow {}^5F_5$			-0.472		0.472		-0.518	-0.491			0.172	0.311
${}^3P_1 \rightarrow {}^5P_1$	${}^3H_5 \rightarrow {}^5F_5$			-1.338		-0.211		-0.368	0.220			-0.501	-0.139
${}^3P_2 \rightarrow {}^3P_2$	${}^3H_5 \rightarrow {}^5F_5$			-0.244		0.244		-0.354	-0.532			0.334	0.337
${}^3P_2 \rightarrow {}^5P_2$	${}^3H_5 \rightarrow {}^5F_5$			0.244		0.650		-0.339	0.532			0.401	-0.337
${}^3F_2 \rightarrow {}^3P_2$	${}^3H_5 \rightarrow {}^5F_5$			-0.199		0.199		-0.289	-0.435			0.273	0.275
${}^3F_2 \rightarrow {}^5P_2$	${}^3H_5 \rightarrow {}^5F_5$			0.199		0.531		-0.276	0.435			0.327	-0.275
${}^3F_3 \rightarrow {}^5P_3$	${}^3H_5 \rightarrow {}^5F_5$		1.107	0.443		0.553	-0.037	0.130	0.329			0.326	-0.273
${}^3H_5 \rightarrow {}^5F_5$	${}^3H_5 \rightarrow {}^5F_5$	0.333	0.364	0.252	0.167	0.136	0.021	0.129	0.163	0.091		-0.321	-0.192

TABLE III. (Continued).

W	W'^*	$P_y \rho_{11}(ST)$			$P_y \rho_{33}(ST)$			$P_y \rho_{31}(ST)$			$P_y \rho_{3-1}(ST)$		
		a_{10}^1	a_{10}^3	a_{10}^5	a_{10}^1	a_{10}^3	a_{10}^5	a_{00}^1	a_{00}^3	a_{00}^5	a_{01}^1	a_{01}^3	a_{01}^5
$^1S_0 \rightarrow ^5D_0$	$^3P_1 \rightarrow ^3P_1$							0.375					
$^1D_2 \rightarrow ^5S_2$	$^3P_1 \rightarrow ^3P_1$	0.184	0.300		-0.184	-0.300		0.075	0.300		-0.106	-0.173	
$^1G_4 \rightarrow ^5D_4$	$^3P_1 \rightarrow ^3P_1$		0.334	0.423		-0.334	-0.423	-0.100	0.256	0.445		-0.193	-0.244
$^1S_0 \rightarrow ^5D_0$	$^3P_1 \rightarrow ^5P_1$	-1.095						-0.168					
$^1D_2 \rightarrow ^5S_2$	$^3P_1 \rightarrow ^5P_1$	0.466	-0.134		0.082	0.134		-0.034	-0.134		0.522	0.077	
$^1G_4 \rightarrow ^5D_4$	$^3P_1 \rightarrow ^5P_1$		0.926	-0.189		0.149	0.189	-0.134	0.065	-0.199		0.604	0.109
$^1S_0 \rightarrow ^5D_0$	$^3P_2 \rightarrow ^3P_2$							0.290					
$^1D_2 \rightarrow ^5S_2$	$^3P_2 \rightarrow ^3P_2$	0.142	0.232		-0.142	-0.232		0.058	0.232		-0.082	-0.134	
$^1G_4 \rightarrow ^5D_4$	$^3P_2 \rightarrow ^3P_2$		0.259	0.327		-0.259	-0.327	-0.078	0.198	0.345		-0.149	-0.189
$^1S_0 \rightarrow ^5D_0$	$^3P_2 \rightarrow ^5P_2$							0.097				0.548	
$^1D_2 \rightarrow ^5S_2$	$^3P_2 \rightarrow ^5P_2$	-0.142	-0.232		-0.806	0.232		0.329	-0.232		-0.192	0.134	
$^1G_4 \rightarrow ^5D_4$	$^3P_2 \rightarrow ^5P_2$		-0.259	-0.327		-0.776	0.327	0.078	0.423	-0.345		-0.388	0.189
$^1S_0 \rightarrow ^5D_0$	$^3F_2 \rightarrow ^3P_2$							0.237					
$^1D_2 \rightarrow ^5S_2$	$^3F_2 \rightarrow ^3P_2$	0.116	0.190		-0.116	-0.190		0.047	0.190		-0.067	-0.110	
$^1G_4 \rightarrow ^5D_4$	$^3F_2 \rightarrow ^3P_2$		0.211	0.267		-0.211	-0.267	-0.063	0.162	0.282		-0.122	-0.154
$^1S_0 \rightarrow ^5D_0$	$^3F_2 \rightarrow ^5P_2$							0.079				0.447	
$^1D_2 \rightarrow ^5S_2$	$^3F_2 \rightarrow ^5P_2$	-0.116	-0.190		-0.658	0.190		0.269	-0.190		-0.157	0.110	
$^1G_4 \rightarrow ^5D_4$	$^3F_2 \rightarrow ^5P_2$		-0.211	-0.267		-0.634	0.267	0.063	0.345	-0.282		-0.317	0.154
$^1S_0 \rightarrow ^5D_0$	$^3F_3 \rightarrow ^5P_3$		1.342					-0.112	0.335			-0.158	0.387
$^1D_2 \rightarrow ^5S_2$	$^3F_3 \rightarrow ^5P_3$	0.657	0.402		0.438	-0.402		-0.179	0.402		0.411	-0.232	
$^1G_4 \rightarrow ^5D_4$	$^3F_3 \rightarrow ^5P_3$	-0.565	0.120	0.297	-0.314		-0.297	0.026	0.020	0.313	-0.435	-0.069	-0.171
$^1S_0 \rightarrow ^5D_0$	$^3H_5 \rightarrow ^5F_5$			1.826				-0.058	-0.135	0.481	-0.041	-0.233	0.527
$^1D_2 \rightarrow ^5S_2$	$^3H_5 \rightarrow ^5F_5$		1.155	0.548		0.577	-0.548	-0.144	-0.144	0.577	-0.041	0.600	-0.316
$^1G_4 \rightarrow ^5D_4$	$^3H_5 \rightarrow ^5F_5$	0.756	0.463	0.450	0.378	0.103	-0.125	-0.170	-0.010	0.227	0.480	0.071	-0.119

W	W'^*	$P_y \rho_{11}(TT)$			$P_y \rho_{33}(TT)$			$P_y \rho_{31}(TT)$			$P_y \rho_{3-1}(TT)$		
		a_{10}^2	a_{10}^4	a_{10}^6	a_{10}^2	a_{10}^4	a_{10}^6	a_{00}^0	a_{00}^2	a_{00}^4	a_{01}^2	a_{01}^4	a_{01}^6
$^3P_0 \rightarrow ^3P_0$	$^3P_1 \rightarrow ^3P_1$							-0.375					
$^3P_0 \rightarrow ^3P_0$	$^3P_1 \rightarrow ^5P_1$							0.168					
$^3P_0 \rightarrow ^3P_0$	$^3P_2 \rightarrow ^3P_2$	-1.095						0.097	-0.387				
$^3P_1 \rightarrow ^3P_1$	$^3P_2 \rightarrow ^3P_2$	-0.237			-0.712				0.335		-0.411		
$^3P_1 \rightarrow ^5P_1$	$^3P_2 \rightarrow ^3P_2$	-0.318			0.318				-0.150		-0.184		
$^3P_0 \rightarrow ^3P_0$	$^3P_2 \rightarrow ^5P_2$							0.032	-0.129		0.316		
$^3P_1 \rightarrow ^3P_1$	$^3P_2 \rightarrow ^5P_2$	0.237			-0.237			-0.112	0.112		0.137		
$^3P_1 \rightarrow ^5P_1$	$^3P_2 \rightarrow ^5P_2$	0.318			0.106			-0.150	0.150		-0.184		
$^3P_2 \rightarrow ^3P_2$	$^3P_2 \rightarrow ^5P_2$							0.029	-0.115		0.283		
$^3P_0 \rightarrow ^3P_0$	$^3F_2 \rightarrow ^3P_2$	-0.894						0.079	-0.316				
$^3P_1 \rightarrow ^3P_1$	$^3F_2 \rightarrow ^3P_2$	0.290			0.871				-0.411		0.503		
$^3P_1 \rightarrow ^5P_1$	$^3F_2 \rightarrow ^3P_2$	0.390			-0.390				0.184		0.225		
$^3P_2 \rightarrow ^3P_2$	$^3F_2 \rightarrow ^3P_2$	-0.339	-0.704		-0.161	0.704		0.071	0.126	-0.727	-0.093	0.407	
$^3P_2 \rightarrow ^5P_2$	$^3F_2 \rightarrow ^3P_2$	0.054	-0.235		-0.054	0.235			0.136	-0.242	-0.118	0.136	
$^3P_0 \rightarrow ^3P_0$	$^3F_2 \rightarrow ^5P_2$							0.026	-0.105		0.258		
$^3P_1 \rightarrow ^3P_1$	$^3F_2 \rightarrow ^5P_2$	-0.290			0.290			0.137	-0.137		-0.168		
$^3P_1 \rightarrow ^5P_1$	$^3F_2 \rightarrow ^5P_2$	-0.390			-0.130			0.184	-0.184		0.225		
$^3P_2 \rightarrow ^3P_2$	$^3F_2 \rightarrow ^5P_2$	0.054	-0.235		-0.054	0.235		-0.012	0.184	-0.242	-0.233	0.136	
$^3P_2 \rightarrow ^5P_2$	$^3F_2 \rightarrow ^5P_2$	-0.054	0.235		0.554	-0.235		0.035	-0.278	0.242	0.031	-0.136	
$^3F_2 \rightarrow ^3P_2$	$^3F_2 \rightarrow ^5P_2$							-0.029	0.115		-0.283		
$^3P_0 \rightarrow ^3P_0$	$^3F_3 \rightarrow ^5P_3$							-0.037	-0.186		0.456		
$^3P_2 \rightarrow ^3P_2$	$^3F_3 \rightarrow ^5P_3$	-0.121	-0.166		0.121	0.166		0.017	-0.045	-0.171	-0.012	0.096	
$^3P_2 \rightarrow ^5P_2$	$^3F_3 \rightarrow ^5P_3$	0.121	0.166		0.444	-0.166		-0.050	-0.121	0.171	-0.070	-0.096	
$^3F_2 \rightarrow ^3P_2$	$^3F_3 \rightarrow ^5P_3$	0.148	0.203		-0.148	-0.203		-0.020	0.055	0.210	0.014	-0.117	
$^3F_2 \rightarrow ^5P_2$	$^3F_3 \rightarrow ^5P_3$	-0.148	-0.203		-0.544	0.203		0.061	0.149	-0.210	0.086	0.117	
$^3P_0 \rightarrow ^3P_0$	$^3H_5 \rightarrow ^5F_5$							-0.019	-0.096	-0.173	0.118	0.387	
$^3P_2 \rightarrow ^3P_2$	$^3H_5 \rightarrow ^5F_5$	-0.109	-0.132			0.109	0.132	-0.004	-0.022	-0.092	0.105	0.063	0.076
$^3P_2 \rightarrow ^5P_2$	$^3H_5 \rightarrow ^5F_5$		0.109	0.132		0.291	-0.132	-0.013	-0.065	-0.063		-0.063	-0.076
$^3F_2 \rightarrow ^3P_2$	$^3H_5 \rightarrow ^5F_5$		0.134	0.161		-0.134	-0.161	0.005	0.026	0.112	-0.129	-0.077	-0.093
$^3F_2 \rightarrow ^5P_2$	$^3H_5 \rightarrow ^5F_5$	-0.134	-0.161			-0.356	0.161	0.016	0.079	0.078	0.077	0.093	

TABLE III. (Continued).

W	W'^*	$P_x \rho_{31}(ST)$			$P_x \rho_{3-1}(ST)$			$P_z \rho_{31}(ST)$		$P_z \rho_{3-1}(ST)$	
		a_{00}^0	a_{00}^2	a_{00}^4	a_{01}^2	a_{01}^4	a_{01}^6	a_{01}^2	a_{01}^4	a_{02}^2	a_{02}^4
$^1D_2 \rightarrow ^5S_2$	$^3P_0 \rightarrow ^3P_0$							-0.354		0.707	
$^1G_4 \rightarrow ^5D_4$	$^3P_0 \rightarrow ^3P_0$								-0.518		0.732
$^1S_0 \rightarrow ^5D_0$	$^3P_1 \rightarrow ^3P_1$	-0.375									
$^1D_2 \rightarrow ^5S_2$	$^3P_1 \rightarrow ^3P_1$	-0.125	-0.250		0.306						
$^1G_4 \rightarrow ^5D_4$	$^3P_1 \rightarrow ^3P_1$	-0.033	-0.167	-0.401		0.448					
$^1S_0 \rightarrow ^5D_0$	$^3P_1 \rightarrow ^5P_1$	0.168									
$^1D_2 \rightarrow ^5S_2$	$^3P_1 \rightarrow ^5P_1$	-0.168	0.335		-0.411						
$^1G_4 \rightarrow ^5D_4$	$^3P_1 \rightarrow ^5P_1$	-0.045	-0.224	0.538		-0.601					
$^1S_0 \rightarrow ^5D_0$	$^3P_2 \rightarrow ^3P_2$	0.097	-0.387					0.474			
$^1D_2 \rightarrow ^5S_2$	$^3P_2 \rightarrow ^3P_2$	-0.097	-0.194		0.237			0.158		-0.316	
$^1G_4 \rightarrow ^5D_4$	$^3P_2 \rightarrow ^3P_2$	-0.026	-0.307	-0.133	0.362	0.149		-0.145	0.033	0.181	-0.047
$^1S_0 \rightarrow ^5D_0$	$^3P_2 \rightarrow ^5P_2$	0.032	-0.129		-0.316			0.158		0.632	
$^1D_2 \rightarrow ^5S_2$	$^3P_2 \rightarrow ^5P_2$	-0.161	0.065		-0.079			0.158		-0.316	
$^1G_4 \rightarrow ^5D_4$	$^3P_2 \rightarrow ^5P_2$	0.026	-0.226	0.044	0.217	-0.050		-0.290	0.298	0.109	-0.421
$^1S_0 \rightarrow ^5D_0$	$^3F_2 \rightarrow ^3P_2$	0.079	-0.316					-0.581			
$^1D_2 \rightarrow ^5S_2$	$^3F_2 \rightarrow ^3P_2$	-0.079	-0.158		0.194			-0.194		0.387	
$^1G_4 \rightarrow ^5D_4$	$^3F_2 \rightarrow ^3P_2$	-0.021	-0.251	-0.109	0.296	0.121		0.177	-0.040	-0.222	0.057
$^1S_0 \rightarrow ^5D_0$	$^3F_2 \rightarrow ^5P_2$	0.026	-0.105		-0.258			-0.194		-0.775	
$^1D_2 \rightarrow ^5S_2$	$^3F_2 \rightarrow ^5P_2$	-0.132	0.053		-0.065			-0.194		0.387	
$^1G_4 \rightarrow ^5D_4$	$^3F_2 \rightarrow ^5P_2$	0.021	-0.184	0.036	0.177	-0.040		0.355	-0.364	-0.133	0.515
$^1S_0 \rightarrow ^5D_0$	$^3F_3 \rightarrow ^5P_3$	-0.037	-0.186		-0.456						
$^1D_2 \rightarrow ^5S_2$	$^3F_3 \rightarrow ^5P_3$	-0.149	-0.075		0.091						
$^1G_4 \rightarrow ^5D_4$	$^3F_3 \rightarrow ^5P_3$	0.060	-0.213	-0.205	0.314	0.229					
$^1S_0 \rightarrow ^5D_0$	$^3H_5 \rightarrow ^5F_5$	-0.019	-0.096	-0.173	-0.118	-0.387					
$^1D_2 \rightarrow ^5S_2$	$^3H_5 \rightarrow ^5F_5$	-0.048	-0.241		-0.118						
$^1G_4 \rightarrow ^5D_4$	$^3H_5 \rightarrow ^5F_5$	-0.108	-0.154	-0.130	0.126	0.132	0.076				

W	W'^*	$P_x \rho_{31}(TT)$			$P_x \rho_{3-1}(TT)$			$P_z \rho_{31}(TT)$		$P_z \rho_{3-1}(TT)$	
		a_{00}^1	a_{00}^3	a_{00}^5	a_{01}^1	a_{01}^3	a_{01}^5	a_{01}^1	a_{01}^3	a_{02}^3	a_{02}^5
$^3P_0 \rightarrow ^3P_0$	$^3P_1 \rightarrow ^3P_1$	0.375									
$^3P_0 \rightarrow ^3P_0$	$^3P_1 \rightarrow ^5P_1$	-0.168									
$^3P_1 \rightarrow ^3P_1$	$^3P_1 \rightarrow ^5P_1$							-0.411			
$^3P_0 \rightarrow ^3P_0$	$^3P_2 \rightarrow ^3P_2$	0.290									
$^3P_1 \rightarrow ^3P_1$	$^3P_2 \rightarrow ^3P_2$	-0.134	-0.201		0.142	0.232		0.142	0.232	-0.367	
$^3P_1 \rightarrow ^5P_1$	$^3P_2 \rightarrow ^3P_2$	0.240	-0.090		0.064	0.104		-0.255	0.104	-0.164	
$^3P_0 \rightarrow ^3P_0$	$^3P_2 \rightarrow ^5P_2$	0.097			-0.548						
$^3P_1 \rightarrow ^3P_1$	$^3P_2 \rightarrow ^5P_2$	-0.067	0.067		-0.047	-0.077		-0.285	-0.077	0.122	
$^3P_1 \rightarrow ^5P_1$	$^3P_2 \rightarrow ^5P_2$	-0.030	0.030		0.403	-0.035		-0.445	-0.035	0.055	
$^3P_2 \rightarrow ^3P_2$	$^3P_2 \rightarrow ^5P_2$	-0.121	0.208		0.098	-0.240		0.037	-0.240	0.379	
$^3P_0 \rightarrow ^3P_0$	$^3F_2 \rightarrow ^3P_2$	0.237									
$^3P_1 \rightarrow ^3P_1$	$^3F_2 \rightarrow ^3P_2$	0.164	0.246		-0.174	-0.285		0.116	0.190	-0.300	
$^3P_1 \rightarrow ^5P_1$	$^3F_2 \rightarrow ^3P_2$	-0.294	0.110		-0.078	-0.127		-0.208	0.085	-0.134	
$^3P_2 \rightarrow ^3P_2$	$^3F_2 \rightarrow ^3P_2$	0.212	0.318		-0.225	-0.367					
$^3P_2 \rightarrow ^5P_2$	$^3F_2 \rightarrow ^3P_2$	-0.042	0.148		0.195	-0.171		-0.030	0.196	-0.310	
$^3P_0 \rightarrow ^3P_0$	$^3F_2 \rightarrow ^5P_2$	0.079			-0.447						
$^3P_1 \rightarrow ^3P_1$	$^3F_2 \rightarrow ^5P_2$	0.082	-0.082		0.058	0.095		-0.232	-0.063	0.100	
$^3P_1 \rightarrow ^5P_1$	$^3F_2 \rightarrow ^5P_2$	0.037	-0.037		-0.494	0.042		-0.364	-0.028	0.045	
$^3P_2 \rightarrow ^3P_2$	$^3F_2 \rightarrow ^5P_2$	0.007	0.064		0.155	-0.073		0.030	-0.196	0.310	
$^3P_2 \rightarrow ^5P_2$	$^3F_2 \rightarrow ^5P_2$	0.106	-0.106		0.075	0.122					
$^3F_2 \rightarrow ^3P_2$	$^3F_2 \rightarrow ^5P_2$	0.121	-0.208		-0.098	0.240		0.024	-0.160	0.253	
$^3P_0 \rightarrow ^3P_0$	$^3F_3 \rightarrow ^5P_3$	-0.112	0.335		0.158	-0.387					
$^3P_1 \rightarrow ^3P_1$	$^3F_3 \rightarrow ^5P_3$							0.224		-0.354	
$^3P_1 \rightarrow ^5P_1$	$^3F_3 \rightarrow ^5P_3$							-0.500		0.791	
$^3P_2 \rightarrow ^3P_2$	$^3F_3 \rightarrow ^5P_3$	0.170	0.030		-0.198	-0.035		0.085	-0.035	0.055	
$^3P_2 \rightarrow ^5P_2$	$^3F_3 \rightarrow ^5P_3$	0.210	-0.210		-0.170	0.242		0.255	-0.104	0.164	
$^3F_2 \rightarrow ^3P_2$	$^3F_3 \rightarrow ^5P_3$	-0.208	-0.037		0.242	0.042		0.069	-0.028	0.045	
$^3F_2 \rightarrow ^5P_2$	$^3F_3 \rightarrow ^5P_3$	-0.257	0.257		0.208	-0.297		0.208	-0.085	0.134	
$^3P_0 \rightarrow ^3P_0$	$^3H_5 \rightarrow ^5F_5$	-0.058	-0.135	0.481	0.041	0.233	-0.527				

TABLE III. (Continued).

W	W'^*	$P_x \rho_{31}(TT)$			$P_x \rho_{3-1}(TT)$			$P_z \rho_{31}(TT)$			$P_z \rho_{3-1}(TT)$	
		a_{00}^1	a_{00}^3	a_{00}^5	a_{01}^1	a_{01}^3	a_{01}^5	a_{01}^1	a_{01}^3	a_{01}^5	a_{02}^3	a_{02}^5
${}^3P_1 \rightarrow {}^3P_1$	${}^3H_5 \rightarrow {}^5F_5$									0.365		-0.483
${}^3P_1 \rightarrow {}^5P_1$	${}^3H_5 \rightarrow {}^5F_5$									-0.653		0.864
${}^3P_2 \rightarrow {}^3P_2$	${}^3H_5 \rightarrow {}^5F_5$	-0.013	0.228	0.043	0.037	-0.239	-0.047		0.224		-0.283	
${}^3P_2 \rightarrow {}^5P_2$	${}^3H_5 \rightarrow {}^5F_5$	-0.039	0.340	-0.301		-0.298	0.330		0.373	-0.094	-0.189	0.125
${}^3F_2 \rightarrow {}^3P_2$	${}^3H_5 \rightarrow {}^5F_5$	0.016	-0.279	-0.053	-0.045	0.292	0.058		0.183		-0.231	
${}^3F_2 \rightarrow {}^5P_2$	${}^3H_5 \rightarrow {}^5F_5$	0.047	-0.416	0.369		0.365	-0.404		0.304	-0.077	-0.154	0.102
${}^3F_3 \rightarrow {}^5P_3$	${}^3H_5 \rightarrow {}^5F_5$								0.215	0.191	-0.476	-0.252

W	W'^*	$d\sigma/d\cos\theta_\Delta(SS)$			$A_y(ST)$		
		a_{00}^0	a_{00}^2	a_{00}^4	a_{10}^1	a_{10}^3	a_{10}^5
${}^1S_0 \rightarrow {}^5D_0$	${}^1S_0 \rightarrow {}^5D_0$	1.000					
${}^1S_0 \rightarrow {}^5D_0$	${}^1D_2 \rightarrow {}^5S_2$		2.000				
${}^1D_2 \rightarrow {}^5S_2$	${}^1D_2 \rightarrow {}^5S_2$	1.000					
${}^1S_0 \rightarrow {}^5D_0$	${}^1G_4 \rightarrow {}^5D_4$			3.207			
${}^1D_2 \rightarrow {}^5S_2$	${}^1G_4 \rightarrow {}^5D_4$		3.207				
${}^1G_4 \rightarrow {}^5D_4$	${}^1G_4 \rightarrow {}^5D_4$	1.000	1.020	0.551			
${}^1S_0 \rightarrow {}^5D_0$	${}^3P_1 \rightarrow {}^5P_1$				-2.191		
${}^1D_2 \rightarrow {}^5S_2$	${}^3P_1 \rightarrow {}^5P_1$				1.095		
${}^1G_4 \rightarrow {}^5D_4$	${}^3P_1 \rightarrow {}^5P_1$					2.151	
${}^1D_2 \rightarrow {}^5S_2$	${}^3P_2 \rightarrow {}^5P_2$				-1.897		
${}^1G_4 \rightarrow {}^5D_4$	${}^3P_2 \rightarrow {}^5P_2$					-2.070	
${}^1D_2 \rightarrow {}^5S_2$	${}^3F_2 \rightarrow {}^5P_2$				-1.549		
${}^1G_4 \rightarrow {}^5D_4$	${}^3F_2 \rightarrow {}^5P_2$					-1.690	
${}^1S_0 \rightarrow {}^5D_0$	${}^3F_3 \rightarrow {}^5P_3$					2.683	
${}^1D_2 \rightarrow {}^5S_2$	${}^3F_3 \rightarrow {}^5P_3$				2.191		
${}^1G_4 \rightarrow {}^5D_4$	${}^3F_3 \rightarrow {}^5P_3$				-1.757	0.239	
${}^1S_0 \rightarrow {}^5D_0$	${}^3H_5 \rightarrow {}^5F_5$						3.651
${}^1D_2 \rightarrow {}^5S_2$	${}^3H_5 \rightarrow {}^5F_5$					3.464	
${}^1G_4 \rightarrow {}^5D_4$	${}^3H_5 \rightarrow {}^5F_5$				2.268	1.132	0.651

W	W'^*	$d\sigma/d\cos\theta_\Delta(TT)$			$A_y(TT)$	
		a_{00}^0	a_{00}^2	a_{00}^4	a_{10}^2	a_{10}^4
${}^3P_0 \rightarrow {}^3P_0$	${}^3P_0 \rightarrow {}^3P_0$	1.000				
${}^3P_1 \rightarrow {}^3P_1$	${}^3P_1 \rightarrow {}^3P_1$	1.000	0.500			
${}^3P_1 \rightarrow {}^5P_1$	${}^3P_1 \rightarrow {}^5P_1$	1.000	-0.100			
${}^3P_0 \rightarrow {}^3P_0$	${}^3P_2 \rightarrow {}^3P_2$		1.789		-2.191	
${}^3P_1 \rightarrow {}^3P_1$	${}^3P_2 \rightarrow {}^3P_2$		2.324		-1.897	
${}^3P_2 \rightarrow {}^3P_2$	${}^3P_2 \rightarrow {}^3P_2$	1.000	0.700			
${}^3P_1 \rightarrow {}^5P_1$	${}^3P_2 \rightarrow {}^5P_2$		-1.039		0.849	
${}^3P_2 \rightarrow {}^5P_2$	${}^3P_2 \rightarrow {}^5P_2$	1.000	-0.700			
${}^3P_0 \rightarrow {}^3P_0$	${}^3F_2 \rightarrow {}^3P_2$		-2.191		-1.789	
${}^3P_1 \rightarrow {}^3P_1$	${}^3F_2 \rightarrow {}^3P_2$		1.897		2.324	
${}^3P_2 \rightarrow {}^3P_2$	${}^3F_2 \rightarrow {}^3P_2$		-0.490		-1.000	
${}^3F_2 \rightarrow {}^3P_2$	${}^3F_2 \rightarrow {}^3P_2$	1.000	0.800			
${}^3P_1 \rightarrow {}^5P_1$	${}^3F_2 \rightarrow {}^5P_2$		-0.849		-1.039	
${}^3P_2 \rightarrow {}^5P_2$	${}^3F_2 \rightarrow {}^5P_2$		0.490		1.000	
${}^3F_2 \rightarrow {}^5P_2$	${}^3F_2 \rightarrow {}^5P_2$	1.000	-0.800			
${}^3P_1 \rightarrow {}^5P_1$	${}^3F_3 \rightarrow {}^5P_3$		-2.400			
${}^3P_2 \rightarrow {}^5P_2$	${}^3F_3 \rightarrow {}^5P_3$		1.386		1.131	
${}^3F_2 \rightarrow {}^5P_2$	${}^3F_3 \rightarrow {}^5P_3$		1.131		-1.386	
${}^3F_3 \rightarrow {}^5P_3$	${}^3F_3 \rightarrow {}^5P_3$	1.000	0.600			
${}^3P_1 \rightarrow {}^5P_1$	${}^3H_5 \rightarrow {}^5F_5$			-3.098		
${}^3P_2 \rightarrow {}^5P_2$	${}^3H_5 \rightarrow {}^5F_5$			1.789	0.800	
${}^3F_2 \rightarrow {}^5P_2$	${}^3H_5 \rightarrow {}^5F_5$			1.461	-0.980	
${}^3F_3 \rightarrow {}^5P_3$	${}^3H_5 \rightarrow {}^5F_5$		3.320	0.811		
${}^3H_5 \rightarrow {}^5F_5$	${}^3H_5 \rightarrow {}^5F_5$	1.000	1.000	0.545		

TABLE III. (Continued).

W	W'^*	$A_{xx}\rho_{11}(SS)$			$A_{yy}\rho_{11}(SS)$			$A_{zz}\rho_{11}(SS)$			$A_{xz}\rho_{11}(ST)$		
		a_{00}^0	a_{00}^2	a_{00}^4	a_{00}^0	a_{00}^2	a_{00}^4	a_{00}^0	a_{00}^2	a_{00}^4	a_{10}^1	a_{10}^3	a_{10}^5
$^1S_0 \rightarrow ^5D_0$	$^1S_0 \rightarrow ^5D_0$	-0.500			-0.500			-0.500					
$^1S_0 \rightarrow ^5D_0$	$^1D_2 \rightarrow ^5S_2$		-1.000			-1.000			-1.000				
$^1D_2 \rightarrow ^5S_2$	$^1D_2 \rightarrow ^5S_2$	-0.250	-0.250		-0.250	-0.250		-0.250	-0.250				
$^1S_0 \rightarrow ^5D_0$	$^1G_4 \rightarrow ^5D_4$			-1.604			-1.604			-1.604			
$^1D_2 \rightarrow ^5S_2$	$^1G_4 \rightarrow ^5D_4$		-1.031	-0.573		-1.031	-0.573		-1.031	-0.573			
$^1G_4 \rightarrow ^5D_4$	$^1G_4 \rightarrow ^5D_4$	-0.321	-0.383	-0.338	-0.321	-0.383	-0.338	-0.321	-0.383	-0.338			
$^1D_2 \rightarrow ^5S_2$	$^3P_1 \rightarrow ^3P_1$										-0.184	-0.300	
$^1G_4 \rightarrow ^5D_4$	$^3P_1 \rightarrow ^3P_1$										-0.334	-0.423	
$^1S_0 \rightarrow ^5D_0$	$^3P_1 \rightarrow ^5P_1$									1.095			
$^1D_2 \rightarrow ^5S_2$	$^3P_1 \rightarrow ^5P_1$									-0.466	0.134		
$^1G_4 \rightarrow ^5D_4$	$^3P_1 \rightarrow ^5P_1$										-0.926	0.189	
$^1D_2 \rightarrow ^5S_2$	$^3P_2 \rightarrow ^3P_2$									-0.142	-0.232		
$^1G_4 \rightarrow ^5D_4$	$^3P_2 \rightarrow ^3P_2$										-0.259	-0.327	
$^1D_2 \rightarrow ^5S_2$	$^3P_2 \rightarrow ^5P_2$									0.142	0.232		
$^1G_4 \rightarrow ^5D_4$	$^3P_2 \rightarrow ^5P_2$										0.259	0.327	
$^1D_2 \rightarrow ^5S_2$	$^3F_2 \rightarrow ^3P_2$									-0.116	-0.190		
$^1G_4 \rightarrow ^5D_4$	$^3F_2 \rightarrow ^3P_2$										-0.211	-0.267	
$^1D_2 \rightarrow ^5S_2$	$^3F_2 \rightarrow ^5P_2$									0.116	0.190		
$^1G_4 \rightarrow ^5D_4$	$^3F_2 \rightarrow ^5P_2$										0.211	0.267	
$^1S_0 \rightarrow ^5D_0$	$^3F_3 \rightarrow ^5P_3$										-1.342		
$^1D_2 \rightarrow ^5S_2$	$^3F_3 \rightarrow ^5P_3$									-0.657	-0.402		
$^1G_4 \rightarrow ^5D_4$	$^3F_3 \rightarrow ^5P_3$									0.565	-0.120	-0.297	
$^1S_0 \rightarrow ^5D_0$	$^3H_5 \rightarrow ^5F_5$											-1.826	
$^1D_2 \rightarrow ^5S_2$	$^3H_5 \rightarrow ^5F_5$											-1.155	-0.548
$^1G_4 \rightarrow ^5D_4$	$^3H_5 \rightarrow ^5F_5$									-0.756	-0.463	-0.450	

W	W'^*	$A_{xx}\rho_{11}(TT)$			$A_{yy}\rho_{11}(TT)$			$A_{zz}\rho_{11}(TT)$			$A_{xz}\rho_{11}(TT)$		
		a_{00}^0	a_{00}^2	a_{00}^4	a_{00}^0	a_{00}^2	a_{00}^4	a_{00}^0	a_{00}^2	a_{00}^4	a_{10}^2	a_{10}^4	a_{10}^6
$^3P_0 \rightarrow ^3P_0$	$^3P_0 \rightarrow ^3P_0$	0.500			0.500			-0.500					
$^3P_1 \rightarrow ^3P_1$	$^3P_1 \rightarrow ^3P_1$	-0.063	0.062		0.063	-0.062		0.125	0.062				
$^3P_1 \rightarrow ^3P_1$	$^3P_1 \rightarrow ^5P_1$	-0.168	0.168		0.168	-0.168		0.335	0.168				
$^3P_1 \rightarrow ^5P_1$	$^3P_1 \rightarrow ^5P_1$	0.088	-0.088		-0.088	0.088		0.425	-0.088				
$^3P_0 \rightarrow ^3P_0$	$^3P_2 \rightarrow ^3P_2$		0.894			0.894			-0.894		1.095		
$^3P_1 \rightarrow ^3P_1$	$^3P_2 \rightarrow ^3P_2$	0.097	-0.097		-0.097	0.097			0.290		-0.237		
$^3P_1 \rightarrow ^5P_1$	$^3P_2 \rightarrow ^3P_2$	0.130	-0.130		-0.130	0.130			0.390		-0.318		
$^3P_2 \rightarrow ^3P_2$	$^3P_2 \rightarrow ^3P_2$	-0.017	0.109	0.309	0.238	0.163		0.055	-0.034	-0.309	0.166	0.345	
$^3P_1 \rightarrow ^3P_1$	$^3P_2 \rightarrow ^5P_2$	-0.097	0.097		0.097	-0.097			-0.290		0.237		
$^3P_1 \rightarrow ^5P_1$	$^3P_2 \rightarrow ^5P_2$	-0.130	0.130		0.130	-0.130			-0.390		0.318		
$^3P_2 \rightarrow ^3P_2$	$^3P_2 \rightarrow ^5P_2$	-0.045	-0.161	0.206	-0.075	0.075		-0.030	0.011	-0.206	-0.052	0.230	
$^3P_2 \rightarrow ^5P_2$	$^3P_2 \rightarrow ^5P_2$	0.023	0.080	-0.103	0.038	-0.038		0.015	-0.005	0.103	0.026	-0.115	
$^3P_0 \rightarrow ^3P_0$	$^3F_2 \rightarrow ^3P_2$		-1.095			-1.095			1.095		0.894		
$^3P_1 \rightarrow ^3P_1$	$^3F_2 \rightarrow ^3P_2$	0.079	-0.079		-0.079	0.079			0.237		0.290		
$^3P_1 \rightarrow ^5P_1$	$^3F_2 \rightarrow ^3P_2$	0.106	-0.106		-0.106	0.106			0.318		0.390		
$^3P_2 \rightarrow ^3P_2$	$^3F_2 \rightarrow ^3P_2$	-0.478	-0.376	-0.126	-0.061	-0.289	-0.630	0.539	0.499	0.126	-0.068	-0.141	
$^3P_2 \rightarrow ^5P_2$	$^3F_2 \rightarrow ^3P_2$	0.086	-0.044	-0.042	0.061	0.149	-0.210	-0.147	-0.079	0.042	0.011	-0.047	
$^3F_2 \rightarrow ^3P_2$	$^3F_2 \rightarrow ^3P_2$	0.080	0.186	0.334	0.250	0.221	0.129	-0.055	-0.136	-0.334	-0.166	-0.345	
$^3P_1 \rightarrow ^3P_1$	$^3F_2 \rightarrow ^5P_2$	-0.079	0.079		0.079	-0.079			-0.237		-0.290		
$^3P_1 \rightarrow ^5P_1$	$^3F_2 \rightarrow ^5P_2$	-0.106	0.106		0.106	-0.106			-0.318		-0.390		
$^3P_2 \rightarrow ^3P_2$	$^3F_2 \rightarrow ^5P_2$	0.086	-0.044	-0.042	0.061	0.149	-0.210	-0.147	-0.079	0.042	0.011	-0.047	
$^3P_2 \rightarrow ^5P_2$	$^3F_2 \rightarrow ^5P_2$	-0.086	0.044	0.042	-0.061	-0.149	0.210	0.147	0.079	-0.042	-0.011	0.047	
$^3F_2 \rightarrow ^3P_2$	$^3F_2 \rightarrow ^5P_2$	-0.080	-0.143	0.223	-0.100	0.014	0.086	0.030	0.043	-0.223	0.052	-0.230	
$^3F_2 \rightarrow ^5P_2$	$^3F_2 \rightarrow ^5P_2$	0.040	0.071	-0.111	0.050	-0.007	-0.043	-0.015	-0.021	0.111	-0.026	0.115	
$^3P_1 \rightarrow ^3P_1$	$^3F_3 \rightarrow ^5P_3$	0.112	0.176	-0.287	-0.112	-0.176	0.287		-0.383	-0.287			
$^3P_1 \rightarrow ^5P_1$	$^3F_3 \rightarrow ^5P_3$	0.150	-0.279	0.129	-0.150	0.279	-0.129		-1.029	0.129			
$^3P_2 \rightarrow ^3P_2$	$^3F_3 \rightarrow ^5P_3$	0.087	-0.012	-0.074	-0.087	0.012	0.074		-0.148	-0.371	0.121	0.166	
$^3P_2 \rightarrow ^5P_2$	$^3F_3 \rightarrow ^5P_3$	-0.087	0.012	0.074	0.087	-0.012	-0.074		0.148	0.371	-0.121	-0.166	
$^3F_2 \rightarrow ^3P_2$	$^3F_3 \rightarrow ^5P_3$	0.071	-0.010	-0.061	-0.071	0.010	0.061		-0.121	-0.303	-0.148	-0.203	
$^3F_2 \rightarrow ^5P_2$	$^3F_3 \rightarrow ^5P_3$	-0.071	0.010	0.061	0.071	-0.010	-0.061		0.121	0.303	0.148	0.203	

TABLE III. (Continued).

W	W'^*	$A_{xx} \rho_{11}(TT)$			$A_{yy} \rho_{11}(TT)$			$A_{zz} \rho_{11}(TT)$			$A_{xz} \rho_{11}(TT)$		
		a_{00}^0	a_{00}^2	a_{00}^4	a_{00}^0	a_{00}^2	a_{00}^4	a_{00}^0	a_{00}^2	a_{00}^4	a_{10}^2	a_{10}^4	a_{10}^6
${}^3F_3 \rightarrow {}^5P_3$	${}^3F_3 \rightarrow {}^5P_3$	0.200	-0.029	-0.171	-0.200	0.029	0.171	0.300	0.257	0.043			
${}^3P_1 \rightarrow {}^3P_1$	${}^3H_5 \rightarrow {}^5F_5$	0.058	0.289	0.047	-0.058	-0.289	-0.047			-0.472			
${}^3P_1 \rightarrow {}^5P_1$	${}^3H_5 \rightarrow {}^5F_5$	0.077	0.387	-0.641	-0.077	-0.387	0.641			-1.338			
${}^3P_2 \rightarrow {}^3P_2$	${}^3H_5 \rightarrow {}^5F_5$	0.045	0.224	-0.085	-0.045	-0.224	0.085			-0.244	0.109	0.132	
${}^3P_2 \rightarrow {}^5P_2$	${}^3H_5 \rightarrow {}^5F_5$	-0.045	-0.224	0.085	0.045	0.224	-0.085			0.244	-0.109	-0.132	
${}^3F_2 \rightarrow {}^3P_2$	${}^3H_5 \rightarrow {}^5F_5$	0.037	0.183	-0.070	-0.037	-0.183	0.070			-0.199	-0.134	-0.161	
${}^3F_2 \rightarrow {}^5P_2$	${}^3H_5 \rightarrow {}^5F_5$	-0.037	-0.183	0.070	0.037	0.183	-0.070			0.199	0.134	0.161	
${}^3F_3 \rightarrow {}^5P_3$	${}^3H_5 \rightarrow {}^5F_5$	-0.103	0.590	-0.135	0.103	-0.590	0.135		1.107	0.443			
${}^3H_5 \rightarrow {}^5F_5$	${}^3H_5 \rightarrow {}^5F_5$	0.267	0.121	-0.048	-0.267	-0.121	0.048	0.333	0.364	0.252			

W	W'^*	$A_{xx} \rho_{33}(SS)$			$A_{yy} \rho_{33}(SS)$			$A_{zz} \rho_{33}(SS)$			$A_{xz} \rho_{33}(ST)$		
		a_{00}^0	a_{00}^2	a_{00}^4	a_{00}^0	a_{00}^2	a_{00}^4	a_{00}^0	a_{00}^2	a_{00}^4	a_{10}^1	a_{10}^3	a_{10}^5
${}^1D_2 \rightarrow {}^5S_2$	${}^1D_2 \rightarrow {}^5S_2$	-0.250	0.250		-0.250	0.250		-0.250	0.250				
${}^1D_2 \rightarrow {}^5S_2$	${}^1G_4 \rightarrow {}^5D_4$		-0.573	0.573		-0.573	0.573		-0.573	0.573			
${}^1G_4 \rightarrow {}^5D_4$	${}^1G_4 \rightarrow {}^5D_4$	-0.179	-0.128	0.063	-0.179	-0.128	0.063	-0.179	-0.128	0.063			
${}^1D_2 \rightarrow {}^5S_2$	${}^3P_1 \rightarrow {}^3P_1$										0.184	0.300	
${}^1G_4 \rightarrow {}^5D_4$	${}^3P_1 \rightarrow {}^3P_1$											0.334	0.423
${}^1D_2 \rightarrow {}^5S_2$	${}^3P_1 \rightarrow {}^5P_1$										-0.082	-0.134	
${}^1G_4 \rightarrow {}^5D_4$	${}^3P_1 \rightarrow {}^5P_1$											-0.149	-0.189
${}^1D_2 \rightarrow {}^5S_2$	${}^3P_2 \rightarrow {}^3P_2$										0.142	0.232	
${}^1G_4 \rightarrow {}^5D_4$	${}^3P_2 \rightarrow {}^3P_2$											0.259	0.327
${}^1D_2 \rightarrow {}^5S_2$	${}^3P_2 \rightarrow {}^5P_2$										0.806	-0.232	
${}^1G_4 \rightarrow {}^5D_4$	${}^3P_2 \rightarrow {}^5P_2$											0.776	-0.327
${}^1D_2 \rightarrow {}^5S_2$	${}^3F_2 \rightarrow {}^3P_2$										0.116	0.190	
${}^1G_4 \rightarrow {}^5D_4$	${}^3F_2 \rightarrow {}^3P_2$											0.211	0.267
${}^1D_2 \rightarrow {}^5S_2$	${}^3F_2 \rightarrow {}^5P_2$										0.658	-0.190	
${}^1G_4 \rightarrow {}^5D_4$	${}^3F_2 \rightarrow {}^5P_2$											0.634	-0.267
${}^1D_2 \rightarrow {}^5S_2$	${}^3F_3 \rightarrow {}^5P_3$										-0.438	0.402	
${}^1G_4 \rightarrow {}^5D_4$	${}^3F_3 \rightarrow {}^5P_3$										0.314		0.297
${}^1D_2 \rightarrow {}^5S_2$	${}^3H_5 \rightarrow {}^5F_5$											-0.577	0.548
${}^1G_4 \rightarrow {}^5D_4$	${}^3H_5 \rightarrow {}^5F_5$										-0.378	-0.103	0.125

W	W'^*	$A_{xx} \rho_{33}(TT)$			$A_{yy} \rho_{33}(TT)$			$A_{zz} \rho_{11}(TT)$			$A_{xz} \rho_{33}(TT)$		
		a_{00}^0	a_{00}^2	a_{00}^4	a_{00}^0	a_{00}^2	a_{00}^4	a_{00}^0	a_{00}^2	a_{00}^4	a_{10}^2	a_{10}^4	a_{10}^6
${}^3P_1 \rightarrow {}^3P_1$	${}^3P_1 \rightarrow {}^3P_1$	-0.188	0.188		0.188	-0.188		0.375	0.187				
${}^3P_1 \rightarrow {}^3P_1$	${}^3P_1 \rightarrow {}^5P_1$	0.168	-0.168		-0.168	0.168		-0.335	-0.168				
${}^3P_1 \rightarrow {}^5P_1$	${}^3P_1 \rightarrow {}^5P_1$	-0.038	0.038		0.038	-0.038		0.075	0.038				
${}^3P_1 \rightarrow {}^3P_1$	${}^3P_2 \rightarrow {}^3P_2$	0.290	-0.290		-0.290	0.290			0.871		-0.712		
${}^3P_1 \rightarrow {}^5P_1$	${}^3P_2 \rightarrow {}^3P_2$	-0.130	0.130		0.130	-0.130			-0.390		0.318		
${}^3P_2 \rightarrow {}^3P_2$	${}^3P_2 \rightarrow {}^3P_2$	0.068	0.241	-0.309	0.113	-0.113		0.045	-0.016	0.309	0.079	-0.345	
${}^3P_1 \rightarrow {}^3P_1$	${}^3P_2 \rightarrow {}^5P_2$	0.097	-0.097		-0.097	0.097			0.290		-0.237		
${}^3P_1 \rightarrow {}^5P_1$	${}^3P_2 \rightarrow {}^5P_2$	-0.043	0.043		0.043	-0.043			-0.130		0.106		
${}^3P_2 \rightarrow {}^3P_2$	${}^3P_2 \rightarrow {}^5P_2$	0.045	0.161	-0.206	0.075	-0.075		0.030	-0.011	0.206	0.052	-0.230	
${}^3P_2 \rightarrow {}^5P_2$	${}^3P_2 \rightarrow {}^5P_2$	0.328	-0.430	0.103	0.013	-0.013		0.085	0.055	-0.103	-0.271	0.115	
${}^3P_1 \rightarrow {}^3P_1$	${}^3F_2 \rightarrow {}^3P_2$	0.237	-0.237		-0.237	0.237			0.712		0.871		
${}^3P_1 \rightarrow {}^5P_1$	${}^3F_2 \rightarrow {}^3P_2$	-0.106	0.106		0.106	-0.106			-0.318		-0.390		
${}^3P_2 \rightarrow {}^3P_2$	${}^3F_2 \rightarrow {}^3P_2$	-0.257	0.131	0.126	-0.184	-0.446	0.630	0.441	0.236	-0.126	-0.032	0.141	
${}^3P_2 \rightarrow {}^5P_2$	${}^3F_2 \rightarrow {}^3P_2$	-0.086	0.044	0.042	-0.061	-0.149	0.210	0.147	0.079	-0.042	-0.011	0.047	
${}^3F_2 \rightarrow {}^3P_2$	${}^3F_2 \rightarrow {}^3P_2$	0.120	0.214	-0.334	0.150	-0.021	-0.129	-0.045	-0.064	0.334	-0.079	0.345	
${}^3P_1 \rightarrow {}^3P_1$	${}^3F_2 \rightarrow {}^5P_2$	0.079	-0.079		-0.079	0.079			0.237		0.290		
${}^3P_1 \rightarrow {}^5P_1$	${}^3F_2 \rightarrow {}^5P_2$	-0.035	0.035		0.035	-0.035			-0.106		-0.130		
${}^3P_2 \rightarrow {}^3P_2$	${}^3F_2 \rightarrow {}^5P_2$	-0.086	0.044	0.042	-0.061	-0.149	0.210	0.147	0.079	-0.042	-0.011	0.047	
${}^3P_2 \rightarrow {}^5P_2$	${}^3F_2 \rightarrow {}^5P_2$	-0.159	0.201	-0.042	-0.674	0.884	-0.210	0.833	-0.814	0.042	0.111	-0.047	
${}^3F_2 \rightarrow {}^3P_2$	${}^3F_2 \rightarrow {}^5P_2$	0.080	0.143	-0.223	0.100	-0.014	-0.086	-0.030	-0.043	0.223	-0.052	0.230	
${}^3F_2 \rightarrow {}^5P_2$	${}^3F_2 \rightarrow {}^5P_2$	0.360	-0.471	0.111	0.150	-0.193	0.043	-0.085	0.221	-0.111	0.271	-0.115	
${}^3P_1 \rightarrow {}^3P_1$	${}^3F_3 \rightarrow {}^5P_3$	-0.112	-0.176	0.287	0.112	0.176	-0.287		0.383	0.287			
${}^3P_1 \rightarrow {}^5P_1$	${}^3F_3 \rightarrow {}^5P_3$	0.050	0.079	-0.129	-0.050	-0.079	0.129		-0.171	-0.129			
${}^3P_2 \rightarrow {}^3P_2$	${}^3F_3 \rightarrow {}^5P_3$	-0.087	0.012	0.074	0.087	-0.012	-0.074	0.148	0.371		-0.121	-0.166	

TABLE III. (Continued).

W	W'^*	$A_{xx}\rho_{33}(TT)$			$A_{yy}\rho_{33}(TT)$			$A_{zz}\rho_{11}(TT)$			$A_{xz}\rho_{33}(TT)$		
		a_{00}^0	a_{20}^2	a_{40}^4	a_{00}^0	a_{20}^2	a_{40}^4	a_{00}^0	a_{20}^2	a_{40}^4	a_{10}^2	a_{40}^4	a_{60}^6
${}^3P_2 \rightarrow {}^5P_2$	${}^3F_3 \rightarrow {}^5P_3$	-0.260	0.334	-0.074	0.260	-0.334	0.074		0.544	-0.371	-0.444	0.166	
${}^3F_2 \rightarrow {}^3P_2$	${}^3F_3 \rightarrow {}^5P_3$	-0.071	0.010	0.061	0.071	-0.010	-0.061		0.121	0.303	0.148	0.203	
${}^3F_2 \rightarrow {}^5P_2$	${}^3F_3 \rightarrow {}^5P_3$	-0.212	0.273	-0.061	0.212	-0.273	0.061		0.444	-0.303	0.544	-0.203	
${}^3F_3 \rightarrow {}^5P_3$	${}^3F_3 \rightarrow {}^5P_3$		-0.171	0.171		0.171	-0.171	0.200	0.043	-0.043			
${}^3P_1 \rightarrow {}^3P_1$	${}^3H_5 \rightarrow {}^5F_5$	-0.058	-0.289	-0.047	0.058	0.289	0.047			0.472			
${}^3P_1 \rightarrow {}^5P_1$	${}^3H_5 \rightarrow {}^5F_5$	0.026	0.129	0.021	-0.026	-0.129	-0.021			-0.211			
${}^3P_2 \rightarrow {}^3P_2$	${}^3H_5 \rightarrow {}^5F_5$	-0.045	-0.224	0.085	0.045	0.224	-0.085			0.244		-0.109	-0.132
${}^3P_2 \rightarrow {}^5P_2$	${}^3H_5 \rightarrow {}^5F_5$	-0.075	-0.373	0.630	0.075	0.373	-0.630			0.650		-0.291	0.132
${}^3F_2 \rightarrow {}^3P_2$	${}^3H_5 \rightarrow {}^5F_5$	-0.037	-0.183	0.070	0.037	0.183	-0.070			0.199		0.134	0.161
${}^3F_2 \rightarrow {}^5P_2$	${}^3H_5 \rightarrow {}^5F_5$	-0.061	-0.304	0.515	0.061	0.304	-0.515			0.531		0.356	-0.161
${}^3F_3 \rightarrow {}^5P_3$	${}^3H_5 \rightarrow {}^5F_5$	-0.120	-0.049	-0.182	0.120	0.049	0.182		0.553	-0.037			
${}^3H_5 \rightarrow {}^5F_5$	${}^3H_5 \rightarrow {}^5F_5$	0.067	-0.121	-0.134	-0.067	0.121	0.134	0.167	0.136	0.021			

except for the s , p , and Δ isobar phases given by $e^{i\delta_{jl}}$; thus, it allows only $\text{Im}s^*\Delta$ and $\text{Im}p^*\Delta$ contributions to the spin correlations and predicts $A_y=0$. As shown below, this model is clearly inadequate to describe the large values of the spin correlations (including $A_y \sim 40\%$) observed in the experiment, and a more complex phase structure for the Δ production waves is required. However, the WM should provide an adequate description of the smaller amplitudes of Fig. 4(a), including the s - and p -wave isobar and the high-partial-wave Δ production. The WM also serves as a benchmark to estimate the number of waves needed for partial-wave analysis. It is worth noting that the WM correctly predicts dominance of the low-energy cross sections by the 1D_2 , 3F_3 , and 3P_2 partial waves, simply as a consequence of the helicity structure of

the pion-exchange amplitudes. The latter explains the strong correlations between the singlet (${}^1D_2, {}^1G_4, \dots$) and uncoupled triplet (${}^3F_3, {}^3H_5, \dots$) waves that are required by the elastic PSA.

We have not explicitly included the $pp \rightarrow \Delta^+p$ amplitudes of Fig. 4(b) in the pion-exchange model or in our partial-wave analysis. These contributions are potentially important because of the strong kinematical overlap between Δ^+p and $\Delta^{++}n$ final states in the $p\pi^+n$ Dalitz plot at low energies. In Appendix B we show how to compute the Δ^+p contributions, using Wick transformations,⁴² as a series of $s, p, \Delta, \dots, p\pi^+$ isobar waves. This analysis is independent of any specific model for Δ production and requires only isotopic spin and angular-momentum conservation. Our numerical calculations indicate that the Δ^+p and $\Delta^{++}n$ contributions to any given production wave are effectively in phase near the Δ^{++} mass. As a result, provided the observables are averaged over the Δ^{++} mass, we find that simply extending the WM to include Δ^+p and $\Delta^{++}n$ isobars cannot generate significant spin correlations (e.g., $|A_y| \leq 2\%$, averaged over the Δ^{++} band). Thus, large spin correlations require a nontrivial phase structure in the $\Delta^{++}n$ production waves, and cannot be obtained simply from the isobar phases implied by Figs. 4(a) and 4(b). In partial-wave analysis using data averaged over the Δ^{++} mass, the Δ^+p waves need not be included explicitly; their contributions are included implicitly in any empirical expansion in s , p , and $\Delta p\pi^+$ isobars.

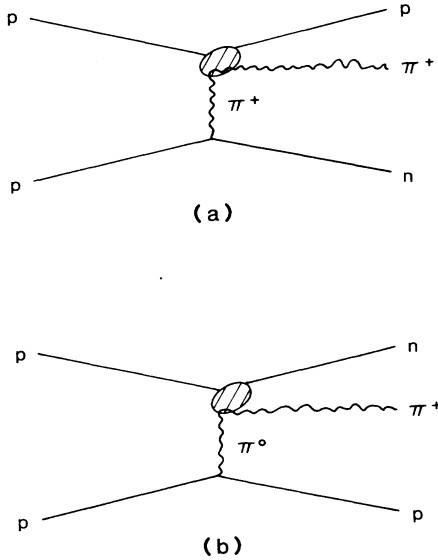


FIG. 4. Diagrams for (a) charged and (b) neutral-pion-exchange Born terms.

IV. MASS AND PRODUCTION-ANGLE DEPENDENCE OF THE OBSERVABLES

In this section we survey the dependence of the observables on $\cos\Theta_\Delta$ and $M_{p\pi^+}$, and show comparisons with the pion-exchange and joint-moments fits. As noted above, these fits were performed with data averaged over the Δ^{++} band, namely, the mass intervals $1.18 < M_{p\pi^+} < 1.28$ GeV for $P_{\text{lab}} = 1.47, 1.71, \text{ and } 1.98$ GeV/c, and $1.16 < M_{p\pi^+} < 1.20$ GeV for $p_{\text{lab}} = 1.18$

TABLE IV. Pion-exchange fit parameters at each energy, and values of C_M obtained from crossing matrices evaluated at the center of the Δ^{++} band ($M_{p\pi^+} = 1.18$ GeV at 1.18 GeV/c, and $M_{p\pi^+} = 1.23$ GeV at 1.47, 1.71, and 1.98 GeV/c). The parameters are defined by Eqs. (A2) and (A6); C_M are defined by Eq. (A4) in the limit $t' \rightarrow 0$ for the s -, p -, and Δ -isobar production amplitudes.

	1.18 GeV/c	1.47 GeV/c	1.71 GeV/c	1.98 GeV/c	6 GeV/c
G (mb ^{1/2})	2.97	1.97	2.32	2.25	3.04
B (GeV ⁻²)	0.90	0.21	-0.32	-0.24	2.79
B_- (GeV ⁻²)	0.50	1.89	4.06	4.58	6.71
B_+ (GeV ⁻²)	0.20	1.10	2.67	4.24	6.60
S	0.35	0.75	0.70	0.94	1.07
$C_{3/2}^{\Delta}$ (GeV ^{-1/2})	4.88	3.87	3.72	3.70	3.55
$C_{-1/2}^{\Delta}$ (GeV ^{-1/2})	-4.85	-3.62	-3.26	-3.10	-2.65
$C_{-1/2}^s$ (GeV ^{-1/2})	-2.10	-1.41	-1.12	-0.97	-0.61
$C_{-1/2}^p$ (GeV ^{-1/2})	-3.60	-3.07	-3.18	-3.30	-3.49

GeV/c. Accordingly, we will focus on the $\cos\Theta_{\Delta}$ dependence for these intervals. We remark that those observables which allow Δ - Δ interference contributions show only modest $M_{p\pi^+}$ dependence in the Δ^{++} band.

A. Cross sections and integrated asymmetries

The differential cross sections $d\sigma/d\cos\Theta_{\Delta}$ and $d\sigma/dM_{p\pi^+}$ are shown in Figs. 5 and 6, respectively, together with the pion-exchange fits; Figs. 6(a) and 6(b) show $d\sigma/dM_{p\pi^+}$ for two slices in $\cos\Theta_{\Delta}$: namely, (a) $0.5 < \cos\Theta_{\Delta} < 1.0$ and (b) $-0.5 < \cos\Theta_{\Delta} < 0.5$. As expected, $d\sigma/d\cos\Theta_{\Delta}$ becomes more collimated with increasing p_{lab} , and $d\sigma/dM_{p\pi^+}$ shows a strong Δ^{++} peak at all energies, although of course only the low side of the Δ^{++} can be seen at 1.18 GeV/c. We remark that the mass dependence predicted by the pion-exchange parametrization is governed by the π^+p elastic phase shifts [cf. Eq. (A2)] and was not fitted to the data; the quantitative agreement with the mass spectra of Fig. 6 is obviously rather poor.

The integrated asymmetry A_y [defined in Eq. (22)] is plotted against $\cos\Theta_{\Delta}$ in Fig. 7 for the Δ^{++} band, together with the joint-moments fits. The pion-exchange predictions from our parametrization are, trivially, $A_y = 0$, which is clearly not the case. Since A_y reflects $\text{Im}(\Delta^* \Delta' + s^* s' + p^* p')$ interference contributions, the large values of A_y suggest large $\Delta^* \Delta'$ interference and hence a nontrivial phase structure for the Δ -production waves. Two other features of A_y are noteworthy: (1) A_y is approximately symmetric in $\cos\Theta_{\Delta}$ at all energies, indicating a predominance of singlet-triplet interference contributions, and (2) A_y changes sign with increasing p_{lab} ; it is positive for all $\cos\Theta_{\Delta}$ at 1.18 GeV/c, while at the higher momenta it is negative except for very forward $\cos\Theta_{\Delta}$. This latter feature suggests either strong energy dependence in the relative phases of the larger waves, or

strong energy dependence in the mix of waves which contribute to A_y .

To illustrate the $M_{p\pi^+}$ dependence of A_y , Fig. 8 shows A_y plotted against $\cos\Theta_{\Delta}$ for 40-MeV slices in $M_{p\pi^+}$. The mass dependence is fairly adiabatic. Of course, some mass dependence would be expected from the Δ^{++} - Δ^+ interference contributions, as discussed in Sec. III E; also, simple Q^{L_f} -barrier factors might be expected to cause some mass dependence in the singlet-triplet interferences,

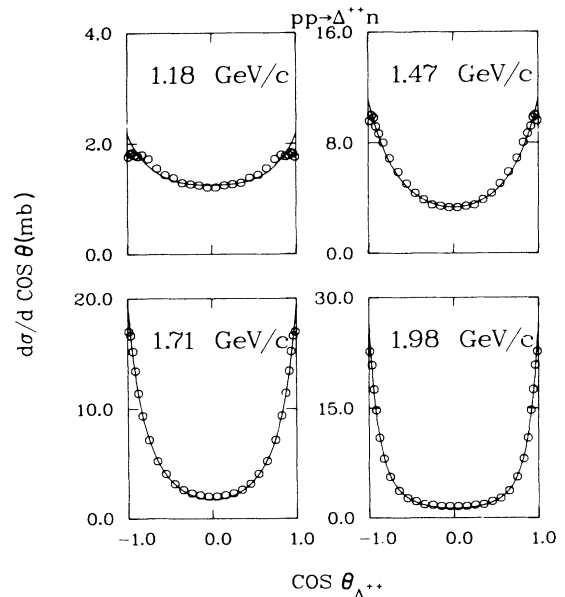


FIG. 5. Differential cross sections $d\sigma/d\cos\Theta_{\Delta}$ together with pion-exchange fits (solid curves); the cross sections are integrated over the Δ^{++} bands, namely, $1.16 < M_{p\pi^+} < 1.20$ GeV (1.18 GeV/c), and $1.18 < M_{p\pi^+} < 1.28$ GeV (1.47, 1.71, and 1.98 GeV/c).

since singlet and triplet waves have different L_f values. In any case, the gross features of A_y appear to be fairly stable over the Δ^{++} band.

B. Unpolarized density-matrix elements

As noted in Sec. III A, the pion-exchange parametrization takes a simpler form in the t -channel frame. Figures 9(a)–9(d) show the t -channel DME's ρ_{11} , ρ_{33} , ρ_{31} , and

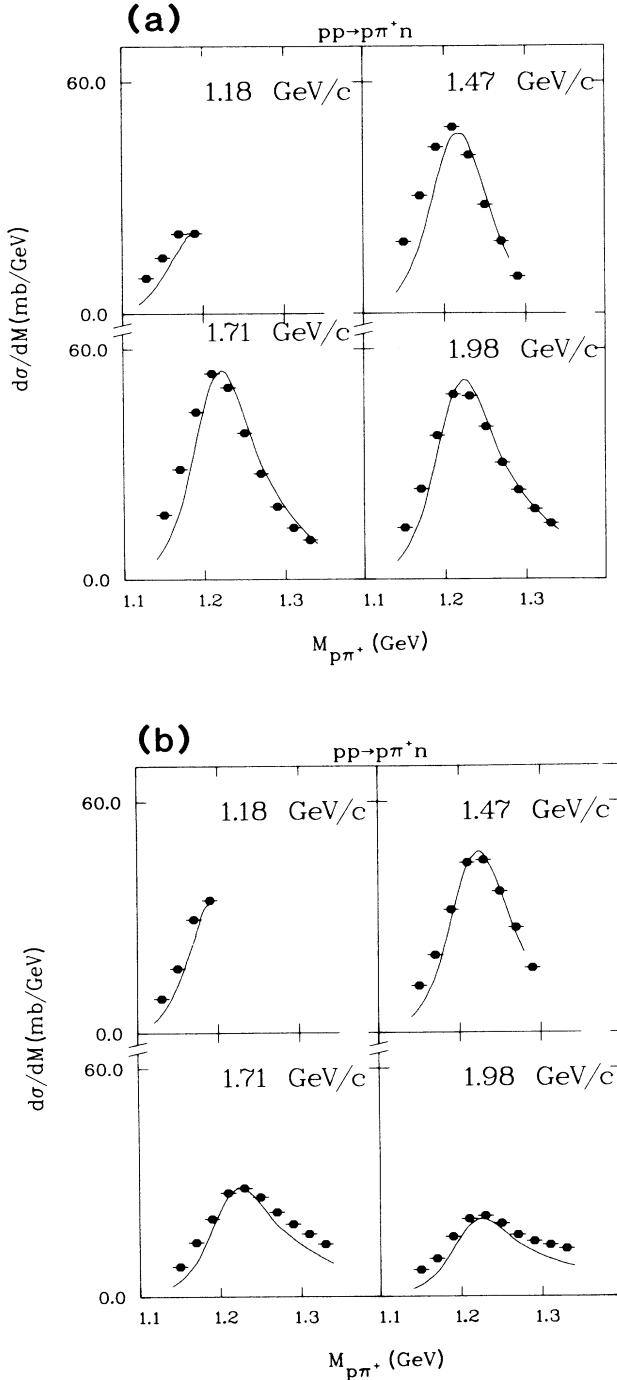


FIG. 6. $M_{p\pi^+}$ spectra, together with pion-exchange predictions, for (a) $\cos\Theta_\Delta > 0.5$, and (b) $-0.5 < \cos\Theta_\Delta < 0.5$.

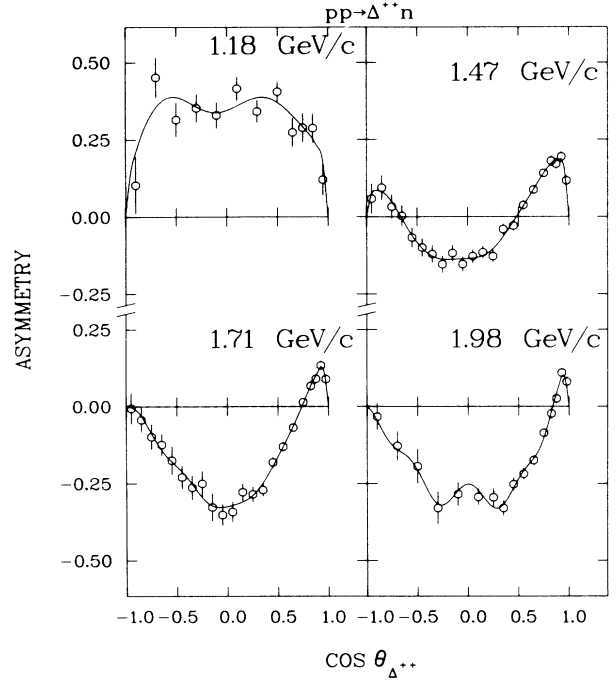


FIG. 7. Asymmetry parameter A_y plotted against $\cos\Theta_\Delta$ and integrated over the Δ^{++} bands as in Fig. 5. The solid curves indicate the joint-moments fits.

ρ_{3-1} in the Δ^{++} band plotted against $\cos\Theta_\Delta$, together with the pion-exchange fits. For comparison the 3–12-GeV/c data are also plotted (against $\sqrt{-t}$). Several features are evident: (a) ρ_{11} and ρ_{33} [Figs. 9(a) and (b)] vary slowly with $\cos\Theta_\Delta$ at the low energies, and are nearly constant for small momentum transfers at the higher energies; (b) ρ_{31} [Fig. 9(c)] is everywhere negative; (c) ρ_{3-1} [Fig. 9(d)] is close to zero for forward scattering at all momenta above 1.5 GeV/c. These features follow naturally from the pion-exchange parametrization. For example, the condition $\rho_{3-1} \approx 0$ follows, schematically, from the relation $\sigma\rho_{3-1} = \text{Re}(A^3 A^{-1*} + A^{-3} A^{1*})$, where we indicate only the Δ^{++} helicity label; in the pion-exchange parametrization, $A^{-3} = 0$ in the t channel, while with $B_+ = B_-$ in Eq. (A6), $\text{Re}(A^3 A^{-1*}) = 0$ after summing over target and recoil nucleon helicities. Overall, the data suggest a very gradual evolution of the DME's with p_{lab} .

The s -channel DME's, ρ_{11} , ρ_{33} , ρ_{31} , ρ_{3-1} , ρ_{s1} , and ρ_{s-1} , are plotted against $\cos\Theta_\Delta$ in Figs. 10(a)–10(f), respectively, together with the joint-moments fits (solid curves). The s -channel pion-exchange fits are indicated by the dashed curves for the 1.71-GeV/c data (they are qualitatively similar at the other momenta). In the s channel, the noteworthy features are (1) ρ_{11} and ρ_{33} vary strongly with $\cos\Theta_\Delta$ [Figs. 10(a) and 10(b)], (2) ρ_{31} is positive for $\cos\Theta_\Delta > 0$ [Fig. 10(c)] and is antisymmetric about $\Theta_\Delta = 90^\circ$ as required by the Pauli principle, and (3) ρ_{3-1} is nonzero [Fig. 10(d)]. The DME's ρ_{s1} and ρ_{s-1} shown in Figs. 10(e) and 10(f) are given by interferences involving $\text{Re}s^* \Delta$, and in the pion-exchange parametrization are pro-

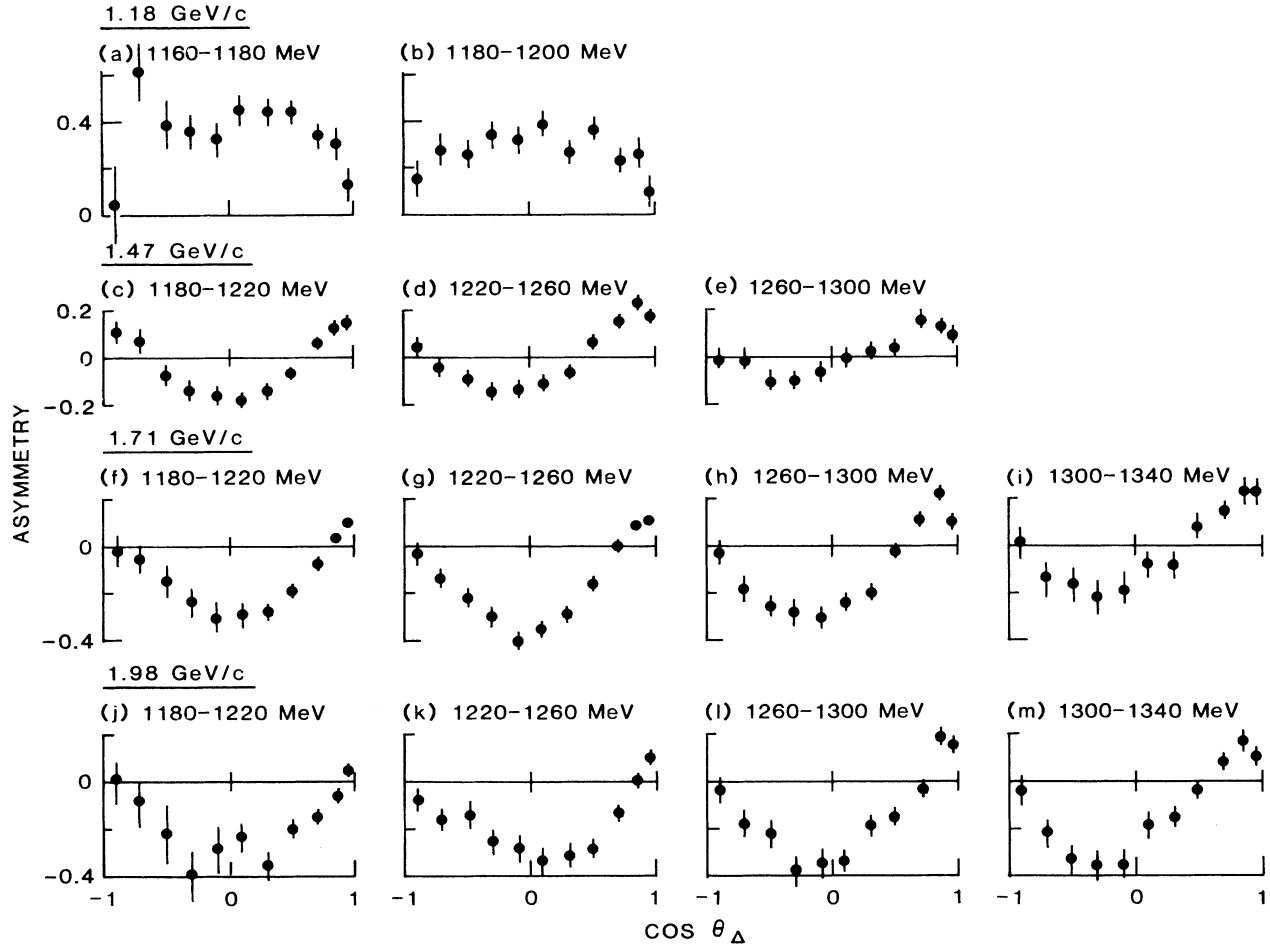


FIG. 8. Asymmetry parameter A_y plotted against $\cos\Theta_\Delta$ sliced in 40 MeV mass intervals.

portional to $\cos(\delta_\Delta - \delta_s)$; thus they are expected to exhibit strong $M_{p\pi^+}$ dependence (and do), and cancellations occur in averaging these observables over the Δ^{++} band. In general, whereas the behavior of the DME's is somewhat more complicated in the s channel, the joint-moments fits provide an adequate description of the $\cos\Theta_\Delta$ dependence.

C. Spin correlations

Figures 11(a)–11(b) show the spin correlations that allow Δ - Δ interference terms, namely, $P_y\rho_{11}$, $P_y\rho_{33}$, $P_y\rho_{31}$, $P_y\rho_{3-1}$, $P_x\rho_{31}$, $P_x\rho_{3-1}$, $P_z\rho_{31}$, and $P_z\rho_{3-1}$, respectively, plotted against $\cos\Theta_\Delta$. Again we display the joint-moment fits (solid curves) and the pion-exchange predictions at 1.71 GeV/c (dashed curves). Note that the pion-exchange predictions, which include only p - Δ interference contributions, are generally too small to describe the data well. These p - Δ interference contributions are maximal in the sense that the p and Δ isobars are $\sim 90^\circ$ out of phase in the WM near the Δ^{++} mass. Thus, as with A_y , it appears that the bulk of the spin-correlation data must be

due to Δ - Δ interferences, and cannot be attributed solely to the interference of different isobar configurations.

The energy dependence of $P_y\rho_{11}$ [Fig. 11(a)] and $P_y\rho_{33}$ [Fig. 11(b)] is noteworthy. Whereas $P_y\rho_{11}$ is generally positive and falls gradually with increasing p_{lab} , $P_y\rho_{33}$ changes sign from positive to negative between 1.18 and 1.47 GeV/c. The combination of these effects is responsible for the energy dependence noted above for $A_y = 2P_y\rho_{11} + 2P_y\rho_{33}$. This rather striking behavior immediately rules out the possibility that A_y is a reflection of the interference of two dominant waves (e.g., 1D_2 and 3F_3); if this were the case, then A_y , $P_y\rho_{11}$, and $P_y\rho_{33}$ would all exhibit the same p_{lab} dependence. The different p_{lab} dependences observed for $P_y\rho_{11}$ and $P_y\rho_{33}$ suggest that the mix of Δ -production waves varies with p_{lab} .

For completeness we show the spin correlations which are sensitive to s - Δ interference, namely, $P_y\rho_{s1}$, $P_y\rho_{s-1}$, $P_x\rho_{s-1}$, and $P_z\rho_{s-1}$ in Figs. 12(a)–12(d), respectively, together with the joint moments and pion-exchange curves. The pion-exchange predictions are not unreasonable for $P_y\rho_{s-1}$, $P_x\rho_{s-1}$, and $P_z\rho_{s-1}$, but do not describe $P_y\rho_{s1}$

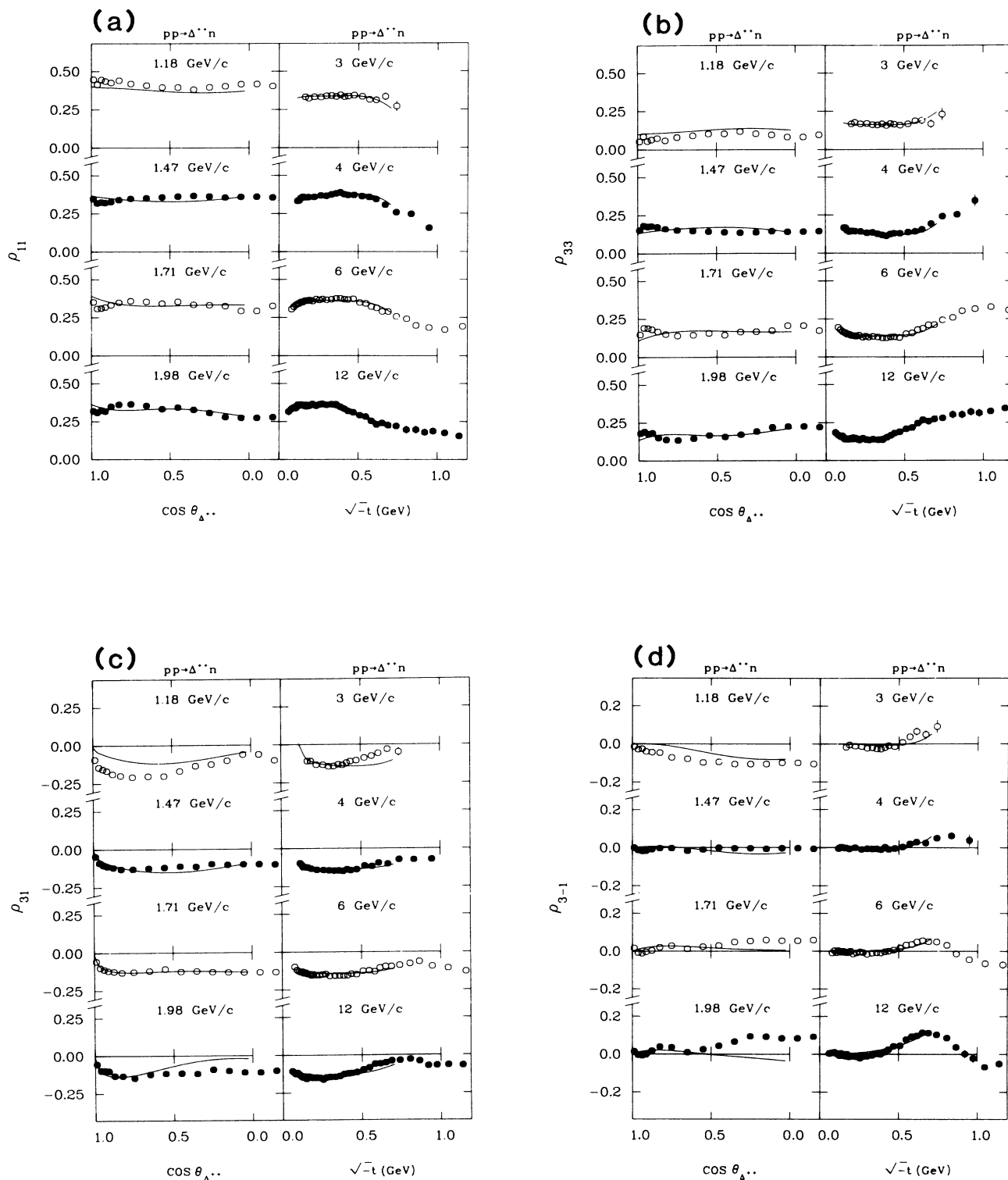


FIG. 9. t -channel DME's (a) ρ_{11} , (b) ρ_{33} , (c) ρ_{31} , and (d) ρ_{3-1} together with pion-exchange fits (solid curves) plotted against $\cos \theta_{\Delta}$ (1.18 to 1.98 GeV/c) and $\sqrt{-t}$ (3 to 12 GeV/c). The data are cut on the Δ^{++} band defined in Fig. 5 for the low-energy points and taken to be $1.15 < M_{p\pi^+} < 1.34$ GeV for the 3 to 12 GeV/c points.

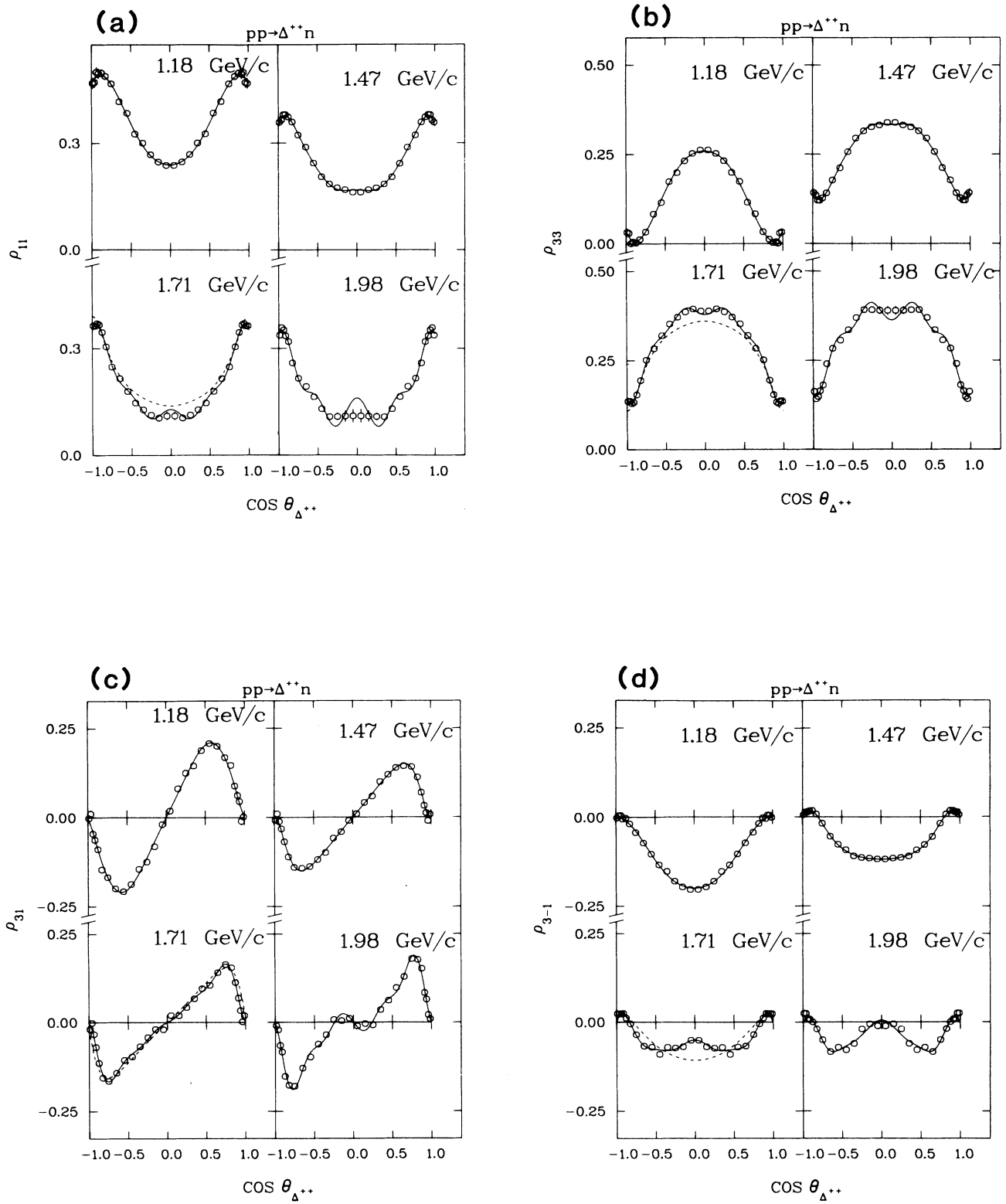


FIG. 10. s -channel DME's (a) ρ_{11} , (b) ρ_{33} , (c) ρ_{31} , (d) ρ_{3-1} , (e) ρ_{s1} , and (f) ρ_{s-1} , plotted against $\cos\Theta_{\Delta^{++}}$ (Δ^{++} -band cuts imposed). The solid curves show the joint-moments fits, and the dashed curves indicate the pion-exchange fits for 1.71 GeV/c.

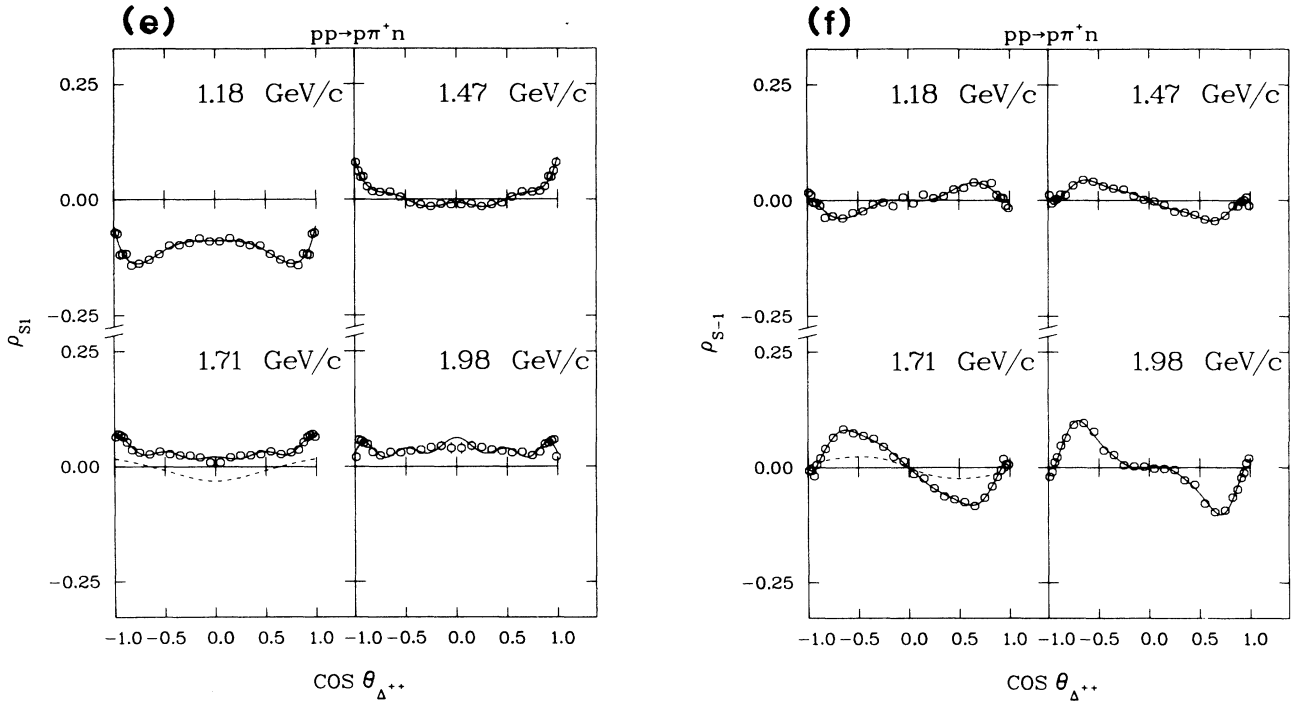


FIG. 10. (Continued).

well. Similar results were obtained in the 3–12 GeV/c analysis.² As noted in Ref. 2, $P_y\rho_{s-1}$ and $P_x\rho_{s-1}$ are expected to be the dominant $\text{Im}s^*\Delta$ interferences for small momentum transfers in the pion-exchange model; they are expected to be approximately mirror symmetric. Figure 13 shows these two spin correlations plotted against $\cos\Theta_\Delta$ for 1.18 to 1.98 GeV/c, and against $\sqrt{-t}$ for 3 to 12 GeV/c. The relative signs and magnitudes are in reasonable accord with the pion-exchange predictions at all energies. Of course, we would not expect quantitative agreement for the $s^*\Delta$ interference terms, because the pion-exchange model evidently fails to describe the Δ -production phases correctly, as evidenced by the large values of A_y . However, the model seems to describe correctly the approximate scale of the $\text{Im}s^*\Delta$ terms, and so should be adequate in estimating the magnitude of the $\text{Im}p^*\Delta$ terms.

D. Other comparisons with 3–12-GeV/c data

In Ref. 2 we noted the following regularities at 6 and 12 GeV/c for $-t < 1 \text{ GeV}^2$:

$$P_x\rho_{31} \simeq -P_z\rho_{3-1}, \quad (38a)$$

$$P_x\rho_{3-1} \simeq P_z\rho_{31}. \quad (38b)$$

These relations would hold if the spin correlations were due to interferences of unnatural-parity amplitudes, for example, π and B exchange. The relations would have

opposite signs for natural-parity interferences. Figure 14 illustrates this comparison for 6 GeV/c, plotted against $\sqrt{-t}$, and 1.47 GeV/c, plotted against $\cos\Theta_\Delta$. The patterns are qualitatively similar at the two energies, again suggesting a rather gradual p_{lab} dependence for the small- t production mechanisms. We note that the predominance of unnatural-parity interferences in the spin correlations has a natural explanation in the additive quark model, as discussed in Ref. 2.

Figure 15 provides a more global view of the overall energy dependence of the Δ - Δ interference SSC's. Guided by the momentum-transfer dependence of the 3–12 GeV/c data, we have selected two momentum-transfer intervals: $-t < 0.2 \text{ GeV}^2$ and $0.28 < -t < 0.6 \text{ GeV}^2$; we have averaged the DME's over these intervals and plotted them against p_{lab} , with smooth polynomial curves to help guide the eye. The SSC's exhibit reasonable continuity with p_{lab} , although some of the individual correlations (notably $P_y\rho_{11}$ and $P_y\rho_{33}$) exhibit marked energy dependence, as anticipated in the discussion above.

E. Summary

This survey suggests the following features. (1) The pion-exchange model provides a fair description of the unpolarized cross sections and DME's, and these show only gradual p_{lab} dependence from 1.2 to 2 GeV/c. (2) The pion-exchange model describes qualitatively some of the polarization effects associated with s - Δ interference, and may therefore provide an adequate description of the small s - and p -wave isobar production amplitudes. (3)

The large values of A_y , and also the discrepancies between the SSC's and the p - Δ interference predictions from the pion-exchange model, suggest the dominance of Δ - Δ interference contributions in the SSC's. (4) The Δ - Δ spin correlations exhibit significant p_{lab} dependence at low energies, especially $P_y\rho_{33}$; nonetheless, the SSC's show reasonable continuity from 1.2 to 12 GeV/c.

V. FINAL-STATE-INTERACTION EFFECTS

This section covers two aspects of final-state interactions between the proton and neutron. The first concerns the relationship between $pp \rightarrow \pi^+d$ and $pp \rightarrow p\pi^+n$, as evidenced by the spin correlations. The second concerns the distortions in the DME's caused by the proton-neutron threshold enhancement in the $pn\pi^+$ final state, an effect which has been clearly seen in several other experiments.^{6,9,43} We discuss these two topics in turn.

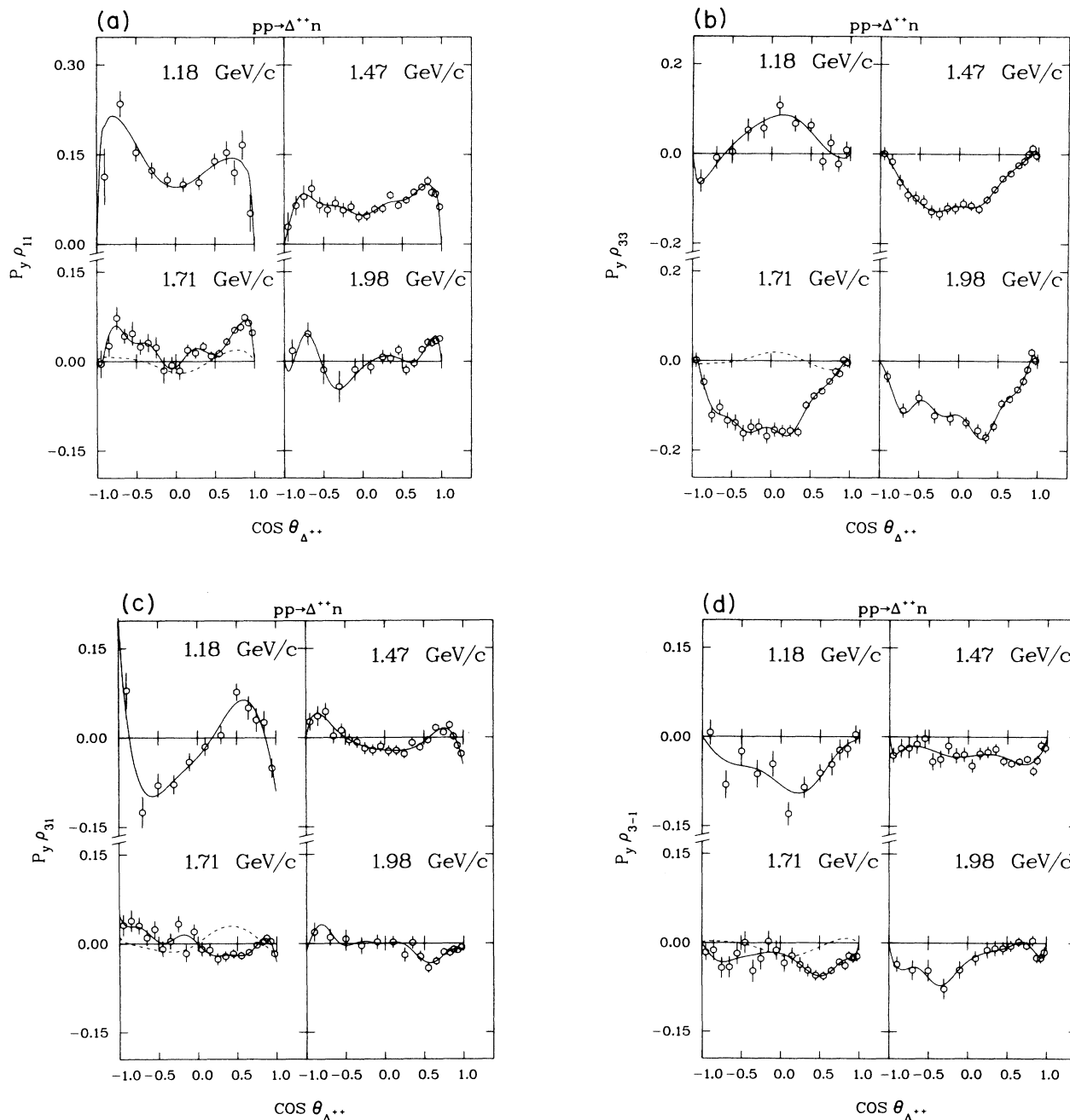


FIG. 11. s -channel spin correlations (a) $P_y\rho_{11}$, (b) $P_y\rho_{33}$, (c) $P_y\rho_{31}$, (d) $P_y\rho_{3-1}$, (e) $P_x\rho_{31}$, (f) $P_x\rho_{3-1}$, (g) $P_z\rho_{31}$, and (h) $P_z\rho_{3-1}$ plotted against $\cos\theta_{\Delta^{++}}$ (Δ^{++} -band cuts imposed). The solid curves show the joint-moments fits and the dashed curves the pion-exchange predictions for 1.71 GeV/c.

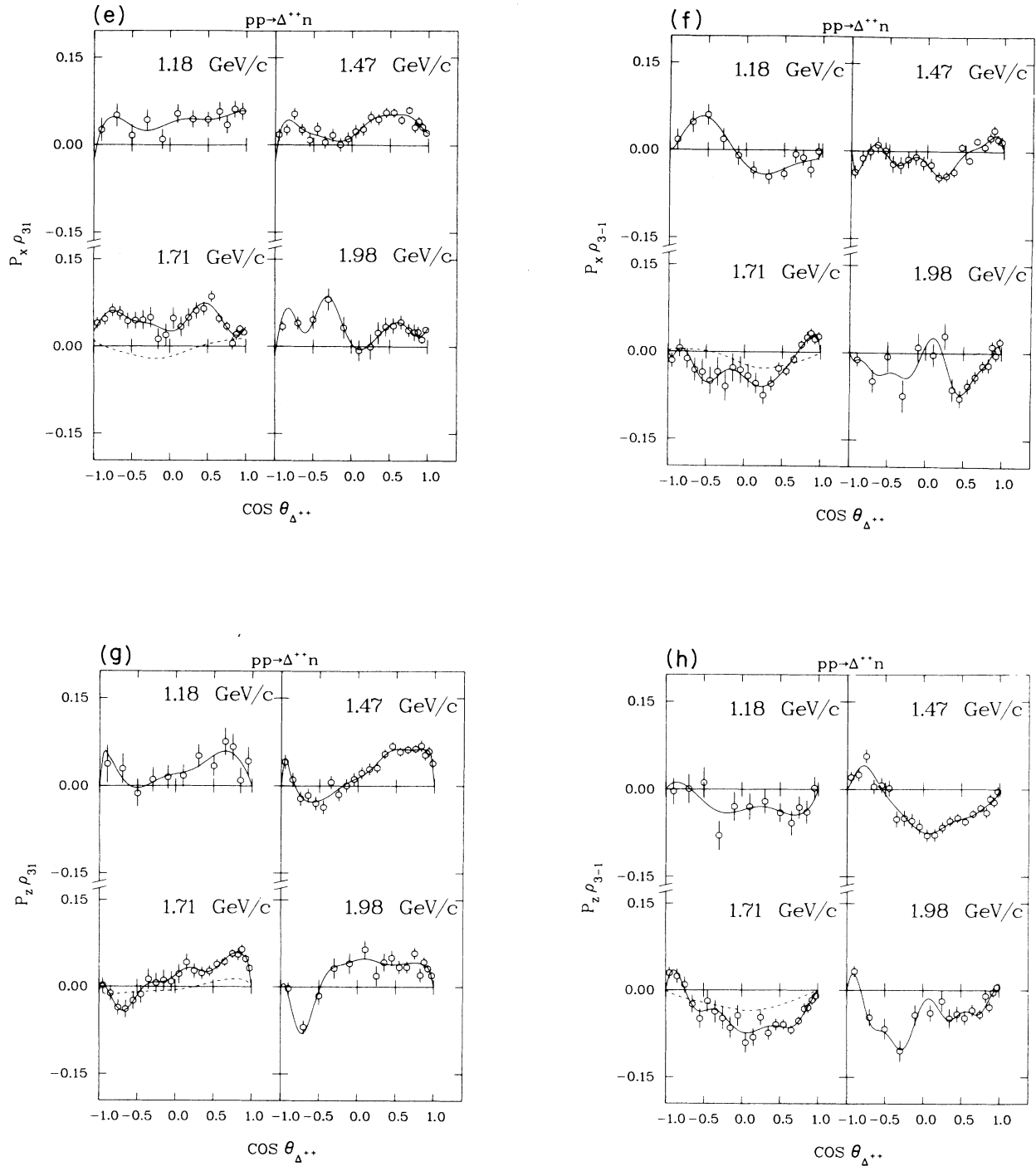


FIG. 11. (Continued).

A. Relationship between $p_1 p \rightarrow p \pi^+ n$ and $p_1 p \rightarrow \pi^+ d$

Deuteron formation presumably occurs through the $pn\pi^+$ intermediate state,²⁹ in kinematical configurations close to proton-neutron threshold. In terms of the Dalitz-plot variables, the condition $M_{pn} \approx 2m_N$ corresponds to the constraints

$$\cos\theta \approx -1, \quad (39a)$$

$$(M_{p\pi^+})^2 \approx \frac{s}{2} + \frac{m_\pi^2}{2} - m_N^2, \quad (39b)$$

where s is the total c.m. energy squared. Note that M_{pn} is independent of the kinematical variables Θ_Δ and ϕ . When

Eq. (39) is satisfied, the proton and neutron three-momenta are collinear and equal in magnitude, and the π^+ production angle is given by Θ_Δ . If deuteron production occurs through the $p\pi^+$ intermediate state, then substituting $\cos\theta = -1$ in the DME expansion of Eq. (21), we would expect

$$A_y(p_1 p \rightarrow \pi^+ d) = \frac{[P_y \rho_{11}(M_{p\pi^+}^0) - P_y \rho_{s1}(M_{p\pi^+}^0)]}{[\rho_{11}(M_{p\pi^+}^0) - \rho_{s1}(M_{p\pi^+}^0)]}, \quad (40)$$

where the RHS is evaluated at the mass $M_{p\pi^+}^0$ satisfying

Eq. (39b). The relevant values of $M_{p\pi^+}^0$ are 1.193, 1.283, 1.336, and 1.437 GeV at 1.18, 1.47, 1.71, and 1.98 GeV/c, respectively. The values at the two higher momenta are well above the Δ^{++} mass, where the cross section is small and our data are statistically limited. The values at 1.18 and 1.47 GeV/c occur within the Δ^{++} band, and we show the comparison between the two sides of Eq. (40) for these momenta in Fig. 16. The values for the $p_1 p \rightarrow p \pi^+ n$ spin correlations [the RHS of Eq. (40)] are taken from this experiment, averaged over the mass intervals $1.18 < M_{p\pi^+} < 1.20$ GeV for 1.18 GeV/c, and 1.26

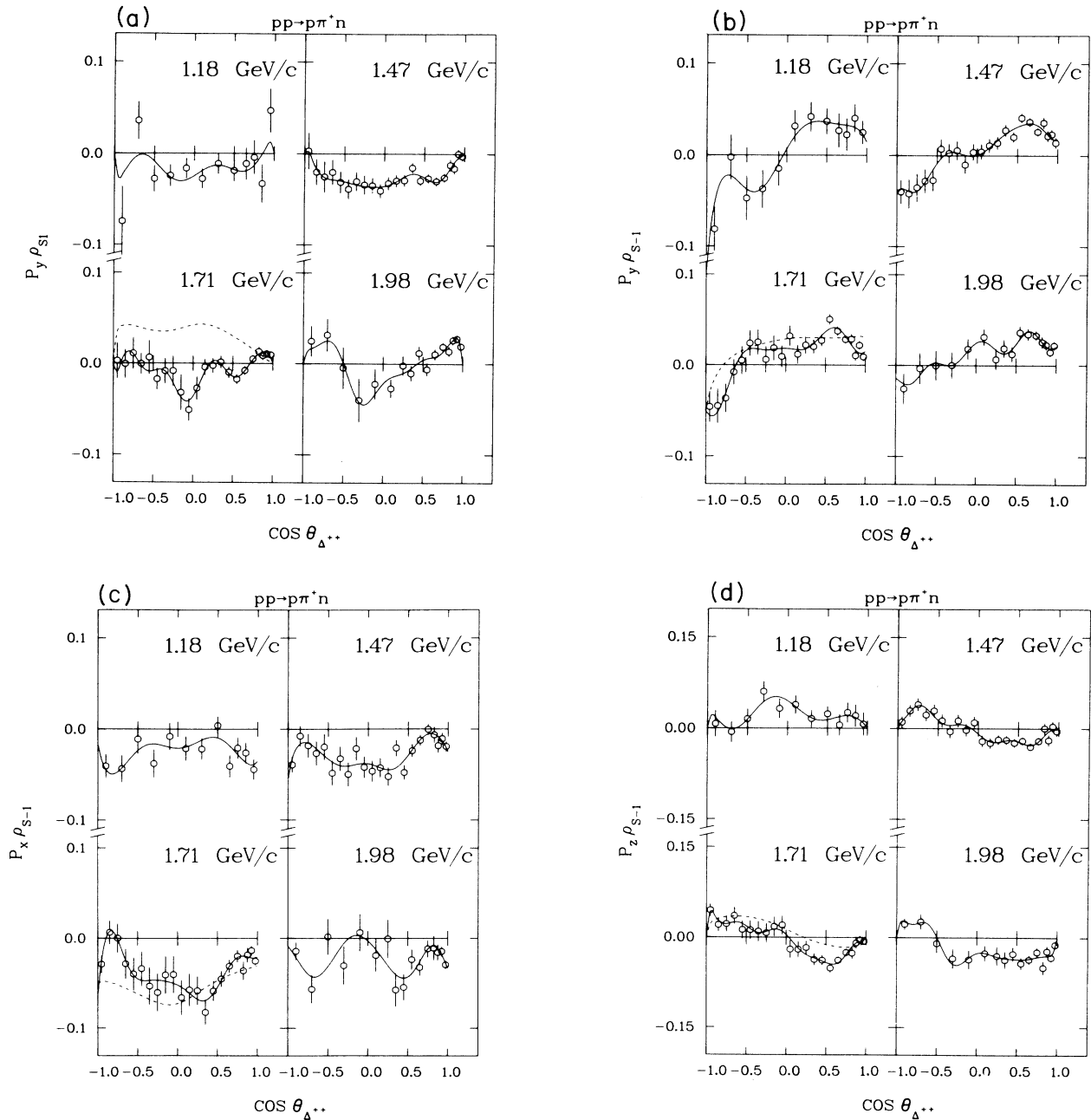


FIG. 12. s -channel spin correlations (a) $P_y \rho_{s1}$, (b) $P_y \rho_{s-1}$, (c) $P_x \rho_{s-1}$, and (d) $P_z \rho_{s-1}$ plotted against $\cos\Theta_\Delta$ (Δ^{++} -band cuts imposed). The curves are defined in Fig. 11.

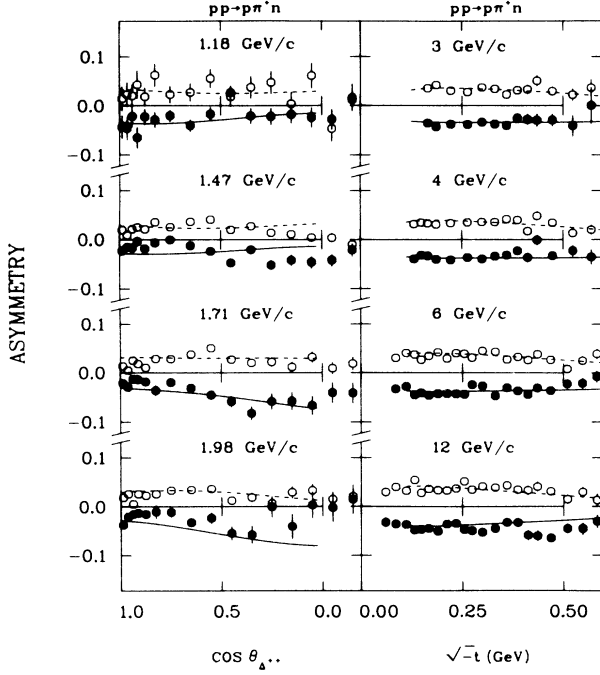


FIG. 13. s -channel spin correlations $P_y \rho_{s-1}$ (open points) and $P_x \rho_{s-1}$ (solid points) plotted against $\cos \Theta_{\Delta^+}$ (1.18 to 1.98 GeV/c) and $\sqrt{-t}$ (3 to 12 GeV/c) with Δ^{++} -band cuts as in Fig. 9. The curves indicate the pion-exchange predictions.

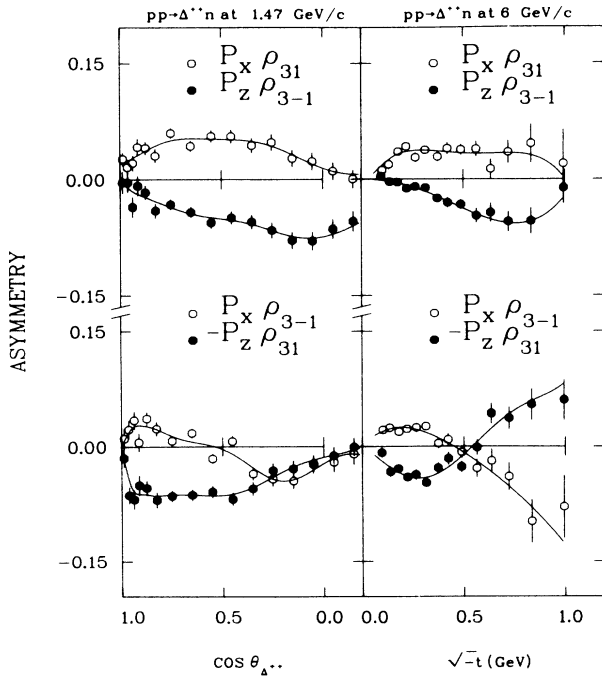


FIG. 14. s -channel spin correlations $P_{x,z} \rho_{31}$ and $P_{x,z} \rho_{3-1}$ compared at 1.47 and 6 GeV/c plotted against $\cos \Theta_{\Delta^+}$ and $\sqrt{-t}$, respectively (Δ^{++} -band cuts imposed). Pure unnatural-parity exchange would result in mirror symmetry for the pairs ($P_x \rho_{31}, P_z \rho_{3-1}$) and ($P_x \rho_{3-1}, -P_z \rho_{31}$) as explained in the text. The curves are the moments fits (1.47 GeV/c) and polynomial fits (6 GeV/c).

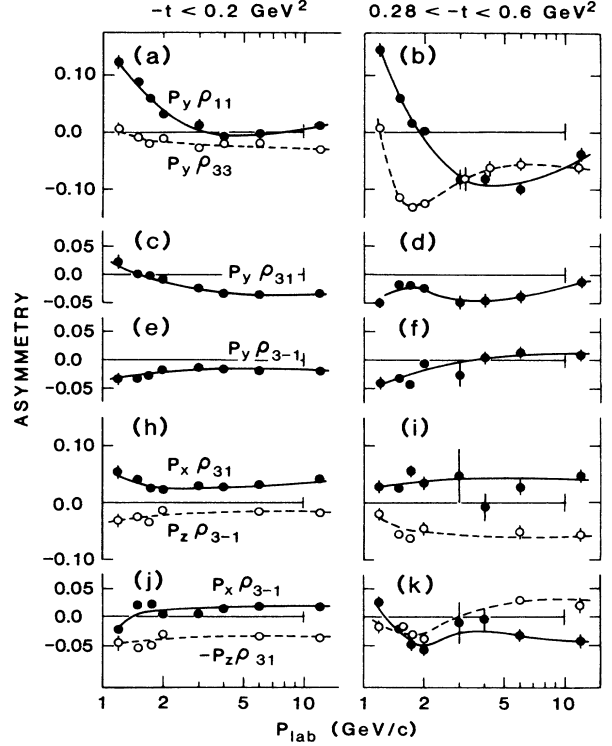


FIG. 15. Spin correlations $P_y \rho_{11}$, $P_y \rho_{33}$, $P_y \rho_{31}$, $P_y \rho_{3-1}$, $P_x \rho_{31}$, $P_x \rho_{3-1}$, $P_z \rho_{31}$, and $P_z \rho_{3-1}$, plotted against p_{lab} for the Δ^{++} band after averaging over the indicated momentum-transfer intervals $-t < 0.20 \text{ GeV}^2$ (a, c, e, h, j) and $0.28 < -t < 0.60 \text{ GeV}^2$ (b, d, f, i, k). The curves are to guide the eye.

$< M_{p\pi^+} < 1.30$ for 1.47 GeV/c; the dominant contributions to the RHS of Eq. (40) come from $P_y \rho_{11}$ and ρ_{11} . The $p_1 p \rightarrow \pi^+ d$ asymmetries [LHS of Eq. (40)] are taken from Refs. 38 and 44 and are shown as smooth curves in Fig. 16. The agreement is satisfactory.⁴⁵ In particular, the $pp \rightarrow \pi^+ d$ asymmetry is generally positive below 2 GeV/c and falls gradually with increasing p_{lab} , the same behavior that characterizes $P_y \rho_{11}$ in $p_1 p \rightarrow p\pi^+ n$. Note that $P_y \rho_{33}$, which is responsible for the rapid energy dependence and sign change in $A_y(p_1 p \rightarrow p\pi^+ n)$, does not enter into Eq. (40).

Strictly speaking, Eq. (40) is only an approximation, and the RHS should be calculated after projecting out those contributions to ρ_{11} and $P_y \rho_{11}$ which involve the spin-triplet final-state proton-neutron configuration. However, theoretical model calculations suggest that $pp \rightarrow p\pi^+ n$ is dominated by final states with $S = 1$ for the proton-neutron system.⁴⁶ In particular, if we require $l_{pn} = 0$ near proton-neutron threshold, then all of the even-parity waves (proton-proton initial states $^1S_0, ^1D_2, ^1G_4, ^1I_6, \dots$) can couple only to final states with $S_{pn} = 1$ due to parity conservation, and the same is true for all odd-parity waves which have odd J (proton-proton initial states $^3P_1, ^3F_3, ^3H_5, \dots$). The remaining odd-parity

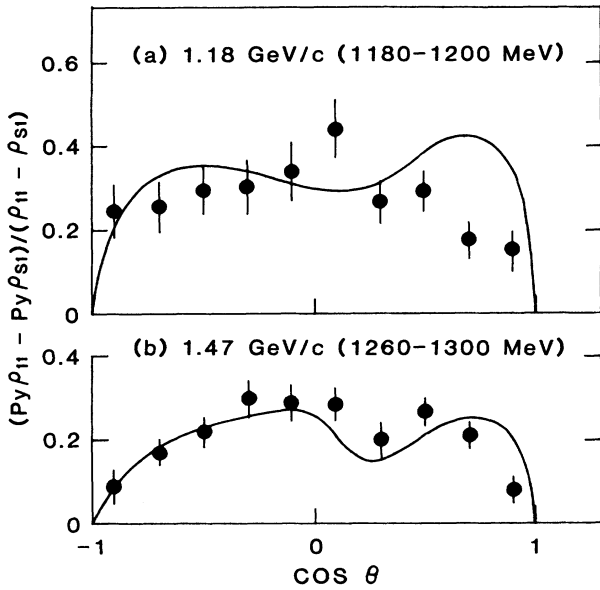


FIG. 16. Comparison of the helicity- $\frac{1}{2}$ projection of the $pp \rightarrow p\pi^+n$ asymmetry (solid points) and A_{n0} for $p_1 p \rightarrow \pi^+ d$ (solid curves) at 1.18 and 1.47 GeV/c. The angle variable is $\cos \Theta_\Delta$ for $p_1 p \rightarrow p\pi^+n$ and $\cos \Theta_\pi$ for $p_1 p \rightarrow \pi^+ d$. The $p_1 p \rightarrow p\pi^+n$ asymmetries have been extracted from the mass intervals $1.18 < M_{p\pi^+} < 1.20$ (1.18 GeV/c) and $1.26 < M_{p\pi^+} < 1.30$ GeV (1.47 GeV/c).

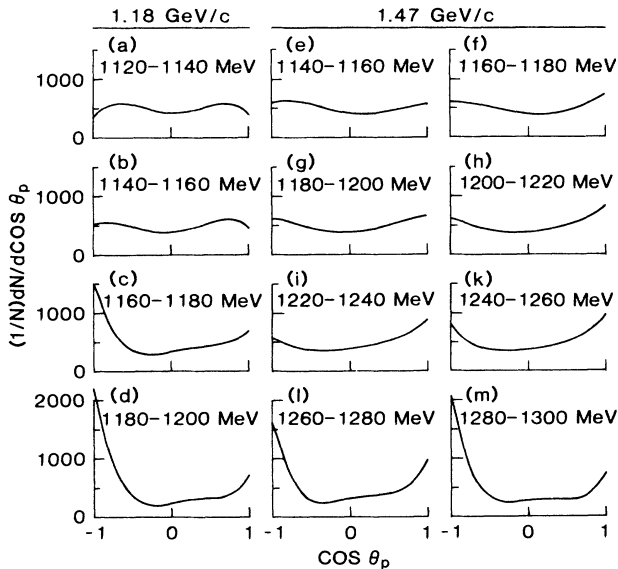


FIG. 17. Normalized angular distributions for $\cos \theta_p$, where θ_p is the s -channel polar decay angle describing $\Delta^{++} \rightarrow p\pi^+$. The distributions are reconstructed from the moments expansion of Eq. (10) and are sliced in 20 MeV mass intervals as indicated. The data are taken from the bin $0.8 < \cos \Theta_\Delta < 1.0$ at 1.18 and 1.47 GeV/c.

waves (${}^3P_{0,2}, {}^3F_{2,4}, {}^3H_{4,6}, \dots$) can *a priori* couple equally to $l_{pn}=0$ final states with $S_{pn}=0$ or $S_{pn}=1$ (3P_0 in particular can couple only to $S_{pn}=0$). Since $S_{pn}=0$ and 1 amplitudes do not interfere in observables averaged over final-state helicities, the $S_{pn}=0$ contributions are *a priori* small, given the expected sizes of the ${}^3P_{0,2}, {}^3P_{2,4}, \dots$ waves. (Of course, away from proton-neutron threshold, with $l_{pn} \neq 0$, these selection rules do not apply.) Thus, Eq. (40) should be a good approximation without explicit projection of the $S=1$ proton-neutron final states.

B. Final-state-interaction effects

In addition to deuteron production, the proton-neutron final-state interaction (FSI) is expected to enhance the $pp \rightarrow p\pi^+n$ cross sections near proton-neutron threshold. From Eq. (39) this should result in backward peaks in the projected $\cos \theta$ angular distributions for values of $M_{p\pi^+}$ close to $M_{p\pi^+}^0$ [e.g., 1.193 (1.283) GeV at 1.18 (1.47) GeV/c]. Figure 17 shows the $\cos \theta$ angular distributions from the moments fits in 20 MeV slices in $M_{p\pi^+}$ at 1.18 and 1.47 GeV/c; the expected backward peaks are prominent near $M_{p\pi^+} \sim M_{p\pi^+}^0$ at each momentum. These enhancements extend over a range in $M_{p\pi^+}$ and $\cos \theta$ which seems to be roughly consistent with the behavior of the 3S_1 proton-neutron phase shift, assuming an FSI enhancement proportional to $\sin^2 \delta({}^3S_1)$ (Ref. 47). Note that in Fig. 17 we have selected the production angle range $0.8 < \cos \Theta_\Delta < 1.0$ because this represents the worst case; for $|\cos \Theta_\Delta| < 0.5$, the backward peaks in $\cos \theta$ are relatively smaller by a factor of 2. This Θ_Δ dependence reflects the fact that the FSI enhancement should be proportional to the unenhanced $\cos \theta = -1$ production cross section; the latter is relatively larger near $\cos \Theta_\Delta = \pm 1$ because of the Θ_Δ dependence of ρ_{11} .

The FSI enhancements naturally result in nonzero $L=3,4$ moments near $M_{p\pi^+} \sim M_{p\pi^+}^0$ in the $\cos \theta$ expansion of Eq. (10). They also lead to a distortion in the $L=0,1,2$ moments in the same mass regions. Specifically, the FSI peak at $\cos \theta \sim -1$ naturally correlates with increased ρ_{11} , decreased ρ_{33} , and more negative ρ_{s1} in the $\cos \theta$ expansion fits. The other DME's, which vanish at $\cos \theta = -1$ and are associated with explicit ϕ dependence, should be less affected by the FSI enhancements. For $p_{\text{lab}} \geq 1.47$ GeV/c, these distortions in ρ_{11} , ρ_{33} , and ρ_{s1} do not pose serious difficulties for partial-wave fits because $M_{p\pi^+}^0$ occurs well on the high side of the Δ^{++} . However, at 1.18 GeV/c the distortions occur over a major part of the " Δ^{++} band" and are clearly reflected in the behavior of the DME's. For example, for $|\cos \Theta_\Delta| \geq 0.8$ we observe $\rho_{11} \sim 0.5$ and $\rho_{33} \sim 0$ [Figs. 10(a) and 10(b)]. It turns out that no physically plausible partial-wave expansion can yield such behavior at 1.18 GeV/c; instead we would expect ρ_{33} to go smoothly to zero at $\cos \Theta_\Delta = \pm 1$. We also observe a correlated negative enhancement in ρ_{s1} [Fig. 10(e)], and an apparent suppression of $P_y \rho_{33}$ [Fig. 11(b)], near $\cos \Theta_\Delta = \pm 1$. In principle, we could "correct" for the FSI distortions by increasing ρ_{33} and $P_y \rho_{33}$ appropriately, as functions of $\cos \Theta_\Delta$; alternatively, we could explicitly include the effects of the enhancement in partial-wave fits

TABLE V. Listing of normalized s -channel joint moments a_{MN}^L for each physical observable as measured in this experiment. The a_{MN}^L are defined as coefficients of $d_{MN}^L(\cos\Theta_\Delta)$ in the expansion of Eq. (23). We do not list the coefficient a_{00}^0 for $d\sigma/d\cos\Theta_\Delta$ ($a_{00}^0=1$ for $d\sigma/d\cos\Theta_\Delta$); instead we list the integrated cross section in mb, σ [cf. Eq. (23c)], under this column.

Unpolarized density-matrix elements						
$p_{\text{lab}}(\text{GeV}/c)$	σ (mb)	$(d\sigma/d\cos\Theta_\Delta)$				
		a_{00}^2	a_{00}^4	a_{00}^6	a_{00}^8	A_{00}^{10}
1.18	2.94±0.010	0.327±0.008	-0.066±0.010	-0.069±0.012		
1.47	10.81±0.018	0.870±0.004	0.068±0.006	-0.069±0.007	-0.049±0.008	-0.065±0.008
1.71	10.91±0.022	1.655±0.006	0.621±0.008	0.095±0.009	-0.041±0.010	-0.073±0.010
1.98	10.03±0.024	2.125±0.008	1.388±0.010	0.527±0.012	0.104±0.013	-0.029±0.012
(ρ_{11})						
	a_{00}^0	a_{00}^2	a_{00}^4	a_{00}^6	a_{00}^8	a_{00}^{10}
1.18	0.376±0.002	0.329±0.005	-0.086±0.007	-0.064±0.008		
1.47	0.278±0.001	0.427±0.003	0.048±0.003	-0.076±0.004	-0.039±0.005	-0.030±0.005
1.71	0.261±0.001	0.651±0.003	0.331±0.004	0.034±0.005	-0.062±0.005	-0.071±0.006
1.98	0.258±0.001	0.753±0.004	0.575±0.005	0.216±0.006	0.016±0.007	-0.077±0.007
(ρ_{33})						
	a_{00}^0	a_{00}^2	a_{00}^4	a_{00}^6	a_{00}^8	a_{00}^{10}
1.18	0.124±0.002	-0.166±0.004	0.053±0.006	0.033±0.007		
1.47	0.222±0.001	0.008±0.003	-0.013±0.003	0.041±0.004	0.015±0.005	-0.002±0.005
1.71	0.239±0.001	0.175±0.004	-0.020±0.005	0.010±0.006	0.040±0.006	0.030±0.006
1.98	0.243±0.002	0.308±0.005	0.122±0.006	0.041±0.007	0.034±0.008	0.046±0.007
(ρ_{31})						
	a_{01}^2	a_{01}^4	a_{01}^6	a_{01}^8	a_{01}^{10}	
1.18	0.316±0.005	-0.070±0.006	-0.065±0.007			
1.47	0.224±0.003	0.013±0.004	-0.088±0.004	-0.040±0.005	-0.005±0.005	
1.71	0.237±0.003	0.152±0.004	-0.049±0.005	-0.100±0.006	-0.048±0.006	
1.98	0.229±0.003	0.244±0.005	0.021±0.006	-0.089±0.007	-0.084±0.006	
(ρ_{3-1})						
	a_{02}^2	a_{02}^4	a_{02}^6	a_{02}^8	a_{02}^{10}	
1.18	-0.255±0.004	0.040±0.005	0.019±0.006			
1.47	-0.130±0.002	0.014±0.003	0.063±0.004	0.026±0.004	-0.003±0.004	
1.71	-0.071±0.002	-0.031±0.003	0.072±0.005	0.071±0.005	0.034±0.005	
1.98	-0.046±0.002	-0.060±0.004	0.045±0.006	0.061±0.006	0.035±0.006	
(ρ_{51})						
	a_{00}^0	a_{00}^2	a_{00}^4	a_{00}^6	a_{00}^8	a_{00}^{10}
1.18	-0.109±0.002	-0.055±0.004	0.056±0.005	0.042±0.006		
1.47	0.015±0.001	0.069±0.002	0.041±0.002	0.022±0.003	0.019±0.003	-0.006±0.004
1.71	0.042±0.001	0.108±0.002	0.072±0.003	0.028±0.004	-0.014±0.004	-0.022±0.004
1.98	0.040±0.001	0.090±0.003	0.074±0.004	0.011±0.005	-0.027±0.005	-0.039±0.005
(ρ_{5-1})						
	a_{01}^2	a_{01}^4	a_{01}^6	a_{01}^8	a_{01}^{10}	
1.18	0.048±0.003	0.001±0.004	-0.035±0.005			
1.47	-0.055±0.002	0.010±0.003	0.027±0.003	-0.002±0.003	-0.015±0.004	
1.71	-0.098±0.002	0.007±0.003	0.065±0.004	0.038±0.004	0.004±0.004	
1.98	-0.103±0.002	-0.057±0.004	0.063±0.005	0.066±0.005	0.026±0.005	
Singlet-triplet asymmetries						
(A_y)						
	a_{10}^1	a_{10}^3	a_{10}^5	a_{10}^7	a_{10}^9	
1.18	-0.544±0.024	-0.200±0.053	0.030±0.061			
1.47	0.016±0.009	-0.271±0.023	-0.144±0.031	-0.014±0.035	-0.001±0.030	
1.71	0.151±0.010	-0.119±0.029	-0.163±0.043	-0.088±0.047	-0.016±0.036	
1.98	0.161±0.013	-0.012±0.039	-0.137±0.060	-0.126±0.067	-0.100±0.047	

TABLE V. (Continued).

P_{lab} (GeV/c)	Singlet-triplet asymmetries				
	a_{10}^1	a_{10}^3	a_{10}^5	a_{10}^7	a_{10}^9
1.18	-0.221 ± 0.009	-0.201 ± 0.022	-0.030 ± 0.023		
1.47	-0.104 ± 0.004	-0.123 ± 0.010	-0.034 ± 0.014	0.007 ± 0.017	0.017 ± 0.014
1.71	-0.042 ± 0.004	-0.103 ± 0.013	-0.053 ± 0.019	0.003 ± 0.021	0.029 ± 0.016
1.98	-0.009 ± 0.006	-0.050 ± 0.016	-0.032 ± 0.025	0.006 ± 0.028	0.003 ± 0.020
	$(P_y \rho_{11})$				
	a_{10}^1	a_{10}^3	a_{10}^5	a_{10}^7	a_{10}^9
1.18	-0.054 ± 0.011	0.087 ± 0.019	0.022 ± 0.024		
1.47	0.112 ± 0.004	-0.012 ± 0.009	-0.036 ± 0.012	-0.010 ± 0.014	-0.011 ± 0.013
1.71	0.117 ± 0.004	0.043 ± 0.012	-0.033 ± 0.017	-0.047 ± 0.018	-0.035 ± 0.015
1.98	0.093 ± 0.005	0.059 ± 0.015	-0.012 ± 0.023	-0.050 ± 0.025	-0.044 ± 0.018
	$(P_y \rho_{31})$				
	a_{00}^1	a_{00}^3	a_{00}^5	a_{00}^7	a_{00}^9
1.18	0.036 ± 0.014	-0.142 ± 0.018	-0.068 ± 0.021		
1.47	-0.023 ± 0.006	-0.021 ± 0.008	-0.008 ± 0.009	0.005 ± 0.011	0.006 ± 0.009
1.71	-0.035 ± 0.009	-0.025 ± 0.014	-0.026 ± 0.015	-0.021 ± 0.016	-0.021 ± 0.011
1.98	-0.028 ± 0.013	-0.010 ± 0.023	0.018 ± 0.024	0.017 ± 0.021	0.008 ± 0.012
	$(P_y \rho_{3-1})$				
	a_{01}^1	a_{01}^3	a_{01}^5	a_{01}^7	a_{01}^9
1.18	-0.090 ± 0.010	0.014 ± 0.017	0.007 ± 0.020		
1.47	-0.044 ± 0.004	-0.042 ± 0.009	-0.022 ± 0.011	-0.005 ± 0.012	-0.003 ± 0.012
1.71	-0.039 ± 0.004	-0.057 ± 0.011	-0.015 ± 0.015	-0.009 ± 0.017	-0.005 ± 0.014
1.98	-0.034 ± 0.005	-0.055 ± 0.015	-0.062 ± 0.021	-0.048 ± 0.023	-0.011 ± 0.017
	$(P_x \rho_{31})$				
	a_{00}^0	a_{00}^2	a_{00}^4	a_{00}^6	a_{00}^8
1.18	0.040 ± 0.005	0.016 ± 0.013	-0.017 ± 0.017	-0.019 ± 0.019	
1.47	0.032 ± 0.002	0.029 ± 0.006	-0.031 ± 0.007	-0.023 ± 0.009	-0.015 ± 0.010
1.71	0.042 ± 0.003	0.054 ± 0.008	-0.008 ± 0.010	0.007 ± 0.012	0.001 ± 0.012
1.98	0.032 ± 0.003	0.056 ± 0.012	0.006 ± 0.015	-0.018 ± 0.017	-0.035 ± 0.015
	$(P_x \rho_{3-1})$				
	a_{01}^2	a_{01}^4	a_{01}^6	a_{01}^8	a_{01}^{10}
1.18	-0.066 ± 0.011	0.021 ± 0.015	0.004 ± 0.017		
1.47	0.018 ± 0.006	0.045 ± 0.009	0.028 ± 0.010	0.021 ± 0.012	-0.020 ± 0.011
1.71	0.020 ± 0.008	0.035 ± 0.013	0.022 ± 0.016	0.032 ± 0.018	0.008 ± 0.015
1.98	0.005 ± 0.011	0.022 ± 0.018	0.036 ± 0.022	0.014 ± 0.024	0.030 ± 0.019
	$(P_z \rho_{31})$				
	a_{01}^2	a_{01}^4	a_{01}^6	a_{01}^8	a_{01}^{10}
1.18	0.029 ± 0.017	-0.029 ± 0.024	-0.031 ± 0.026		
1.47	0.070 ± 0.006	0.000 ± 0.009	-0.024 ± 0.010	-0.009 ± 0.012	-0.008 ± 0.011
1.71	0.070 ± 0.007	0.058 ± 0.012	0.002 ± 0.014	-0.011 ± 0.015	0.008 ± 0.012
1.98	0.068 ± 0.008	0.062 ± 0.015	-0.009 ± 0.019	-0.026 ± 0.019	-0.003 ± 0.015
	$(P_z \rho_{3-1})$				
	a_{02}^2	a_{02}^4	a_{02}^6	a_{02}^8	a_{02}^{10}
1.18	-0.056 ± 0.015	-0.011 ± 0.021	0.000 ± 0.024		
1.47	-0.058 ± 0.004	0.027 ± 0.008	0.008 ± 0.010	-0.001 ± 0.011	-0.011 ± 0.011
1.71	-0.055 ± 0.004	-0.022 ± 0.009	0.023 ± 0.013	0.040 ± 0.015	0.006 ± 0.013
1.98	-0.047 ± 0.005	-0.028 ± 0.011	0.035 ± 0.016	0.042 ± 0.019	0.042 ± 0.015
	$(P_y \rho_{51})$				
	a_{10}^1	a_{10}^3	a_{10}^5	a_{10}^7	a_{10}^9
1.18	0.025 ± 0.008	-0.002 ± 0.019	0.006 ± 0.020		
1.47	0.038 ± 0.003	0.015 ± 0.009	-0.010 ± 0.012	-0.017 ± 0.014	-0.001 ± 0.011
1.71	0.005 ± 0.004	-0.018 ± 0.011	-0.009 ± 0.016	0.005 ± 0.018	0.025 ± 0.014
1.98	-0.007 ± 0.005	-0.057 ± 0.014	-0.044 ± 0.021	-0.025 ± 0.024	-0.018 ± 0.017

TABLE V. (Continued).

Singlet-triplet asymmetries					
p_{lab} (GeV/c)	$(P_y \rho_s - 1)$				
	a_{00}^1	a_{00}^3	a_{00}^5	a_{00}^7	a_{00}^9
1.18	0.060±0.012	-0.006±0.015	0.032±0.020		
1.47	0.051±0.006	0.012±0.007	-0.016±0.008	0.001±0.010	0.006±0.009
1.71	0.061±0.008	0.052±0.012	0.002±0.013	-0.007±0.014	-0.001±0.010
1.98	0.042±0.013	0.034±0.022	0.007±0.023	-0.001±0.021	0.005±0.012
$(P_x \rho_s - 1)$					
	a_{00}^0	a_{00}^2	a_{00}^4	a_{00}^6	a_{00}^8
1.18	-0.026±0.004	-0.029±0.009	0.002±0.012	0.022±0.014	
1.47	-0.025±0.002	-0.004±0.006	-0.020±0.007	-0.023±0.009	0.001±0.010
1.71	-0.028±0.003	-0.017±0.008	-0.027±0.010	-0.050±0.013	-0.020±0.013
1.98	-0.022±0.004	-0.044±0.012	-0.012±0.015	-0.020±0.018	-0.009±0.016
$(P_z \rho_s - 1)$					
	a_{01}^2	a_{01}^4	a_{01}^6	a_{01}^8	a_{01}^{10}
1.18	0.002±0.012	0.011±0.017	-0.026±0.019		
1.47	-0.043±0.005	-0.010±0.007	0.012±0.009	0.011±0.010	-0.013±0.009
1.71	-0.056±0.006	-0.036±0.010	-0.024±0.012	-0.026±0.013	-0.020±0.011
1.98	-0.050±0.008	-0.068±0.014	-0.038±0.017	-0.033±0.018	-0.015±0.013
Triplet-triplet asymmetries					
(A_y)					
	a_{10}^2	a_{10}^4	a_{10}^6	a_{10}^8	a_{10}^{10}
1.18	0.012±0.041	0.005±0.060	-0.049±0.059		
1.47	-0.094±0.017	-0.050±0.027	-0.019±0.033	-0.021±0.035	0.003±0.026
1.71	-0.095±0.020	-0.134±0.037	-0.081±0.047	-0.039±0.047	-0.023±0.030
1.98	-0.055±0.026	-0.140±0.051	-0.142±0.067	-0.073±0.065	-0.020±0.037
$(P_y \rho_{11})$					
	a_{10}^2	a_{10}^4	a_{10}^6	a_{10}^8	a_{10}^{10}
1.18	0.051±0.016	0.035±0.026	0.000±0.024		
1.47	-0.019±0.007	-0.028±0.012	-0.028±0.016	-0.015±0.016	-0.003±0.011
1.71	-0.014±0.009	-0.052±0.016	-0.070±0.020	-0.042±0.021	-0.023±0.012
1.98	-0.017±0.011	-0.039±0.021	-0.089±0.028	-0.052±0.027	-0.008±0.015
$(P_y \rho_{33})$					
	a_{10}^2	a_{10}^4	a_{10}^6	a_{10}^8	a_{10}^{10}
1.18	-0.038±0.016	-0.015±0.022	-0.017±0.024		
1.47	-0.029±0.007	0.001±0.011	0.014±0.013	-0.004±0.014	-0.001±0.013
1.71	-0.034±0.008	-0.013±0.015	0.032±0.018	0.021±0.019	0.010±0.014
1.98	-0.020±0.010	-0.055±0.020	-0.014±0.025	-0.011±0.025	-0.019±0.016
$(P_y \rho_{31})$					
	a_{00}^0	a_{00}^2	a_{00}^4	a_{00}^6	a_{00}^8
1.18	-0.013±0.006	0.034±0.016	0.024±0.020	0.021±0.022	
1.47	0.003±0.003	0.029±0.007	-0.027±0.008	-0.034±0.011	-0.010±0.010
1.71	0.008±0.003	0.032±0.012	0.015±0.014	-0.017±0.015	-0.010±0.012
1.98	-0.001±0.005	0.002±0.019	-0.003±0.024	-0.029±0.023	-0.022±0.015
$(P_y \rho_{3-1})$					
	a_{01}^2	a_{01}^4	a_{01}^6	a_{01}^8	a_{01}^{10}
1.18	-0.006±0.014	0.025±0.019	-0.016±0.021		
1.47	-0.016±0.007	-0.003±0.010	0.021±0.011	0.010±0.013	0.003±0.012
1.71	-0.014±0.008	-0.001±0.014	-0.012±0.016	-0.019±0.017	-0.007±0.013
1.98	0.033±0.010	0.010±0.019	0.003±0.023	-0.011±0.023	-0.008±0.015
$(P_x \rho_{31})$					
	a_{00}^1	a_{00}^3	a_{00}^5	a_{00}^7	a_{00}^9
1.18	0.017±0.010	0.011±0.015	0.023±0.018		
1.47	0.015±0.005	-0.012±0.007	0.017±0.008	0.014±0.010	0.010±0.010
1.71	-0.014±0.006	-0.019±0.009	0.021±0.011	0.027±0.013	0.000±0.011
1.98	-0.012±0.008	0.012±0.014	0.024±0.016	0.070±0.017	0.030±0.014

TABLE V. (Continued).

p_{lab} (GeV/c)	Triplet-triplet asymmetries				
	$(P_x \rho_{3-1})$				
	a_{01}^1	a_{01}^3	a_{01}^5	a_{01}^7	a_{01}^9
1.18	-0.002 ± 0.008	0.024 ± 0.014	-0.029 ± 0.017		
1.47	-0.013 ± 0.004	0.019 ± 0.008	-0.012 ± 0.010	-0.022 ± 0.011	0.007 ± 0.011
1.71	-0.023 ± 0.005	0.029 ± 0.011	0.043 ± 0.014	-0.005 ± 0.016	-0.014 ± 0.015
1.98	-0.025 ± 0.006	-0.026 ± 0.015	0.025 ± 0.021	0.001 ± 0.023	0.009 ± 0.020
	$(P_z \rho_{31})$				
	a_{01}^1	a_{01}^3	a_{01}^5	a_{01}^7	a_{01}^9
1.18	0.043 ± 0.011	0.049 ± 0.021	0.022 ± 0.025		
1.47	0.033 ± 0.003	0.058 ± 0.008	0.053 ± 0.010	0.038 ± 0.011	0.011 ± 0.011
1.71	0.019 ± 0.004	0.036 ± 0.010	0.052 ± 0.013	0.033 ± 0.015	0.005 ± 0.013
1.98	0.014 ± 0.004	-0.005 ± 0.012	0.041 ± 0.017	0.057 ± 0.019	0.024 ± 0.016
	$(P_z \rho_{3-1})$				
	a_{02}^3	a_{02}^5	a_{02}^7	a_{02}^9	
1.18	-0.028 ± 0.018	-0.040 ± 0.023			
1.47	-0.059 ± 0.006	-0.049 ± 0.009	-0.010 ± 0.010	0.006 ± 0.011	
1.71	-0.046 ± 0.007	-0.059 ± 0.011	-0.048 ± 0.014	-0.016 ± 0.013	
1.98	0.004 ± 0.008	-0.044 ± 0.014	-0.041 ± 0.018	-0.031 ± 0.016	
	$(P_y \rho_{s1})$				
	a_{10}^2	a_{10}^4	a_{10}^6	a_{10}^8	a_{10}^{10}
1.18	-0.002 ± 0.014	-0.011 ± 0.022	-0.030 ± 0.020		
1.47	-0.002 ± 0.006	0.004 ± 0.010	-0.002 ± 0.013	0.006 ± 0.013	0.007 ± 0.009
1.71	-0.003 ± 0.007	-0.008 ± 0.014	-0.025 ± 0.017	-0.012 ± 0.018	-0.013 ± 0.010
1.98	-0.004 ± 0.010	-0.005 ± 0.018	-0.027 ± 0.024	-0.008 ± 0.023	0.000 ± 0.013
	$(P_y \rho_{s-1})$				
	a_{00}^0	a_{00}^2	a_{00}^4	a_{00}^6	a_{00}^8
1.18	-0.002 ± 0.006	-0.019 ± 0.014	-0.024 ± 0.018	-0.024 ± 0.020	
1.47	0.001 ± 0.002	-0.016 ± 0.007	-0.012 ± 0.007	0.010 ± 0.009	-0.004 ± 0.010
1.71	-0.001 ± 0.003	-0.041 ± 0.011	-0.041 ± 0.012	0.008 ± 0.014	0.017 ± 0.012
1.98	0.006 ± 0.005	0.000 ± 0.018	-0.004 ± 0.023	0.001 ± 0.022	0.014 ± 0.015
	$(P_x \rho_{s-1})$				
	a_{00}^1	a_{00}^3	a_{00}^5	a_{00}^7	a_{00}^9
1.18	0.008 ± 0.007	-0.008 ± 0.011	-0.011 ± 0.014		
1.47	0.009 ± 0.005	0.008 ± 0.006	0.001 ± 0.008	0.006 ± 0.010	0.002 ± 0.010
1.71	-0.009 ± 0.007	0.009 ± 0.009	0.023 ± 0.011	0.034 ± 0.013	0.016 ± 0.012
1.98	0.001 ± 0.009	-0.006 ± 0.014	-0.035 ± 0.017	-0.019 ± 0.018	-0.005 ± 0.014
	$(P_z \rho_{s-1})$				
	a_{01}^1	a_{01}^3	a_{01}^5	a_{01}^7	a_{01}^9
1.18	0.037 ± 0.008	-0.007 ± 0.015	0.024 ± 0.018		
1.47	-0.001 ± 0.003	0.018 ± 0.006	0.008 ± 0.008	-0.005 ± 0.009	-0.004 ± 0.009
1.71	-0.002 ± 0.003	0.018 ± 0.008	0.043 ± 0.011	0.026 ± 0.013	0.015 ± 0.011
1.98	-0.015 ± 0.004	0.004 ± 0.011	0.001 ± 0.015	-0.001 ± 0.017	0.011 ± 0.014

to the raw data. We have done neither, but have instead allowed for larger systematic errors on ρ_{33} and $P_y \rho_{33}$ at 1.18 GeV/c.

VI. FEATURES OF THE JOINT MOMENTS

In this section we survey the behavior of the joint moments averaged over the Δ^{++} band, in particular for the

DME's and SSC's that arise from Δ - Δ interference. Recall that the moments $a_{MN}^L(P_i \rho_{jk})$ are defined as the coefficients of $d_{MN}^L(\cos\Theta_\Delta)$ in the expansion of $d\sigma/d\cos\Theta_\Delta P_i \rho_{jk}$ [Eq. (23a)]; recall also that we have normalized the moments at each energy so that $a_{00}^0 = 1$ in the expansion of $d\sigma/d\cos\Theta_\Delta$ [Eq. (23b)]. Table V provides a numerical listing of the fitted moments for all DME's and SSC's.

A. Unpolarized moments

Figure 18(a) shows the integrated cross sections σ [Eq. (23c)], which provide the overall normalization at each energy. For comparison, we also show the results of Shimizu *et al.*³ corrected for the cut on the Δ^{++} band.⁴⁸ Figures 18(b)–18(f) show the joint moments a_{00}^L in the expansion of $d\sigma/d\cos\Theta_\Delta$, together with the corresponding coefficients from Ref. 3. Shimizu *et al.* reported Legendre coefficients of order $L \leq 6$, and so no comparison is made for a_{00}^8 and a_{00}^{10} ; also, we fixed $a_{00}^8=0$ and $a_{00}^{10}=0$ in the 1.18-GeV/ c fits, as indicated in Figs. 18(e) and (f). Overall the agreement with Shimizu *et al.* seems satisfactory; we remark also that the t -channel DME's presented in Ref. 3 are consistent with our data in Fig. 9.

The leading moments for the unpolarized DME's ρ_{11} , ρ_{33} , ρ_{31} , and ρ_{3-1} are shown in Fig. 19, together with curves based on partial-wave fits as described in the next section. Since the unpolarized DME's do not include singlet-triplet interference terms (cf. Table II), they are generally more sensitive to the partial-wave intensities than to relative phase behavior. The gross features of the moments, for example, the relative signs of the ρ_{31} and ρ_{3-1} terms, are indicative of large 1D_2 and 3F_3 cross sec-

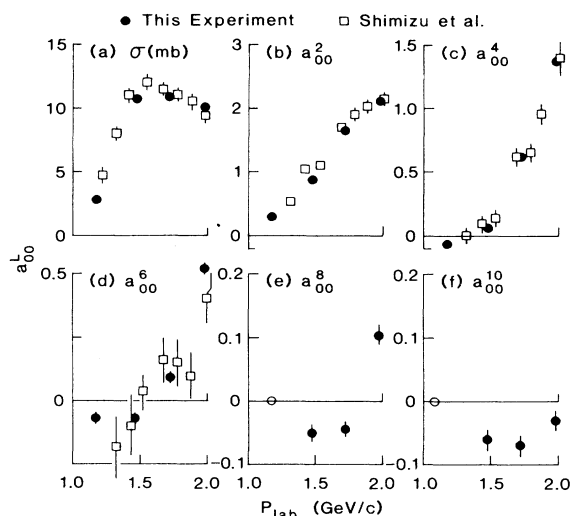


FIG. 18. Integrated cross sections (a) and angular distribution moments (b)–(f) for $d\sigma/d\cos\Theta_\Delta$ plotted against p_{lab} (Δ^{++} -band cuts imposed). The solid (open) points are from this experiment (Ref. 3).

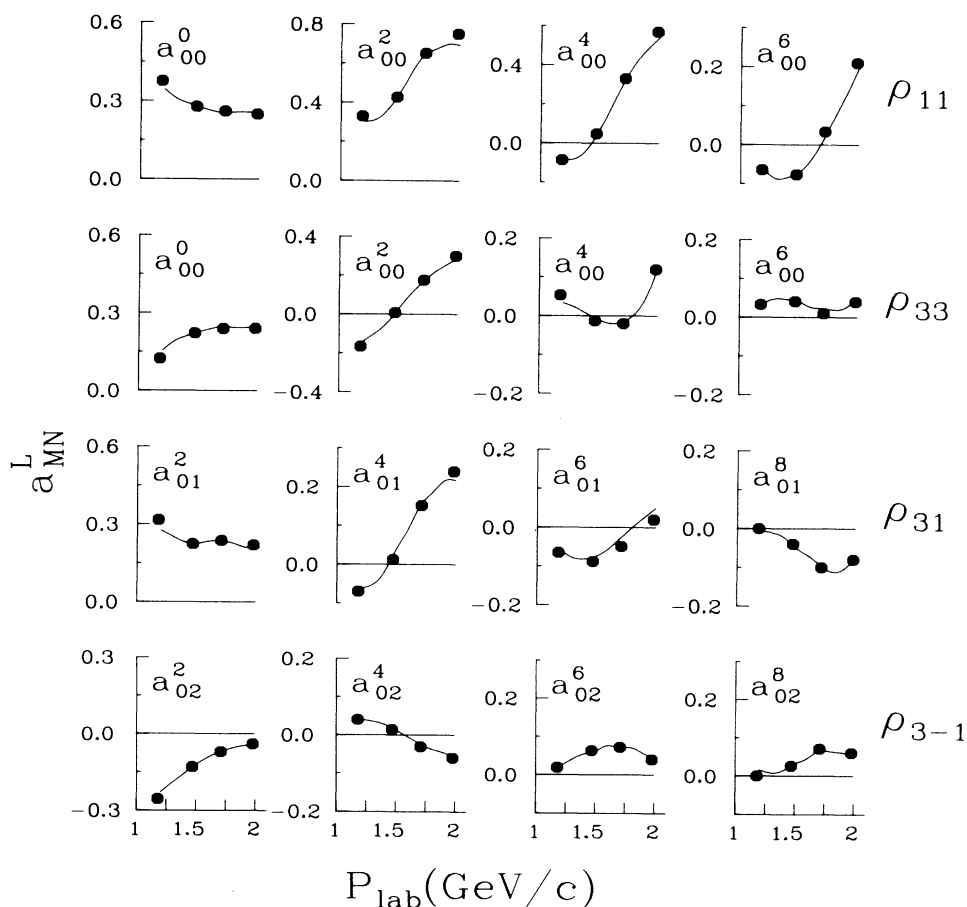


FIG. 19. Joint moments for the unpolarized DME's ρ_{11} , ρ_{33} , ρ_{31} , and ρ_{3-1} plotted against p_{lab} . The curves are results of partial-wave fits ("OPE" solution).

tions, as can be read off from Table III. Of course, our pion-exchange model reproduces these features by construction, and requires partial-wave intensities more or less as predicted by the elastic PSA.

B. Spin-correlation moments

Figures 20–23 show the joint moments for the Δ - Δ interference SSC's; we have displayed separately the singlet-triplet (Figs. 20 and 22) and triplet-triplet (Figs. 21 and 23) contributions. The curves are results of partial-wave fits described in Sec. VII. We also show the joint moments for $p, p \rightarrow \pi^+d$ together with $a_{10}^L(P_y\rho_{11})$ in Figs. 20 and 21; these were obtained from Eq. (49), ignoring the ρ_{s1} contributions, using the relations

$$a_{10}^L(pp \rightarrow \pi^+d) = -\sqrt{L(L+1)}a_{00}^0(\rho_{11}) \left(\frac{b_L}{a_0} \right)_{pp \rightarrow \pi^+d}. \quad (41)$$

Here a_0 and b_L on the RHS are Legendre and associated Legendre coefficients for $pp \rightarrow \pi^+d$ from Ref. 44, and

$a_{00}^0(\rho_{11})$ are the moments for $pp \rightarrow p\pi^+n$ shown in Fig. 19. As anticipated in Sec. VA, the large singlet-triplet moments are reasonably consistent for $pp \rightarrow p\pi^+n$ and $pp \rightarrow \pi^+d$ (Fig. 20); the smaller triplet-triplet terms are not in good agreement at the lower momenta (Fig. 21).

The rapid p_{lab} dependence noted earlier in A_y and $P_y\rho_{33}$ is evident in the singlet-triplet coefficients of Fig. 20; while the $a_{10}^L(P_y\rho_{11})$ vary smoothly with p_{lab} , $a_{10}^1(A_y)$ and $a_{10}^1(P_y\rho_{33})$ change sign above 1.2 GeV/c, and $a_{10}^3(A_y)$ and $a_{10}^3(P_y\rho_{33})$ develop minima at 1.5 GeV/c. The singlet-triplet moments for $P_i\rho_{31}$ and $P_i\rho_{3-1}$ show some energy-dependent structures (Fig. 22). The triplet-triplet moments of Figs. 21 and 23 are generally small. All moments show reasonable continuity as functions of p_{lab} .

As noted in Sec. IV C, the rapid p_{lab} dependence of the singlet-triplet moments in Fig. 20 cannot be explained by the interference of only two waves, because of the disparate behavior of $P_y\rho_{11}$ and $P_y\rho_{33}$. Suppose, for example, that the singlet-triplet moments were dominated by 1D_2 - 3F_3 interference. Then from Table III, the mo-

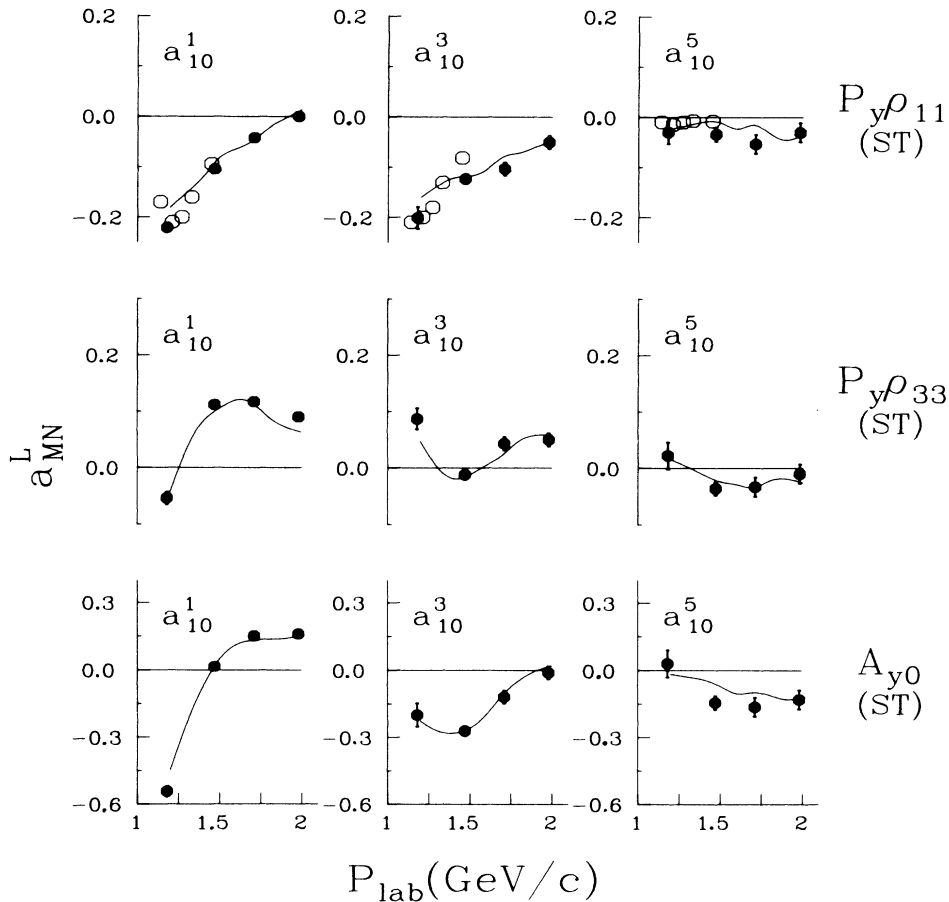


FIG. 20. Singlet-triplet interference moments ($L=1, 3$, and 5) for $P_y\rho_{11}$, $P_y\rho_{33}$, and A_y plotted against p_{lab} (Δ^{++} -band cuts imposed). The curves are results of partial-wave fits ("OPE" solution). The open boxes for $P_y\rho_{11}$ indicate the corresponding moments for $p, p \rightarrow \pi^+d$ using Eq. (41).

ments for $P_y\rho_{11}$ and $P_y\rho_{33}$ would take the form

$$a_{10}^1(P_y\rho_{11}) = \frac{3}{2}a_{10}^1(P_y\rho_{33}) = 0.66 \text{Im}({}^1D_2^{-3}F_3^*), \quad (42a)$$

$$a_{10}^3(P_y\rho_{11}) = -a_{10}^3(P_y\rho_{33}) = 0.40 \text{Im}({}^1D_2^{-3}F_3^*). \quad (42b)$$

The first relation (42a), requiring like signs for $a_{10}^1(P_y\rho_{11})$ and $a_{10}^1(P_y\rho_{33})$, may be satisfied at threshold, but is strongly broken by the sign change in $a_{10}^1(P_y\rho_{33})$ above 1.18 GeV/c; the second relation (42b) is satisfied in sign but clearly not in magnitude nor in p_{lab} dependence. Thus, it is clear that ${}^1D_2^{-3}F_3$ interference alone cannot account for the spin correlations.

Consider next a more complicated picture in which all of the moments have a smooth p_{lab} dependence given by various “background” contributions, together with some specific structure near threshold due to enhanced ${}^1D_2^{-3}F_3$ interference. Assuming $\text{Im}({}^1D_2^{-3}F_3^*) < 0$ for concreteness, we would then expect negative threshold enhancements in the moments $a_{10}^1(P_y\rho_{11})$, $a_{10}^3(P_y\rho_{11})$, $a_{10}^1(P_y\rho_{33})$, $a_{00}^3(P_y\rho_{31})$, $a_{01}^1(P_y\rho_{3-1})$, and $a_{01}^2(P_x\rho_{3-1})$; likewise, we would expect positive enhancements in $a_{10}^3(P_y\rho_{33})$,

$a_{00}^1(P_y\rho_{31})$, $a_{01}^3(P_y\rho_{3-1})$, and $a_{00}^0(P_x\rho_{31})$. Except for $a_{00}^0(P_x\rho_{31})$ in Fig. 22, this pattern seems qualitatively to match the data. Note that (cf. Table III) there are no ${}^1D_2^{-3}F_3$ contributions to $P_z\rho_{31}$ or $P_z\rho_{3-1}$.

Thus, we conclude that the p_{lab} dependence of the SSC's suggests a threshold enhancement in $\text{Im}({}^1D_2^{-3}F_3^*)$, supplemented by additional contributions from other partial-wave interferences. Given the apparent complexity of the DME's and SSC's, further progress requires a more general amplitude analysis as described in the next section.

VII. PARTIAL-WAVE ANALYSIS

This section summarizes our partial-wave fits to the joint moments. We also compare the partial waves for the free ($pp \rightarrow p\pi^+n$) reaction with those from similar analysis of the bound ($pp \rightarrow \pi^+d$) reaction. In our partial-wave analysis (PWA) we explored several ways of incorporating constraints on the partial-wave structure from the elastic PSA and the pion-exchange model, all of which led to generally similar solutions; we present representative results from the different fitting strategies.

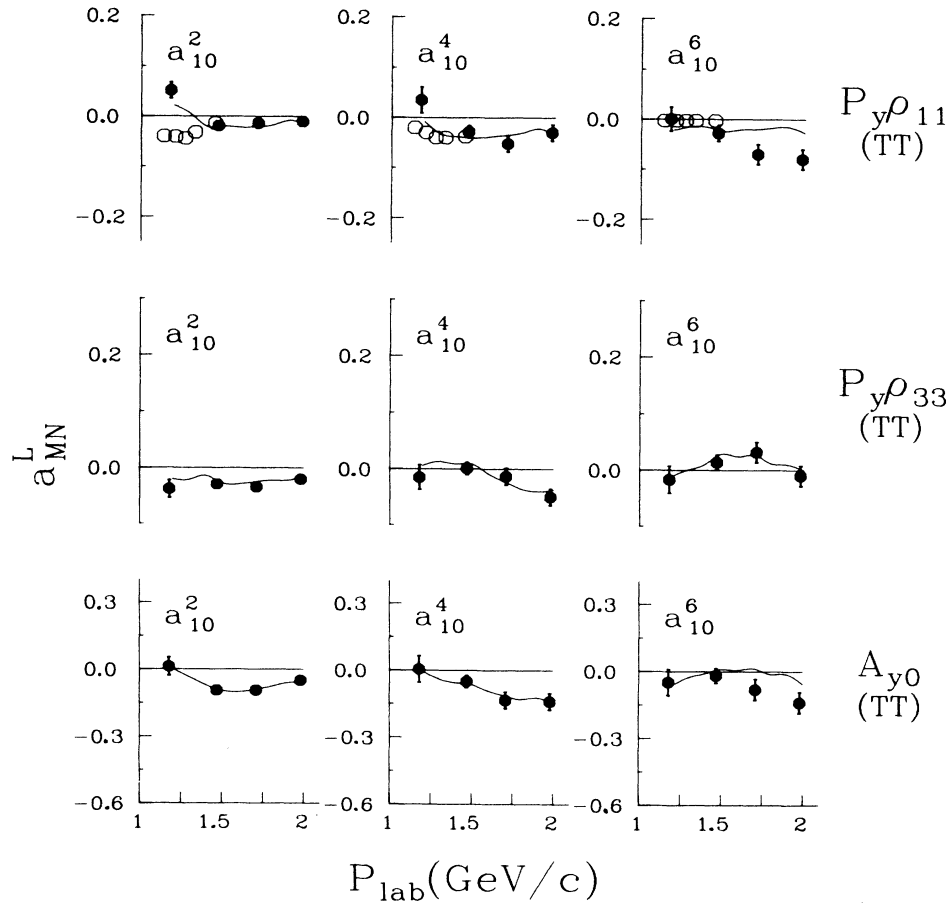


FIG. 21. Triplet-triplet interference moments ($L=2, 4$, and 6) for $P_y\rho_{11}$, $P_y\rho_{33}$, and A_y plotted against p_{lab} (Δ^{++} -band cuts imposed); the curves and open points are as in Fig. 20.

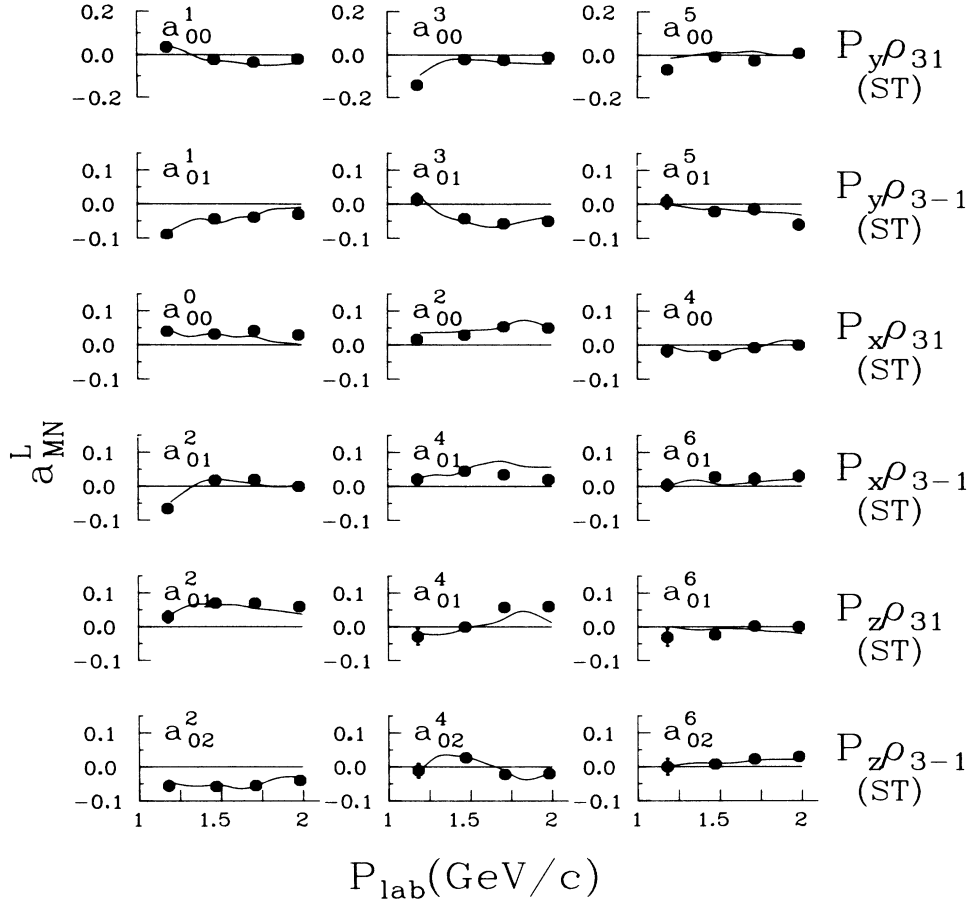


FIG. 22. Singlet-triplet interference moments for $P_y\rho_{31}$, $P_y\rho_{3-1}$, $P_x\rho_{31}$, $P_x\rho_{3-1}$, $P_z\rho_{31}$, and $P_z\rho_{3-1}$ plotted against p_{lab} (Δ^{++} -band cuts imposed); the curves are as in Fig. 20.

A. Preliminaries

We used the pion-exchange model to estimate the complexity needed for an accurate partial-wave expansion for $p_{\text{lab}} \leq 2.0$ GeV/c. Table VI lists the 59 partial waves which we retained, organized into four categories: (1) 10 “low partial waves” (LPW’s), taken to be complex in the fits; (2) 18 “high partial waves” (HPW’s), taken to be real; (3) 13 “very high partial waves” (VHPW’s), also taken to be real and fixed by the pion-exchange model; and (4) 18 non- Δ^{++} isobar waves, also fixed by the model with the isobar phases of Eq. (A2b). Only the Δ - Δ and p - Δ interference moments were used in the fits, not the $P_i\rho_{s_1}$ or $P_i\rho_{s-1}$ moments; thus, the fits were insensitive to the behavior of the s -wave $p\pi^+$ isobars.⁴⁹ Although only the Δ^{++} -production waves (LPW’s and HPW’s) were varied in the final fits, we verified that the results were insensitive to reasonable variations of the p -wave ($j^P = \frac{1}{2}^+$) $p\pi^+$ isobars. We also verified that relaxing the phase constraint on the larger HPW’s (1G_4 and 3H_5) did not alter the results; these waves took on $\sim 0^\circ$ and $\sim 180^\circ$ phases when varied freely. We did not explicitly include the Δ^+p

isobar waves in the fits, for reasons given in Sec. III and Appendix B. The reflections of these waves contribute mainly to the LPW’s and HPW’s, which were freely varied anyway in the fits; their contributions to the fixed waves (VHPW’s and p -wave isobars) are expected from the Wick transformations to be small.

One of the more critical assumptions in our analysis is that the HPW’s should be approximately real. Given unitarity phase factors $e^{i\delta_{pp} + \delta_{\Delta N}}$ for the transition amplitudes, this assumption implies that δ_{pp} should be small for the relevant proton-proton initial states. This happens to be true for all the HPW’s listed in Table VI, except for the transition $^3P_1 \rightarrow ^5F_1$. Setting this wave to zero did not alter the fit results significantly. Several of the p -isobar transitions, involving 1S_0 , 3P_0 , and 3P_1 initial states, also violate the requirement $\delta_{pp} \sim 0^\circ$; however, as noted above, these small non- Δ^{++} waves had little effect on the fit results.

Since we have used the pion-exchange model and the PSA predictions as a guide in finding reasonable solutions, it is useful to compare these directly with one another. Figure 24 shows the relative intensities of the

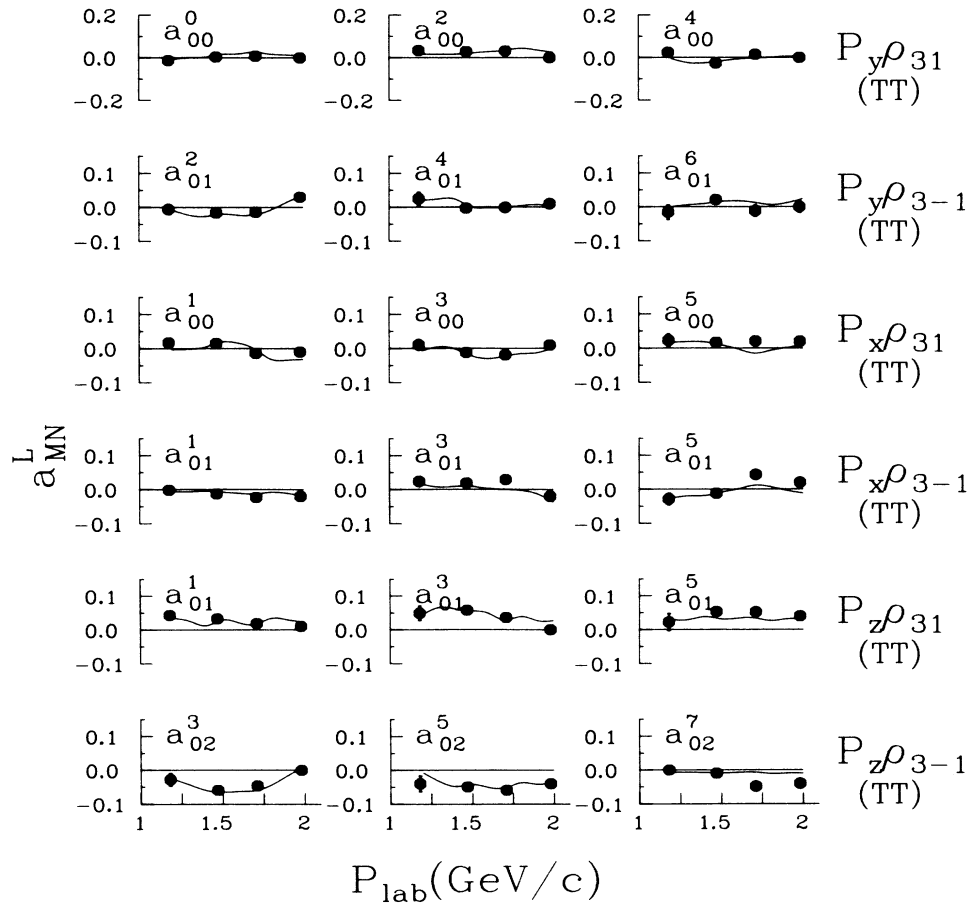


FIG. 23. Triplet-triplet interference moments for $P_y\rho_{31}$, $P_y\rho_{3-1}$, $P_x\rho_{31}$, $P_x\rho_{3-1}$, $P_z\rho_{31}$, and $P_z\rho_{3-1}$ plotted against p_{lab} (Δ^{++} -band cuts imposed); the curves are as in Fig. 20.

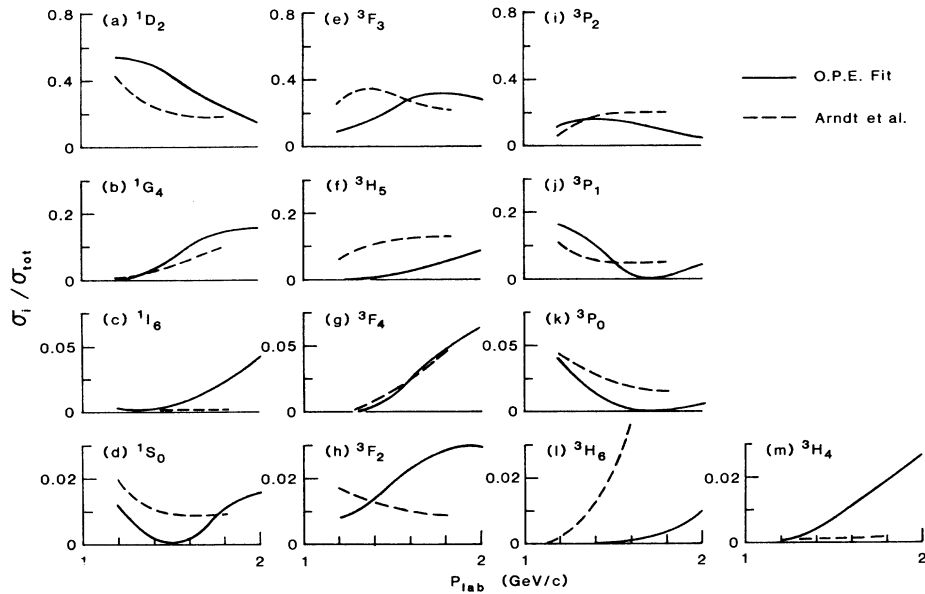


FIG. 24. Comparison of the partial-wave intensities expressed as fractions of the Δ^{++} -production cross section for the pion-exchange fits (solid curves) and the PSA of Ref. 24 (dashed curves).

TABLE VI. Listing of transition amplitudes according to type as specified in the text: LPW's (low partial waves), HPW's (high partial waves), VHPW's (very high partial waves), and s/p $j^P = \frac{1}{2}^{\pm}$ isobar production waves. Also listed are the fractions of the total cross sections for each collection of waves, as determined by the fits; the fractions are listed for both solutions as PSA (OPE).

	LPW	HPW	VHPW	s/p isobars
	$^1D_2 \rightarrow ^5S_2$	$^1D_2 \rightarrow ^3D_2$	$^1D_2 \rightarrow ^5G_2$	$^1S_0 \rightarrow ^3P_0$ (s)
	$^3P_0 \rightarrow ^3P_0$	$^1D_2 \rightarrow ^5D_2$	$^1G_4 \rightarrow ^3G_4$	$^3P_0 \rightarrow ^1S_0$ (s)
	$^3P_1 \rightarrow ^3P_1$	$^3P_1 \rightarrow ^5F_1$	$^1G_4 \rightarrow ^5G_4$	$^3P_1 \rightarrow ^3S_1$ (s)
	$^3P_1 \rightarrow ^5P_1$	$^3P_2 \rightarrow ^3F_2$	$^3F_3 \rightarrow ^5H_3$	$^1D_2 \rightarrow ^3P_2$ (s)
	$^3P_2 \rightarrow ^3P_2$	$^3P_2 \rightarrow ^5F_2$	$^3F_4 \rightarrow ^3H_4$	$^3P_1 \rightarrow ^3D_1$ (s)
	$^3P_2 \rightarrow ^5P_2$	$^3F_2 \rightarrow ^3F_2$	$^3F_4 \rightarrow ^5H_4$	$^3P_2 \rightarrow ^1D_2$ (s)
	$^3F_2 \rightarrow ^3P_2$	$^3F_2 \rightarrow ^5F_2$	$^3H_4 \rightarrow ^3H_4$	$^3P_2 \rightarrow ^3D_2$ (s)
	$^3F_2 \rightarrow ^5P_2$	$^3F_3 \rightarrow ^3F_3$	$^3H_4 \rightarrow ^5H_4$	$^3F_2 \rightarrow ^1D_2$ (s)
	$^3F_3 \rightarrow ^5P_3$	$^3F_3 \rightarrow ^5F_3$	$^3H_5 \rightarrow ^3H_5$	$^3F_2 \rightarrow ^3D_2$ (s)
	$^1S_0 \rightarrow ^5D_0$	$^3F_4 \rightarrow ^3F_4$	$^3H_5 \rightarrow ^5H_5$	$^3F_3 \rightarrow ^3D_3$ (s)
		$^3F_4 \rightarrow ^5F_4$	$^3J_6 \rightarrow ^3H_6$	$^1S_0 \rightarrow ^1S_0$ (p)
		$^1G_4 \rightarrow ^5D_4$	$^3J_6 \rightarrow ^5H_6$	$^3P_0 \rightarrow ^3P_0$ (p)
		$^3H_4 \rightarrow ^3F_4$	$^3J_7 \rightarrow ^5H_7$	$^3P_1 \rightarrow ^1P_1$ (p)
		$^3H_4 \rightarrow ^5F_4$		$^3P_1 \rightarrow ^3P_1$ (p)
		$^3H_5 \rightarrow ^5F_5$		$^3P_2 \rightarrow ^3P_2$ (p)
		$^1I_6 \rightarrow ^5G_6$		$^3F_2 \rightarrow ^3P_2$ (p)
		$^3H_6 \rightarrow ^3H_6$		$^1D_2 \rightarrow ^1D_2$ (p)
		$^3H_6 \rightarrow ^5H_6$		$^1D_2 \rightarrow ^3D_2$ (p)

(GeV/c)	Cross-section fractions			
	LPW	HPW	VHPW	s/p isobars
1.2	0.937 (0.831)	0.035 (0.142)	0.001 (0.001)	0.027 (0.026)
1.5	0.816 (0.804)	0.142 (0.155)	0.004 (0.004)	0.038 (0.036)
1.7	0.597 (0.610)	0.345 (0.332)	0.010 (0.010)	0.048 (0.047)

leading production waves as functions of p_{lab} , labeled by initial-state quantum numbers J , S_i , and L_i . The PSA predictions from Ref. 24 for the total inelastic cross sections are indicated by dashed curves, while our pion-exchange fits over the $pp \rightarrow \Delta^{++}n$ mass interval are shown as solid curves.⁵⁰ Both descriptions predict approximately the same ranking for the different waves, and require the 1D_2 , 3F_3 , and 3P_2 cross sections to dominate at low energies. The disagreements between the PSA and pion-exchange intensities shown in Fig. 24 are comparable to those reported in other comparisons between theoretical model inelasticities and the Arndt *et al.* PSA (Refs. 46, 51, and 52); there are discrepancies in the relative contributions of 1D_2 and 3F_3 , and also in some of the smaller waves, especially $^3H_{4,5,6}$ and 3F_2 . Given these discrepancies, we would not want to constrain the HPW's to agree precisely with either model, but we would expect the same approximate ranking of intensities in any viable solution. We remark that neither the pion-exchange predictions of Fig. 24, nor any of our PWA fits reported below, violate unitarity constraints on the partial-wave cross sections [cf. Eqs. (33) and (34)].

Finally, we note that small systematic uncertainties were included in the joint-moments fits.⁵³ These were meant to reflect the uncertainties in the fixed p -isobar contributions; they were also meant to allow for coherence effects due to possible wave-to-wave differences in $M_{p\pi^+}$ dependence (our moments are averaged over $M_{p\pi^+}$). We

note also that we tested all solutions for continuity by interpolating the joint moments in p_{lab} and refitting in 100-MeV/c p_{lab} intervals; this is the basis for the continuous fitted curves in Figs. 19–23.

B. Fitting strategies

We concentrate on two general fitting strategies, referred to as “PSA” and “OPE” (one-pion-exchange) fits. In the PSA fits, the LPW intensities (1S_0 , $^3P_{0,1,2}$, 1D_2 , and 3F_3 waves) were constrained loosely to agree with the PSA of Ref. 24, as displayed in Fig. 24. The HPW's were initially taken from the pion-exchange model, after rescaling the 1G_4 , 1I_6 , 3F_4 , and $^3H_{4,5,6}$ pion-exchange waves to agree with the PSA intensity predictions; these HPW starting values were optimized separately from the LPW's, and then smoothed to be monotonic functions of p_{lab} . The resulting HPW's used in the PSA fits are plotted in Fig. 25; for comparison, the original pion-exchange values for the HPW's are shown in Fig. 26. The relative phases (0° or 180°) are generally similar for the two sets of waves and reflect the pion-exchange helicity structure. The continuity test for the PSA solutions is illustrated in Fig. 27, which shows the real and imaginary parts of the LPW's in 100 MeV/c intervals. We note that the $^1S_0 \rightarrow ^5D_0$ transition (not shown) turned out to be small and poorly determined; it was set to zero in the final PSA fits. Also, we performed the PSA fits only for $p_{\text{lab}} \leq 1.7$

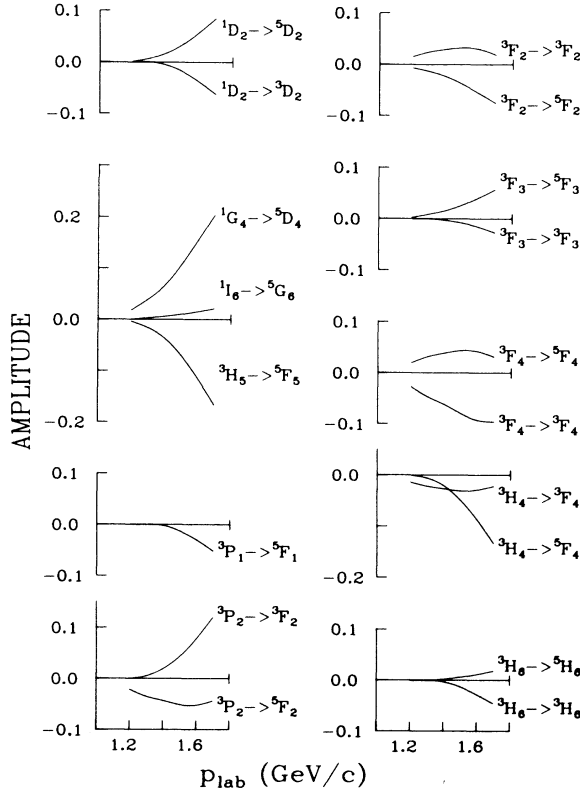


FIG. 25. Real parts of high partial curves for $pp \rightarrow \Delta^{++}n$ obtained in “PSA” fits (imaginary parts were set to zero). The normalization is consistent with Eq. (33).

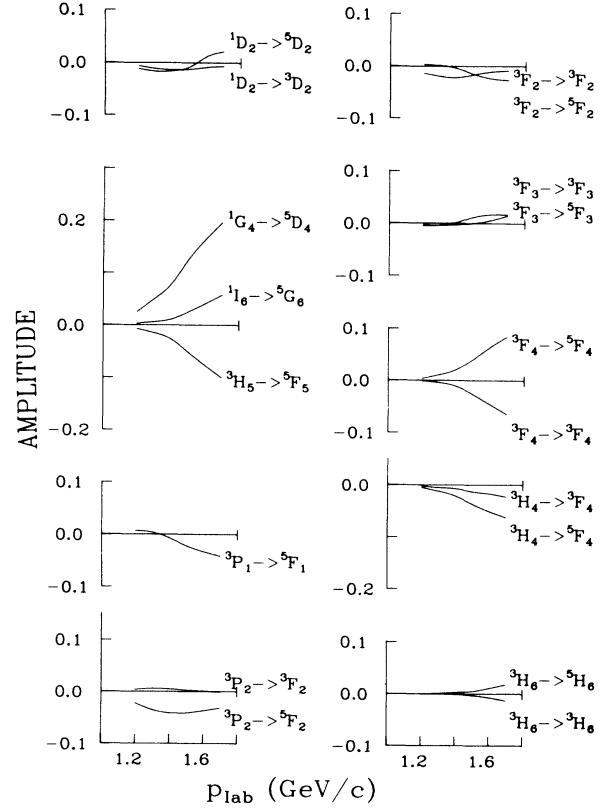


FIG. 26. Real parts of high partial waves for $pp \rightarrow \Delta^{++}n$ from the pion-exchange model.

GeV/c, where the elastic PSA constraints are expected to be reliable.

The second class of solutions, the OPE fits, did not utilize the PSA intensities directly. Instead, estimates of $\Delta\sigma_L$ and $\Delta\sigma_T$ for $pp \rightarrow \Delta N$ were included in the fits to help constrain the partial-wave cross sections. We discuss the determination of $\Delta\sigma_L$ and $\Delta\sigma_T$ from the elastic PSA and $p_1 p_1 \rightarrow \pi^+ d$ data below (Sec. VIID). We note here that $\Delta\sigma_{L,T}$ depend only on the partial-wave intensities, except for interference contributions associated with coupled-triplet waves (${}^3P_2 - {}^3F_2$, ${}^3F_4 - {}^3H_4$, etc.). We have used PSA estimates of the coupled-triplet terms as separate constraints in the OPE fits. Since these constraints are model dependent and (unlike total $\Delta\sigma_{L,T}$) not subject to direct measurement, we have performed fits with and without the coupled-triplet constraints (OPE and OPE-2 fits, respectively).

In the OPE and OPE-2 fits, the HPW’s were varied freely along with the LPW’s, and no attempt was made to smooth the HPW’s except that the large 1G_4 and 3H_5 waves were fixed by the pion-exchange model. The fitted HPW’s showed some scatter, but were qualitatively similar to the PSA results. The overall intensity breakdown for LPW’s, HPW’s, VHPW’s, and non- Δ contributions for

the OPE and PSA fits are compared in Table VI. The HPW cross section for the OPE fits is larger at 1.2 GeV/c than would be expected from either the elastic PSA or the pion-exchange model; despite this, the LPW’s turned out to be fairly similar for the OPE and PSA solutions at all energies. As a further variant, we repeated the OPE-2 fits using the HPW’s fixed by the pion-exchange model (cf. Fig. 26). These fits (OPE-3) gave worse χ^2 ’s but the LPW’s turned out to be quite similar to those of OPE-2.

Figure 28 compares the relative intensities of the leading waves for the OPE (data points) and PSA (smooth curves) solutions. Within errors the results are quite similar for the two solutions. If anything, the agreement is better than the theoretical comparison shown in Fig. 24 between pion-exchange and PSA intensity predictions. As in the PSA fits, the 1S_0 wave (not shown) turned out to be small ($< 1\%$ of the total) in all of the OPE fits. The OPE-2 fits, with no coupled-triplet constraints, gave systematically lower 3F_3 and higher 3F_2 intensities than the OPE values shown in Fig. 28.

We note that in both OPE and OPE-2 solutions, the 1D_2 and 3F_3 fractional intensities fall smoothly for $p_{\text{lab}} > 1.5$ GeV/c, compensated by increasing 3P_2 , 1G_4 , and ${}^3H_{4,5}$ intensities. We would expect to obtain larger

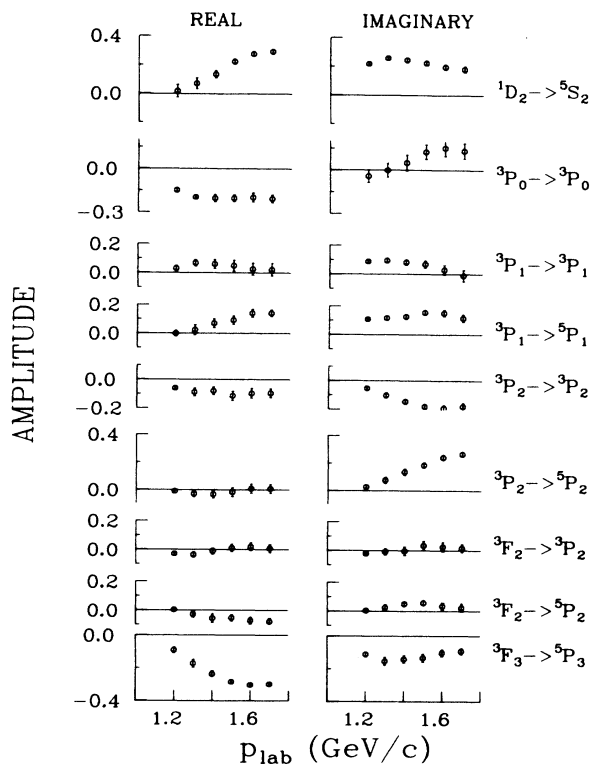


FIG. 27. Real and imaginary parts of low partial waves in $pp \rightarrow \Delta^{++}n$ obtained in "PSA" fits in 100 MeV/c intervals using p_{lab} -interpolated moments for continuity testing; normalization is consistent with Eq. (33).

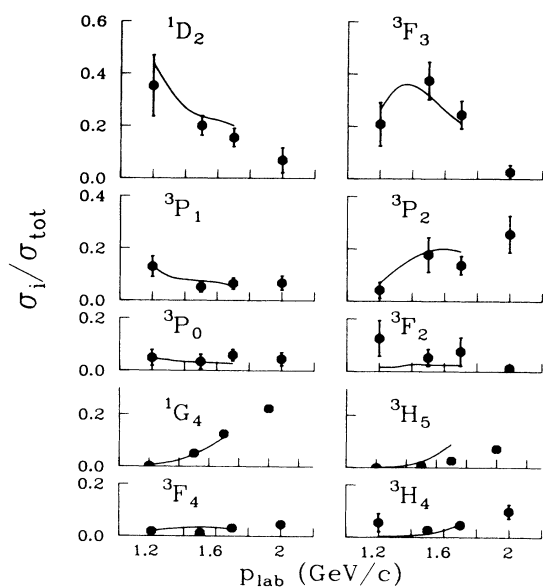


FIG. 28. Total relative intensities for the indicated proton-proton initial states for "PSA" fits (smooth curves) and "OPE" fits (data points) plotted against p_{lab} .

1D_2 and 3F_3 intensities above 1.7 GeV/c if constraints from the higher-energy Saclay-Geneva elastic PSA (Ref. 25) were imposed on the fits.

Figure 29 shows the LPW phases for the PSA and OPE solutions. The solid curves depict the results of the continuity-test fits. The only major differences between the OPE and OPE-2 results occurred in the 1D_2 and 3P_2 phases, and the behavior of these OPE-2 phases are shown as separate dashed curves in Fig. 29(j) and 29(o). As noted above, the OPE-3 results (using pion-exchange values for the HPW's) were very close to those shown in Fig. 29 for OPE and OPE-2. Although some of the waves (especially 3F_2) tend to be poorly determined, the behavior of the larger waves is similar for the PSA and OPE solutions. In particular, the 1D_2 , 3F_3 , and $^3P_{0,1,2}$ phases are generally stationary or clockwise rotating with increasing p_{lab} . Near threshold, the phases are somewhat different for the PSA and OPE solutions, with the 1D_2 wave executing a stronger clockwise phase variation above 1.2 GeV/c for the OPE solutions.

Table VII lists the fit χ^2 's for the various PSA and OPE solutions. The solid curves in Figs. 19–23 illustrate the OPE solutions for the joint moments.

C. Ambiguities and overall phase behavior

To search for discrete ambiguities, we experimented with random LPW phases in the starting values for the fits. At the lower energies we can generally obtain one variant solution for each fitting strategy; the differences

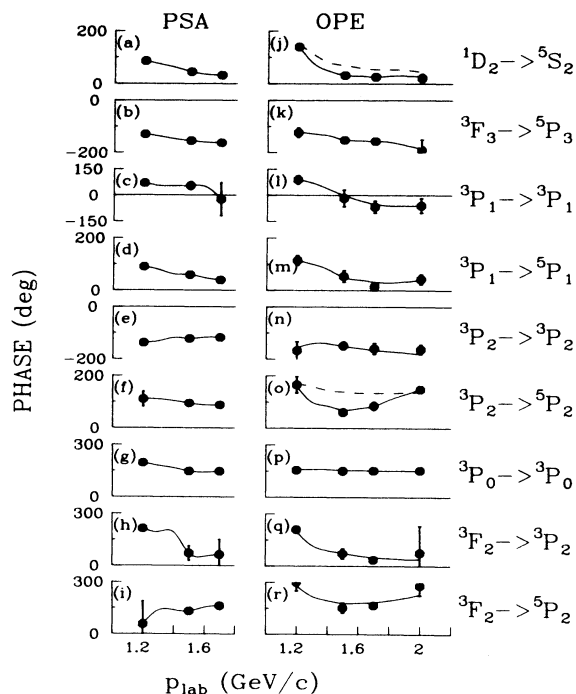


FIG. 29. Phases for low partial waves obtained in "PSA" (a)–(i) and "OPE" (j)–(r) fits. Solid curves depict the continuity test results in each case. The dashed curves in (j) and (o) indicate phases from "OPE-2" solution, obtained by relaxing the constraint on the coupled-triplet spin correlation.

TABLE VII. Values of χ^2 per degree of freedom for “PSA” fits and three variants of “OPE” fits described in text. The χ^2 refers only to the joint-moments contributions; the number of degrees of freedom includes the subsidiary constraints imposed on the different fits. For the “PSA” solutions we have not counted the HPW’s as parameters; these were optimized by separate fits as described in the text, then fixed in fits for the LPW’s.

p_{lab} (GeV/c)	“PSA”	“OPE”	“OPE-2” No coupled- triplet constraint	“OPE-3” HPW fixed
1.2	85/51	32/28	30/27	126/47
1.5	49/68	28/45	24/44	138/64
1.7	87/68	68/45	52/44	141/64
2.0		68/45	67/44	

lie mainly in the behavior of the $^3P_2 \rightarrow ^5P_2$ and $^3F_2 \rightarrow ^5P_2$ phases near threshold and are roughly comparable to the differences between the PSA and OPE results for these waves in Fig. 29. We would therefore regard the threshold behavior of these (small) waves as poorly determined. Otherwise we do not find viable solutions which differ significantly in the behavior of the larger waves.

To understand better the sensitivity of the fits to the overall phases, we repeated the OPE fits at each p_{lab} , fixing the $^1D_2 \rightarrow ^5S_2$ phase at discrete values and fitting the remaining waves as functions of the phase, $\phi(^1D_2)$. We verified that the behavior of fit χ^2 vs $\phi(^1D_2)$ was consistent with the errors on the $^1D_2 \rightarrow ^5S_2$ phases shown in Fig. 29. These fits generated a continuous family of solutions at each energy characterized by the values of $\phi(^1D_2)$. We noted above that the PSA solution gives a lower value for the $^1D_2 \rightarrow ^5S_2$ phase at 1.2 GeV/c than any of the OPE solutions. It turns out that the PSA solutions at 1.2 GeV/c (both the LPW and HPW values) lies very close to the OPE family of solutions, with the lower value of $\phi(^1D_2)$.

Figure 30 shows the best fit results for the $^1D_2 \rightarrow ^5S_2$ phases versus p_{lab} for the PSA and OPE, OPE-2, and OPE-3 solutions. The error bars at 1.2 and 1.5 GeV/c indicate the 95% confidence limits ($\Delta\chi^2=3.84$) on $\phi(^1D_2)$ from the OPE solutions. Also shown is a hypothetical Breit-Wigner phase, based on 1D_2 resonance parameters suggested by Yokosawa¹ ($M=2.155$ GeV, $\Gamma=0.1$ GeV). Setting $\phi(^1D_2)$ to the Breit-Wigner value at 1.5 GeV/c increases the OPE fit χ^2 by 22 for one degree of freedom. It is clear that none of the solutions suggest Breit-Wigner behavior. In the case of the PSA and OPE-3 solutions, one might argue that the $^1D_2 \rightarrow ^5S_2$ phase is constrained by the model dependence of the HPW’s. In the OPE and OPE-2 solutions, the assumptions made on the HPW’s are fairly minimal (they are taken to be relatively real) but the solutions for $\phi(^1D_2)$ still exclude Breit-Wigner behavior.

D. Use of $\Delta\sigma_L$ and $\Delta\sigma_T$ constraints

We comment briefly on the use of $\Delta\sigma_L$ and $\Delta\sigma_T$ constraints in the OPE fits. In principle, a complete set of spin correlations for $p, p_1 \rightarrow p\pi^+n$, as classified in Table

III, would be desirable for the PWA, and measurements have been reported at very low energies.⁹ For our analysis we used values of inelastic $\Delta\sigma_{L,T}$ predicted by the PSA of Ref. 24; we corrected these explicitly for $pp \rightarrow \pi^+d$ contributions, using available A_{xx} , A_{yy} , and A_{zz} data from Refs. 54–56 and differential cross section data from Refs. 3 and 57. To use the corrected $\Delta\sigma_{L,T}$ in our fits, we made the assumption that the ratios $\Delta\sigma_{L,T}/\sigma$ should be the same for the Δ^{++} -band $p\pi^+n$ final state as for the total $NN\pi$ final state. The first Legendre coefficients of Table

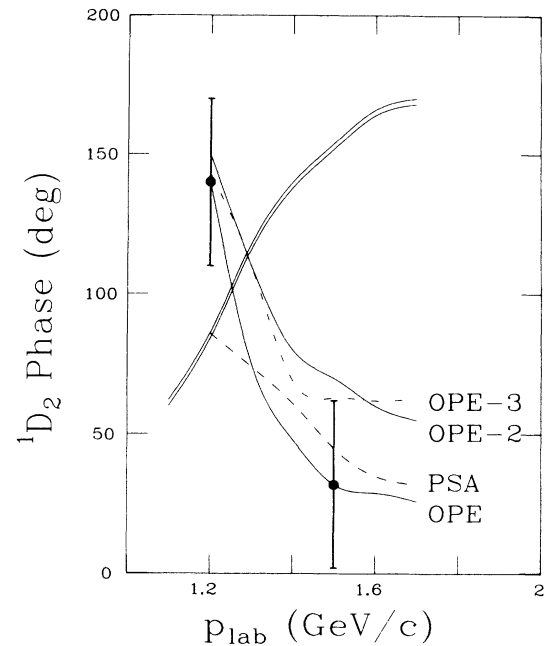


FIG. 30. Phase of $^1D_2 \rightarrow ^5S_2$ vs p_{lab} for “OPE” (lower solid), “OPE-2” (upper solid), “OPE-3” (upper dot-dashed), and “PSA” (lower dashed) solutions. Double solid curve depicts nominal Breit-Wigner behavior. Error bars indicate 95% confidence limits from “OPE” fits at 1.2 and 1.5 GeV/c.

III can then be related to $\Delta\sigma_{L,T}/\sigma$ as

$$\Delta\sigma_L/\sigma = -8[a_{00}^0(A_{zz}\rho_{11}) + a_{00}^0(A_{zz}\rho_{33})], \quad (43a)$$

$$\Delta\sigma_T/\sigma = -4[a_{00}^0(A_{xx}\rho_{11}) + a_{00}^0(A_{xx}\rho_{33}) + a_{00}^0(A_{yy}\rho_{11}) + a_{00}^0(A_{yy}\rho_{33})]. \quad (43b)$$

Our estimates for the various $\Delta\sigma_{L,T}$ components are listed in Table VIII, together with the OPE-fit results. Similar estimates below 1.2 GeV/c have been given by Aprile-Giboni *et al.*⁵⁸ The estimates given by Auer *et al.*⁵⁹ for inelastic $\Delta\sigma_L$ are systematically higher than ours, but are not inconsistent with our fit results.

The elastic PSA also predict the coupled-triplet interference contributions to $\Delta\sigma_L$ and $\Delta\sigma_T$ involving ${}^3P_2 - {}^3F_2$ and ${}^3F_4 - {}^3H_4$ waves. In the notation of Arik and Williams,⁶⁰ these interferences can be expressed in terms of parameters I_J^x ,

$$\Delta\sigma_T = 2 \sum_J I_J^x, \quad (44a)$$

$$\Delta\sigma_L = -4 \sum_J I_J^x, \quad (44b)$$

where

$$I_2^x = \frac{4\pi}{k^2} [J(J+1)]^{1/2} \sum_i ({}^3P_2 \rightarrow i)({}^3F_2 \rightarrow i)^*, \quad (44c)$$

and so on for $J=4, 6, \dots$. The I_J^x can be separated further into elastic and inelastic pieces, corresponding to the final states i , in Eq. (44c). The PSA also predict the total I_J^x by unitarity, viz.,

$$I_2^x = \frac{4\pi}{k^2} [J(J+1)]^{1/2} \text{Im}({}^3P_2 \rightarrow {}^3F_2)_{pp \rightarrow pp}. \quad (45)$$

The PSA predictions for inelastic I_J^x then follow by subtraction of elastic [Eq. (44c) with $i =$ proton-proton] from total [Eq. (45)]. The inelastic contributions to $\Delta\sigma_{L,T}$ from $pp \rightarrow \Delta N$ can be deduced from Eq. (44) or equivalently from the first Legendre moments involving ${}^3P_2 - {}^3F_2$ interferences in Table III. The results for the ${}^3P_2 - {}^3F_2$ waves are given in Table VIII for PSA predictions and fit results. With no coupled-triplet constraints, the OPE-2 fits differ markedly from the PSA predictions at 1.5 and 1.7 GeV/c. With (loose) constraints, the OPE fits agree with the PSA within reasonable systematic uncertainties. We note that the PSA predictions depend sensitively on several fine details, notably the 3P_2 and 3F_2 inelasticities, the mixing angle ϵ , and the phase-shift sum

$\delta({}^3P_2) + \delta({}^3F_2)$; our OPE-2 fits indicate somewhat different inelasticities for these waves than the PSA.

E. Comparison of $pp \rightarrow p\pi^+n$ and $pp \rightarrow \pi^+d$ partial waves

We turn lastly to comparison with the $pp \rightarrow \pi^+d$ partial waves reported by Bugg.⁶¹ Bugg's analysis utilized high-quality data on single-spin asymmetries A_{y0} and iT_{11} and two-spin correlations A_{xx} , A_{yy} , A_{zz} , and A_{xz} . *A priori*, we would not expect the relative intensities of the different partial waves to be identical in $pp \rightarrow \Delta N$ and $pp \rightarrow \pi^+d$, for reasons given in Sec. V A; however, we might expect the dependence of a given partial-wave phase on p_{lab} to be similar for the bound and free nucleon final states.

That the partial-wave intensities differ for the two reactions can be inferred from the gross behavior of $\Delta\sigma_L/\sigma$ and $\Delta\sigma_T/\sigma$ in Table VIII. The ratios $\Delta\sigma_{L,T}/\sigma$ are bigger for the π^+d final state than for the remainder of the inelastic cross section, suggesting a stronger singlet component in π^+d than in ΔN . This is consistent with the PWA results; the 1D_2 intensity is $\sim 40\%$ at maximum in our $pp \rightarrow \Delta N$ fits, compared with $\sim 60\%$ for $pp \rightarrow \pi^+d$. This difference is more or less as expected. First, the angular-momentum selection rules favor singlet states in $pp \rightarrow \pi^+d$, as discussed in Sec. V A. Second, deuteron production requires $M_{p\pi^+}^0$ in Eq. (39b) to be close to the upper kinematic limit, where $L_f = 0$ (e.g., ${}^1D_2 \rightarrow {}^5S_2$) transitions should be enhanced. In this connection, we note that A_{xx} , A_{yy} , and A_{zz} , reported by Shypit *et al.*⁹ for $p_1 p_1 \rightarrow p\pi^+n$ at lower energies, tend also to approach extrema ($A = -1$) near the $M_{p\pi^+}$ kinematic limit.

Similarities in the phase behavior for $pp \rightarrow \pi^+d$ and $pp \rightarrow \Delta N$ might be expected with the following caveats. First, some explicit $M_{p\pi^+}$ dependence may be expected in the $pp \rightarrow \Delta^{++}n$ partial-wave phases, for example, from reflections of the Δ^+p isobars; this would affect deuteron production through the kinematical condition on $M_{p\pi^+}^0$ of Eq. (39b). Second, the s -wave $p\pi^+$ isobar contributions, which are isolated in $pp \rightarrow p\pi^+n$ through the ρ_{s1}, ρ_{s-1} observables, cannot be separated in $pp \rightarrow \pi^+d$; they are expected to be most important for the 3P_1 transitions, which allow overall $L_f = 0$ for the $(p\pi^+)_s - n$ isobar pairing. Despite these caveats, the comparison of A_{y0} ($pp \rightarrow \pi^+d$) and $P_y \rho_{11}$ ($pp \rightarrow \Delta N$) in Sec. IV suggests qualitative similarities in the phase behavior of the larger waves.

In the $pp \rightarrow \pi^+d$ PWA (Ref. 61), it has been customary to include explicitly the $\Delta^{++} \rightarrow p\pi^+$ Breit-Wigner phase

TABLE VIII. Values of $\Delta\sigma_{L,T}$ and $\Delta\sigma/\sigma$ used in PWA fits for inelastic (in), $pp \rightarrow \pi^+d$, and $pp \rightarrow NN\pi$; values of $\Delta\sigma_{L,T}/\sigma$ in parentheses show "OPE" fit results. Also listed are the coupled-triplet contributions to $\Delta\sigma_T/\sigma(2I_2^x/\sigma)$ used in fits; values in parentheses refer to OPE and OPE-2 fit results obtained, respectively, with and without the coupled-triplet constraints.

p_{lab} (GeV/c)	$\Delta\sigma_L^{\text{in}}$ (mb)	$\Delta\sigma_T^{\text{in}}$ (mb)	$\Delta\sigma_L^{\pi d}$ (mb)	$\Delta\sigma_T^{\pi d}$ (mb)	$\frac{\Delta\sigma_L^{\pi d}}{\sigma}$	$\frac{\Delta\sigma_T^{\pi d}}{\sigma}$	$\frac{\Delta\sigma_L^{NN\pi}}{\sigma}$	$\frac{\Delta\sigma_T^{NN\pi}}{\sigma}$	$\frac{2I_2^x}{\sigma}$
1.2	3.2	8.0	2.7	3.7	0.87	1.19	+0.06 (0.09)	+0.53 (0.50)	-0.03 (+0.02, +0.13)
1.5	-6.7	5.0	~ 0.2	~ 1.0	~ 0.25	~ 1.25	-0.34 (-0.28)	+0.20 (0.18)	-0.07 (-0.04, +0.16)
1.7	-4.0	4.8	~ 0	~ 0.5	~ 0	~ 1.0	-0.20 (-0.04)	+0.22 (0.23)	-0.07 (-0.02, +0.09)
2.0	~ 0	4.5	~ 0	~ 0	~ 0	~ 0	+0.02 (+0.17)	+0.21 (0.26)	-0.08 (-0.06, -0.02)

appropriate to the ΔN intermediate state, so that all $pp \rightarrow \pi^+ d$ waves are assigned a looping behavior on the Argand plots. In our $pp \rightarrow \Delta^{++} n$ PWA, we have shown production wave phases (i.e., without the common $\Delta^{++} \rightarrow p\pi^+$ decay phase). Thus, to make comparisons between the two reactions it is convenient to compare relative phases using the 1D_2 as a reference wave. In Bugg's analysis seven LPW's were fitted ($a_0, \dots, a_6 = {}^1S_0, {}^3P_1, {}^1D_2, {}^3P_1^*, {}^3P_2, {}^3F_2$, and 3F_3); the HPW and the phase of 1D_2 were constrained by theory. Figure 31 compares the relative phases for ${}^3F_3, {}^3P_1, {}^3P_2, {}^3F_2, {}^1G_4$, and 3H_5 for Bugg's analysis and our PSA solution, using 1D_2 as a reference in each case. In this comparison we have (a) rotated all odd-parity $pp \rightarrow \Delta N$ waves by 180° to accommodate the phase conventions of Ref. 52, and (b) rotated $a_3 = {}^3P_1^*$ by 180° .

There are inherent ambiguities in this comparison in that the ${}^3P_1, {}^3P_2$, and 3F_2 waves allow two lowest orbital final states in $pp \rightarrow \Delta N$ ($S_f = 1, 2$) compared with one in $pp \rightarrow \pi^+ d$ ($S_f = 1$). For 3P_2 and 3F_2 this ambiguity is resolved by noting that the $S_f = 2$ $pp \rightarrow \Delta N$ transitions contribute mainly to helicity- $\frac{3}{2}$ Δ production and are

therefore not important as intermediate states in $pp \rightarrow \pi^+ d$. For 3P_1 we have simply displayed all four waves: ${}^3P_1 \rightarrow {}^3S_1$ (a_1) and ${}^3P_1 \rightarrow {}^3D_1$ (a_4) for $pp \rightarrow \pi^+ d$, and ${}^3P_1 \rightarrow {}^3, {}^5P_1$ for $pp \rightarrow \Delta^{++} n$.

Figure 31 indicates that the relative phases of the larger waves vary slowly with p_{lab} for both the ΔN and $\pi^+ d$ final states. An exception to this is the clockwise motion of the 3P_1 phase in $pp \rightarrow \pi^+ d$ above threshold, a behavior which Bugg⁶¹ attributes to the $p\pi^+$ s -wave isobar contribution expected for this wave. Overall the level of agreement between the two solutions is fairly good.

The combination of ΔN and $\pi^+ d$ data extends the dibaryon study from threshold to above the 3F_3 peak. Also important is the fact that the $pp \rightarrow \pi^+ d$ PWA is constrained by two-spin correlations, especially A_{xz} . The A_{y_0} and A_{xz} correlations are closely related, as indicated in Table III (cf. $P_y \rho_{11}$ and $A_{xz} \rho_{11}$). For example, with only 1D_2 and 3F_3 waves we would have

$$-A_{y_0} \sim \text{Im}^1 D_2 {}^3 F_3^* , \quad (46a)$$

$$A_{xz} \sim \text{Re}^1 D_2 {}^3 F_3^* , \quad (46b)$$

so that comparison of A_{y_0} and A_{xz} would help to determine more precisely the quadrant for the ${}^3F_3 - {}^1D_2$ relative phase in the absence of other waves. Experimentally, A_{y_0} and A_{xz} are generally opposite in sign for $pp \rightarrow \pi^+ d$ above 1.1 GeV/c (Refs. 54, 56, and 62) indicating like signs for $\text{Im}^1 D_2 {}^3 F_3^*$ and $\text{Re}^1 D_2 {}^3 F_3^*$. Also the ratio $|A_{xz}/A_{y_0}|$ generally increases with p_{lab} , suggesting an asymptotic limit of $\sim 180^\circ$ for the ${}^3F_3 - {}^1D_2$ relative phase (0° with Bugg's phase conventions in Fig. 31). Both of these features emerge naturally in our $pp \rightarrow \Delta^{++} n$ solutions without benefit of A_{xz} data. The asymptotic phase behavior is consistent with the pion-exchange model; unnatural-parity exchange at high energies requires 180° relative phase between the singlet and uncoupled triplet waves (${}^1D_2 \sim -{}^3F_3, {}^1G_4 \sim -{}^3H_5$, etc.).

F. Summary

We have presented PWA solutions for $pp \rightarrow \Delta^{++} n$ using the joint moments from this experiment and constraints based on the elastic PSA and $\Delta\sigma_L$ and $\Delta\sigma_T$. The behavior of the relative phases of the larger partial waves appears to be similar to $pp \rightarrow p\pi^+ n$ and in $pp \rightarrow \pi^+ d$; the relative phases vary only slowly with p_{lab} and do not suggest Breit-Wigner behavior in any single wave from below the 1D_2 to above the 3F_3 peaks. The absolute phases in our solutions depend on the treatment of the HPW and are less well constrained close to threshold. However, all of the larger waves rotate clockwise in our solutions, whether we constrain the HPW's to be smooth functions (PSA and OPE-3 solutions) or allow the HPW's to vary freely (OPE and OPE-2 solutions). We find no evidence for the counterclockwise phase motion expected for coupled-channel Breit-Wigner resonances.

VIII. SUMMARY

We have presented density-matrix elements and single-spin correlations for $p_1 p \rightarrow p\pi^+ n$ from 1.18 to 1.98 GeV/c based on total statistics of 2.4×10^6 events. We

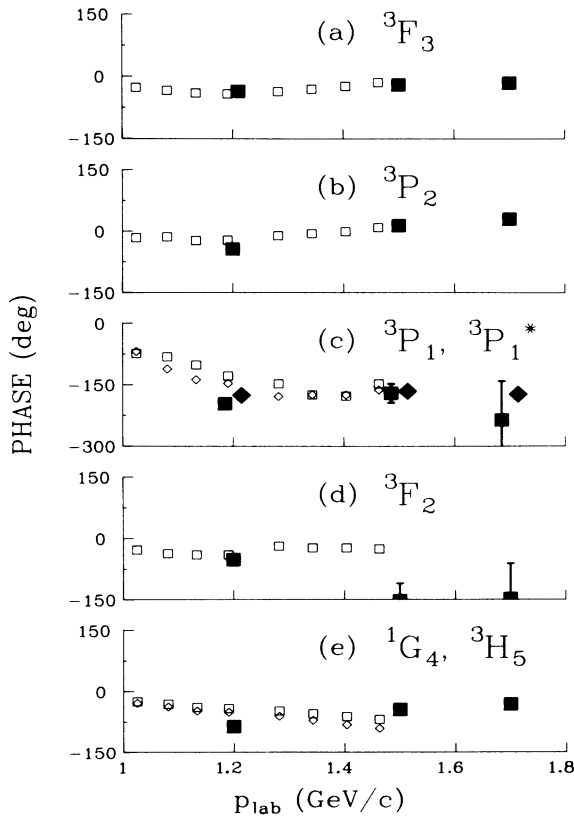


FIG. 31. Phases of low partial waves relative to 1D_2 wave for $pp \rightarrow \pi^+ d$ from Bugg (Ref. 61, open points) and $pp \rightarrow \Delta^{++} n$ ("PSA" solution, solid points). The 3P_1 phases in (c) refer to a_1 (open squares), $-a_3$ (open diamonds), ${}^3P_1 \rightarrow {}^3P_1$ (solid squares), and ${}^3P_1 \rightarrow {}^5P_1$ (solid diamonds). The $pp \rightarrow \pi^+ d$ phases in (e) refer to 1G_4 (open squares) and 3H_5 (open diamonds); for $pp \rightarrow \Delta^{++} n$, the 1G_4 and 3H_5 relative phases are identical (solid squares). In (b) and (d) the $pp \rightarrow \Delta^{++} n$ phases refer to ${}^3P_2 \rightarrow {}^3P_2$ and ${}^3F_2 \rightarrow {}^3P_2$, respectively.

have focused on the two-body process $pp \rightarrow \Delta^{++} n$, although our analysis allows for non- Δ^{++} backgrounds. The description that we have used is kinematically complete in that it separates explicitly the dependence on production (Θ_Δ) and decay angles (θ, ϕ) for $pp \rightarrow \Delta^{++} n$. We have displayed the DME's and SSC's directly as functions of production angle and $M_{p\pi^+}$, and in a compact form using joint moments which summarize the Θ_Δ dependence. The joint moments can be conveniently related to the partial-wave expansion, and we have presented formalism and numerical relations needed to interpret 0-, 1-, and 2-spin correlations. We have used the joint moments, averaged over Δ^{++} mass, as input to partial-wave analysis. Our results, combined with similar analysis on $pp \rightarrow \pi^+ d$, allow model-independent conclusions on the nature of the "dibaryon resonance" candidates.

In conjunction with small- t measurements on $p_1 p \rightarrow \Delta^{++} n$ made with the same apparatus from 3 to 12 GeV/c (Ref. 2), our data provide a detailed picture of $pp \rightarrow \Delta N$ from threshold to high energies. Over this energy range the spin-averaged observables show only gradual p_{lab} dependence, and the features of the DME's at small t are similar to those in other reactions dominated by absorbed pion exchange. The single-spin asymmetries, on the other hand, show some dramatic energy dependences. The overall production asymmetry $A_y(p_1 p \rightarrow \Delta^{++} n)$ is substantial at all energies; at maximum, A_y varies from +40% near threshold to $\sim -35\%$ above 1.7 GeV/c, remaining generally negative up to 12 GeV/c. Using the SSC's to separate helicity- $\frac{1}{2}$ and helicity- $\frac{3}{2}$ Δ production, we find that the helicity- $\frac{1}{2}$ component of A_y falls gradually with p_{lab} , going from generally positive below 2 GeV/c to negative at higher energies; the low-energy behavior mirrors the production asymmetry in $p_1 p \rightarrow \pi^+ d$, as expected on kinematical grounds. We find that the helicity- $\frac{3}{2}$ production asymmetry changes sign between 1.2 and 1.5 GeV/c and remains negative at high energies; this component tends to dominate A_y for large production angles. The SSC's also project out various helicity- $\frac{1}{2}$ and helicity- $\frac{3}{2}$ interference terms, all of which appear to evolve smoothly with p_{lab} from threshold to high energies.

We have considered several mechanisms which can lead to nontrivial amplitude phases, and hence to nonzero spin correlations. For example, the different isobar phases (given approximately by the πN elastic phase shifts) are expected to lead to interference effects between the different final-state configurations $pp \rightarrow \Delta^{++} n$, $pp \rightarrow \Delta^+ p$, and $pp \rightarrow (p\pi^+, J^P = \frac{1}{2}^\pm) n$. However, we find that the magnitudes of these effects are small and that the bulk of the spin dependence must be attributed to interference of different production waves for $pp \rightarrow \Delta^{++} n$. Overall, the behavior of the SSC's seems to require a fairly complex phase structure in the $pp \rightarrow \Delta N$ waves.

We have explored several approaches to partial-wave fits, obtaining similar results in all cases. Our solutions incorporate features which are expected on physical grounds. (1) The high partial waves are constrained to be relatively real and serve as a phase reference; their relative signs are generally consistent with absorbed pion ex-

change, as required for unnatural-parity-exchange dominance of the helicity amplitudes at small t . (2) The intensity distributions of the large waves are similar to predictions from the elastic PSA. Also the fitted values of inelastic $\Delta\sigma_L$ and $\Delta\sigma_T$, which are sensitive to the partial-wave intensities, are consistent with the PSA and with experimental spin-correlation data. (3) The relative phases obtained in our PWA show similar p_{lab} dependence as found in $pp \rightarrow \pi^+ d$ (Ref. 61); we would expect the larger $pp \rightarrow \Delta N$ transition phases to be similar for free and bound $pn\pi^+$ final states.

The main results of the PWA fits are that the low partial waves, involving S - and P -wave ΔN final states, generally rotate clockwise with increasing p_{lab} (in a sense opposite to Breit-Wigner behavior). Similar clockwise phase variation also characterizes those S and P waves that have large phase shifts in elastic nucleon-nucleon scattering, namely 1S_0 , 3S_1 , 3P_0 , 1P_1 , and 3P_1 . Thus, our results suggest at least a generic similarity between the large waves in $NN \rightarrow NN$ and $N\Delta \rightarrow N\Delta$. Neither the absolute nor the relative phases suggest Breit-Wigner behavior in any of the large ΔN waves. In particular, we conclude that the 1D_2 and 3F_3 waves do not involve coupled-channel Breit-Wigner resonances; if anything, the behavior of these waves may indicate ΔN virtual bound states, which would account for the resonancelike phase variations observed in $pp \rightarrow pp$. While these conclusions are generally consistent with conventional dynamical interpretations of dibaryons, more detailed understanding of the pp - ΔN coupled waves will require high-statistics data, including two-spin correlations, over a finer grid in p_{lab} .

ACKNOWLEDGMENTS

We acknowledge the technical assistance of I. Ambats, J. Dawson, L. Filips, and E. Walschon. We thank R. Ely, C. Klindworth, R. Rivetna, and S. Watson for help with online computers and offline processing, and the ZGS staff for the smooth operation of the accelerator. This work was supported by the U.S. Department of Energy under Contract No. W-31-109-ENG-38.

APPENDIX A

We have developed a parametrization based on the Williams model⁴¹ to describe the pion-exchange amplitudes of Fig. 4(a) at higher energies.² In this model the production amplitudes are relatively real except for the s , p , and Δ isobar phase factors given by $\sin\delta_{jj} e^{i\delta_{jj}}$. The model describes the spin-averaged DME's from 3 to 12 GeV/c fairly well with seven parameters; it also predicts the larger s - Δ interference spin correlations $P_y\rho_{s-1}$ and $P_x\rho_{s-1}$ correctly. It does not explain the large values of A_y and other spin correlations because it allows only $\text{Im}s^*\Delta$ and $\text{Im}p^*\Delta$ interferences and ignores $\text{Im}\Delta^*\Delta$ contributions, due to the assumption of relatively real Δ -production phases.

We have extrapolated the parametrization to lower energies and have carried out five-parameter fits at each energy to the DME's ρ_{11} , ρ_{33} , ρ_{31} , and ρ_{3-1} . The model correctly predicts that the partial waves 1D_2 , 3F_3 , and 3P_2 should dominate the low-energy cross sections, as a conse-

quence of the helicity structure of the pion-exchange amplitudes. Although the model is clearly a very crude approximation, it may be adequate to describe the smaller amplitudes, namely the s - and p -wave isobar production and the high partial waves for Δ production.

The parametrization is described in Ref. 2. Briefly, we decompose the helicity amplitudes used in Eqs. (27)–(30) into Born terms and absorptive corrections:

$$A_{\lambda_n \lambda_t}^{M \lambda_b} = A_{\lambda_n \lambda_t}^{M \lambda_b}(\text{Born}) + A_{\lambda_n \lambda_t}^{M \lambda_b}(\text{abs}). \quad (\text{A1})$$

The Born terms take a simple form in the t -channel frame:

$$A_{(1/2)(1/2)}^{(1/2)(1/2)}(\text{Born}) = \frac{\sqrt{-t}}{(-t + m_{\pi^+}^2)} e^{Bt'} F(M_{p\pi^+}), \quad (\text{A2a})$$

with

$$F(M_{p\pi^+}) = G \left[\frac{m_N^2 k k'}{2\pi s} \right]^{1/2} \frac{M_{p\pi^+}}{\sqrt{q_p}} \frac{\sqrt{2j+1}}{2} \sin \delta_{jl} e^{i\delta_{jl}}, \quad (\text{A2b})$$

$$G = \left[\frac{G_{NN\pi}^2}{2\pi m_N^2} \right]^{1/2} \simeq 3.60 \text{ mb}^{1/2}. \quad (\text{A2c})$$

Here B and G are taken as free parameters; $t' = t - t_{\min}$; k (k') are initial- (final-) state c.m. momenta for $pp \rightarrow (p\pi^+)n$; q_p is the momentum of the final proton in the $p\pi^+$ c.m.; s is the total c.m. energy squared; and δ_{jl} are the π^+p elastic phase shifts. The other helicity amplitudes are obtained by parity conservation [Eq. (28)] and by the naturality relation

$$A_{\lambda_n \lambda_t}^{M \lambda_b} = \xi (-1)^{\lambda_n - \lambda_t} A_{-\lambda_n - \lambda_t}^{M \lambda_b}, \quad (\text{A3})$$

where $\xi = -1$ for the Born terms ($\xi = +1$ for natural-, -1 for unnatural-parity exchange).

The Born terms do not allow $M = \pm \frac{3}{2}$ in the t channel and consequently predict $\rho_{33} = \rho_{31} = \rho_{3-1} = 0$ in the t channel, contrary to experiment. The t -channel $M = \frac{3}{2}$ amplitudes are provided by the absorptive corrections in Eq. (A1). In the Williams model these corrections give rise to nonvanishing s -channel amplitudes $A_{(1/2)(-1/2)}^{(3/2)(1/2)}$ and $A_{(-1/2)(1/2)}^{(-1/2)(1/2)}$ at $t' = 0$; these amplitudes satisfy angular momentum conservation but would vanish in Born approximation. For small t' , the s -channel Born terms for these amplitudes have the approximate behavior

$$A_{(1/2)(-1/2)}^{(3/2)(1/2)}(s\text{-ch Born}) \approx C_{(3/2)} \left[\frac{t'}{-t + m_{\pi^+}^2} \right] e^{Bt'} F(M_{p\pi^+}), \quad (\text{A4a})$$

$$A_{(-1/2)(1/2)}^{(-1/2)(1/2)}(s\text{-ch Born}) \approx C_{(-1/2)} \left[\frac{t'}{-t + m_{\pi^+}^2} \right] e^{Bt'} F(M_{p\pi^+}), \quad (\text{A4b})$$

where C_M are slowly varying functions of t and $M_{p\pi^+}$

which can be calculated from the crossing matrices. At high energies, the Williams model gives the s -channel absorptive corrections in Eq. (A1) as

$$A_{(1/2)(-1/2)}^{(3/2)(1/2)}(s\text{-ch abs}) \approx C_{(3/2)} e^{Bt'} F(M_{p\pi^+}), \quad (\text{A5a})$$

$$A_{(-1/2)(1/2)}^{(-1/2)(1/2)}(s\text{-ch abs}) \approx C_{(-1/2)} e^{Bt'} F(M_{p\pi^+}). \quad (\text{A5b})$$

Our parametrization is a little more flexible and amounts to the ansatz

$$A_{\lambda_n \lambda_t}^{M \lambda_b}(\text{abs}) - \xi A_{-\lambda_n - \lambda_t}^{M \lambda_b}(\text{abs}) = e^{B\xi t'} S C_M F(M_{p\pi^+}), \quad (\text{A6})$$

where $B_\xi = B_\pm$ are slope parameters for the natural- and unnatural-parity exchange amplitudes defined by Eq. (A3), and S is a scale parameter. The helicities M and λ_b refer to t -channel helicities while λ'_n and λ'_t refer to s -channel helicities; Eq. (A6) applies specifically to amplitudes with $(M, \lambda_b, \lambda'_n, \lambda'_t) = (\frac{3}{2}, \frac{1}{2}, \frac{1}{2}, -\frac{1}{2})$ and $(-\frac{3}{2}, \frac{1}{2}, -\frac{1}{2}, \frac{1}{2})$ only. For $t' = 0$ the second term on the LHS of Eq. (A6) vanishes, and with $S = 1$ the ansatz is equivalent to Eq. (A5). Finally, in order to satisfy the Pauli principle, the combined amplitudes in Eq. (A1) are folded about 90° using Eq. (29):

$$A_{\lambda_n \lambda_t}^{M \lambda_b}(\Theta_\Delta)_{\text{sym}} = A_{\lambda_n \lambda_t}^{M \lambda_b}(\Theta_\Delta) + (-1)^{M + \lambda_n + \lambda_b + \lambda_t} A_{\lambda_n \lambda_b}^{M \lambda_t}(\pi - \Theta_\Delta). \quad (\text{A7})$$

The fitted parameters G , S , B , B_+ , and B_- are listed in Table IV for 1.18, 1.47, 1.71, 1.98, and 6 GeV/ c . The fits used the DME's ρ_{11} , ρ_{33} , ρ_{31} , and ρ_{3-1} integrated over the Δ^{++} band, given by 1.15–1.34 GeV (6 GeV/ c), 1.18–1.28 GeV (1.47, 1.71, and 1.98 GeV/ c), and 1.16–1.20 GeV (1.18 GeV/ c). The crossing factors $C_{3/2}$ and $C_{-1/2}$ were evaluated at the center of each mass interval and were not explicitly averaged over $M_{p\pi^+}$. We find reasonable continuity in the fitted parameters with energy. However, as might be expected, the fit quality is poorer at the lower energies than for the 3–12-GeV/ c data.

APPENDIX B

In this appendix we consider interference contributions between $\Delta^{++}n$ and Δ^+p final states [Figs. 4(a) and 4(b)]. These contributions can be calculated using the Wick transformation⁴² and isotopic spin conservation, without reference to any specific Δ -production model. The computations are involved and we only sketch the derivation here. Our numerical calculations indicate that the single spin correlations, averaged over the Δ^{++} mass, do not in fact receive significant $\Delta^+-\Delta^{++}$ interference contributions.

Consider a specific $pp \rightarrow \Delta^{++}n$ transition amplitude $W_p = W_p(J, j = \frac{3}{2}, l = 1, L_i, S_i, L_f, S_f)$ in the notation of Eq. (32a). Isotopic spin conservation gives

$$W(pp \rightarrow \Delta^{++}n) = W_p(M_{p\pi^+}), \quad (B1a)$$

$$W(pp \rightarrow \Delta^+p) = \frac{-W_p}{3}(M_{n\pi^+}). \quad (B1b)$$

Combining Eqs. (30) and (35), the associated helicity amplitudes for this single wave take the form

$$T_{\lambda_n \lambda_t}^{\lambda_p \lambda_b}(pp \rightarrow \Delta^{++}n) = W_p \sum_M D_{\lambda_b M - \lambda_n}^{*J}(0, \Theta_\Delta, \phi) d_{M \lambda_p}^j(\theta) F_{jl}(M_{p\pi^+}) g_{j l \lambda_p} C_{M \lambda_b \lambda_n \lambda_t}^{J L_i S_i L_f S_f}, \quad (B2a)$$

$$T_{\lambda_n \lambda_t}^{\lambda_p \lambda_b}(pp \rightarrow \Delta^+p) = -\frac{W_p}{3} \sum_{M, M', \lambda'_n, \lambda'_p} D_{\lambda_b M' - \lambda_n}^{*J}(0, \Theta_\Delta, \phi) D_{M' - \lambda_n M - \lambda'_p}^{*J}(0, \tilde{\Theta}, 0) d_{M \lambda_n}^j(\tilde{\theta}) \times d_{\lambda_n \lambda_n}^{j(1/2)}(\chi_n) d_{\lambda_p \lambda_p}^{j(1/2)}(\chi_p) F_{jl}(M_{n\pi^+}) g_{j l \lambda'_n} C_{M \lambda_b \lambda'_p \lambda_t}^{J L_i S_i L_f S_f} \left[\frac{q_p Q_{p\pi^+}}{q_n Q_{n\pi^+}} \right]^{1/2}. \quad (B2b)$$

Here $j = \frac{3}{2}$, $l = 1$, $\lambda = \lambda_b - \lambda_t$; q_p (q_n) is the proton (neutron) momentum in the $p\pi^+$ ($n\pi^+$) RF; $\tilde{\Theta}$ is the rotation in the three-body plane that takes the z axis from $\hat{p}_{p\pi^+}$ to $\hat{p}_{n\pi^+}$; $\tilde{\theta}$ is the rotation angle in the $n\pi^+$ RF between \hat{p}_n and $\hat{p}_{n\pi^+}$; and χ_n and χ_p are Stapp rotations that ensure consistent helicity axes for λ_p and λ_n in (B2a) and (B2b). Both amplitudes have formally similar dependence on Θ_Δ and ϕ , which specify the orientation of the three-body decay plane. The variables $\tilde{\Theta}$, $\tilde{\theta}$, χ_n , χ_p , and $M_{n\pi^+}$ in Eq. (B2b) are ‘‘internal’’ variables in that they can be reexpressed as functions of $M_{p\pi^+}$ and θ used in Eq. (B2a); $M_{p\pi^+}$ and θ may be regarded as the two independent Dalitz-plot variables. The Jacobian factor $(q_p Q_{p\pi^+} / q_n Q_{n\pi^+})^{1/2}$ in Eq. (B2b) is included to ensure consistency with Eq. (36); it allows expression of the cross section as $d^2\sigma/dM_{p\pi^+} d\cos\theta$ rather than $d\sigma/d\rho$ (ρ being the invariant phase space associated with the Dalitz-plot variables).

We can recast the $pp \rightarrow \Delta^+p$ amplitudes of Eq. (B2b) as a sum over $pp \rightarrow (p\pi^+)n$ isobars of the form of Eq. (B2a). Given an appropriate Breit-Wigner form for $F(M_{n\pi^+})$, the ‘‘reflected’’ waves can be written as

$$W(J, j', l', L_i, S_i, L'_f, S'_f) = -\frac{W_p}{3} R_{j' l' L'_f S'_f}^{j l L_f S_f}(M_{p\pi^+}). \quad (B3)$$

The reflection coefficients R are complex functions of $M_{p\pi^+}$ and can be calculated by comparing (B2b) and the general form of (B2a). The amplitude on the LHS of Eq. (B3) is the $M_{p\pi^+}$ -dependent partial wave amplitude for $pp \rightarrow (p\pi^+)n$ as used in Eq. (30a); note that L , L_i , and S_i are the same for the Δ^+p wave and the $(p\pi^+)n$ reflections, but j' , l' , L'_f , and S'_f for the $(p\pi^+)n$ reflections can take all values consistent with parity and angular-momentum conservation.

As an aside, there is inherent ambiguity in the choice of angles χ_n , χ_p , and $\tilde{\theta}$ in Eq. (B2b); an error of 2π in any of these would change the overall phase of the Δ^+p contribution by 180° . We resolve this ambiguity by considering first the reaction $pp \rightarrow pp\pi^0$, which has two possible Δ^+p final states. For this process, the ambiguities are resolved by the Pauli principle, which requires even values of $L+S$ for the final-state protons. We then use isotopic spin conservation to relate the $pp \rightarrow pp\pi^0$ isobar contributions to the desired $pp \rightarrow pn\pi^+$ final states.

We have calculated the reflection matrix as a function of $M_{p\pi^+}$ for the ΔN waves which are expected to be large at 1.18 and 1.47 GeV/ c (e.g., $L_f = 0$ and 1 waves). For kinematical reasons, the relative phase of the Δ^{++} and Δ^+ contributions goes through zero near the center of the Δ^{++} band for all waves (we define the center of the Δ^{++} band as 1.23 GeV at 1.47 GeV/ c , and 1.18 GeV at 1.18 GeV/ c). As a result, $\text{Im}(\Delta^{++}\Delta^{++})$ contributions to the spin correlations average to very nearly zero over the Δ^{++} band, although they give small contributions which oscillate about zero as functions of $M_{p\pi^+}$. For example, we used the pion-exchange parametrization to specify the relative real production waves for $pp \rightarrow \Delta N$, and computed the $\Delta^+-\Delta^{++}$ interference contributions to the SSC's; the values of A_y were less than 2% over all $\cos\Theta_\Delta$, averaged over the Δ^{++} band, and the other SSC's were correspondingly quite small. This result is insensitive to the precise values assumed in the production waves.

We conclude that the relative Breit-Wigner phases of the $\Delta^{++}n$ and Δ^+p final states cannot by themselves explain the large spin correlations observed in the data. Therefore we simply regard the Δ^+p contributions as phenomenological backgrounds in the s , p , and Δ $pp \rightarrow (p\pi^+)n$ isobar configurations; also, we focus on observables averaged over the Δ^{++} band so as to minimize the effect of $\Delta^+-\Delta^{++}$ interferences.

*Present address: University of Arizona, Tucson, AZ 85281.

†Present address: AT&T Information Systems, Denver, CO 80234.

‡Present address: Bell Laboratories, Piscataway, NJ 08854.

§Present address: Kinetic Systems, Lockport, IL 60441.

¹Some recent representative reviews of dibaryon phenomenology include D. V. Bugg, Nucl. Phys. **A416**, 227C (1984); Annu. Rev. Nucl. Part. Sci. **35**, 295 (1985); M. P. Locher, Nucl. Phys. **A416**, 243C (1984); P. Kroll, J. Phys. Paris Colloq. **46**, C2-493 (1985); I. R. Afnan, Nucl. Phys. **A416**, 257C (1984); A. Yokosawa, in *Proceedings of the 6th International Symposium on Polarization Phenomena in Nuclear Physics*, Osaka, Japan, 1985 [J. Phys. Soc. Jpn. Suppl. **55**, (1986)].

²A. B. Wicklund *et al.*, Phys. Rev. D **34**, 19 (1986).

³F. Shimizu *et al.*, Nucl. Phys. **A386**, 571 (1982).

⁴D. V. Bugg *et al.*, Phys. Rev. **133**, B1017 (1964) (1.66 GeV/c); A. M. Eisner, E. L. Hart, R. I. Louttit, and T. W. Morris, *ibid.* **138**, B670 (1964) (2.23 GeV/c); R. L. McIlwain *et al.*, Phys. Rev. **127**, 239 (1962) (1.17 GeV/c); S. Focardi *et al.*, Nuovo Cimento **39**, 405 (1965) (0.98 GeV/c); B. Baldoni *et al.*, Nuovo Cimento **26**, 1376 (1962) (1.17 GeV/c); M. G. Mescheryakov *et al.*, Zh. Eksp. Teor. Fiz. **28**, 45 (1957) [Sov. Phys. JETP **4**, 60 (1957)] (1.17 GeV/c); V. P. Dzhelepov *et al.*, Dok. Akad. Nauk. SSSR **104**, 380 (1955) (1.19–1.27 GeV/c); B. S. Neganov *et al.*, Zh. Eksp. Teor. Fiz. **32**, 1265 (1957) [Sov. Phys. JETP **5**, 1033 (1957)] (1.18 GeV/c, 1.29 GeV/c).

⁵A. D. Hancock *et al.*, Phys. Rev. C **27**, 2742 (1983).

⁶C. L. Hollas *et al.*, Phys. Rev. Lett. **55**, 29 (1985).

⁷G. Glass *et al.*, Phys. Lett. **129**, 27 (1983).

⁸T. S. Bhatia *et al.*, Phys. Rev. C **28**, 2071 (1983).

⁹R. Shypit *et al.*, Phys. Lett. **124B**, 314 (1983); C. E. Waltham *et al.*, Nucl. Phys. **A433**, 649 (1985).

¹⁰I. Duck and E. Umland, Phys. Lett. **96B**, 230 (1980).

¹¹P. J. Mulders, A. T. Aerts, and J. J. de Swart, Phys. Rev. D **21**, 2653 (1980); P. J. Mulders, *ibid.* **25**, 1269 (1982).

¹²B. J. Edwards, Phys. Rev. D **23**, 1978 (1981).

¹³R. Bhandari, R. A. Arndt, L. D. Roper, and B. J. Verwest, Phys. Rev. Lett. **46**, 1111 (1981).

¹⁴A. Konig and P. Kroll, Nucl. Phys. **A356**, 345 (1981); W. Jauch, A. Konig, and P. Kroll, Phys. Lett. **143B**, 509 (1984).

¹⁵W. M. Kloet and R. R. Silbar, Nucl. Phys. **A338**, 281 (1980); **A338**, 317 (1980); **A364**, 346 (1980).

¹⁶W. M. Kloet, T. A. Tjon, and R. R. Silbar, Phys. Lett. **99B**, 80 (1981).

¹⁷J. Dubach, W. M. Kloet, and R. R. Silbar, J. Phys. G **8**, 475 (1982).

¹⁸J. Dubach, W. M. Kloet, A. Cass, and R. R. Silbar, Phys. Lett. **106B**, 29 (1981).

¹⁹B. J. Verwest, Phys. Lett. **83B**, 161 (1979); Phys. Rev. C **25**, 482 (1982).

²⁰A. M. Green and M. E. Sainio, J. Phys. G **5**, 503 (1979).

²¹E. L. Lomon, Phys. Rev. D **26**, 576 (1982); **31**, 1746 (1985).

²²T. Ueda, Phys. Lett. **74B**, 123 (1978); **79B**, 487 (1978); M. Araki, Y. Koike, and T. Ueda, Prog. Theor. Phys. **63**, 335 (1980); **63**, 2133 (1980); M. Araki and T. Ueda, Nucl. Phys. **A379**, 449 (1982).

²³J. A. Niskanen, Phys. Lett. **112B**, 17 (1982).

²⁴R. A. Arndt *et al.*, Phys. Rev. D **28**, 97 (1983).

²⁵J. Bystricky, C. Lechanoine-Leluc, and F. Lehar, Saclay Report No. DPhPE 82-12, 1984 (unpublished); Saclay Report No. DPhPE 86-13 (unpublished).

²⁶N. Hoshizaki, Prog. Theor. Phys. **60**, 1796 (1978); **61**, 129 (1979).

²⁷R. Dubois *et al.*, Nucl. Phys. **A377**, 554 (1982).

²⁸The total inelastic cross section for a coupled-channel Breit-Wigner resonance is given by

$$\sigma(pp \rightarrow \text{inel}) = \frac{2\pi}{k^2} (2J+1) \times (1-x),$$

where $x = \Gamma_{pp} / \Gamma_{\text{tot}}$. For example, for $x = 0.2$, this yields an inelastic cross section of 7.3 mb at the peak of the 3F_3 “resonance” (taking $M_R \sim 2.24$ GeV). Only the $NN\pi$ and $\Delta\pi$ channels have large enough cross sections to satisfy this constraint.

²⁹S. Mandelstam, Proc. R. Soc. London **A244**, 491 (1958).

³⁰Notation: ${}^{2S+1}L_{2J+1} \rightarrow {}^{2S'+1}L'_{2J+1}$, where $S(S')$ and $L(L')$ refer to the $pp(\Delta N)$ -channel total spin and orbital momentum, and J to the total angular momentum.

³¹R. H. Dalitz and R. G. Moorhouse, Proc. R. Soc. London **A318**, 279 (1970). For specific parametrizations with non-resonant background effects, see P. W. Coulter, Phys. Rev. Lett. **29**, 450 (1972); D. E. Novoseller, Nucl. Phys. **B176**, 153 (1980); D. Cohen *et al.*, Phys. Rev. D **22**, 2595 (1980).

³²These scenarios for the behavior of $\delta_{\Delta N}$ are discussed in more detail by B. J. Edwards and G. H. Thomas, Phys. Rev. D **22**, 2772 (1980).

³³M. W. Arenton *et al.*, Phys. Rev. D **25**, 22 (1982); **25**, 2241 (1982); **28**, 657 (1983); S. Kooijman *et al.*, Phys. Rev. Lett. **45**, 316 (1980).

³⁴I. Ambats *et al.*, Nucl. Instrum. Methods **174**, 427 (1980).

³⁵M. M. Calkin, Rice University thesis, 1983 (unpublished).

³⁶M. G. Albrow *et al.*, Nucl. Phys. **B23**, 445 (1970); J. P. Auer *et al.*, Phys. Lett. **67B**, 113 (1977); Phys. Rev. Lett. **41**, 354 (1978); P. P. Bevington *et al.*, *ibid.* **41**, 384 (1978); B. A. Bell *et al.*, Phys. Lett. **94B**, 310 (1980); C. Cozzika *et al.*, Phys. Rev. **164**, 1672 (1967); R. Diebold *et al.*, Phys. Rev. Lett. **35**, 632 (1975); A. Lin *et al.*, Phys. Lett. **74B**, 273 (1978); M. W. McNaughton *et al.*, Phys. Rev. C **23**, 838 (1981); **23**, 1128 (1981); M. W. McNaughton and P. Chamberlin, *ibid.* **24**, 1778 (1981).

³⁷H. Spinka *et al.*, Nucl. Instrum. Methods **211**, 239 (1983).

³⁸M. D. Corcoran *et al.*, Phys. Lett. **120B**, 309 (1983).

³⁹F. T. Solmitz, Annu. Rev. Nucl. Sci. **14**, 375 (1964).

⁴⁰J. L. Petersen, Phys. Rep. **2C**, 155 (1971).

⁴¹P. K. Williams, Phys. Rev. D **1**, 1312 (1970).

⁴²G. C. Wick, Ann. Phys. **18**, 65 (1962).

⁴³J. Hudomalj-Gabitzch *et al.*, Phys. Rev. C **18**, 2666 (1978).

⁴⁴A. Saha *et al.*, Phys. Rev. Lett. **51**, 759 (1983).

⁴⁵By convention the production normal used to define $A_y(p, p \rightarrow \pi^+ d)$ is given by $\hat{\mathbf{p}}_b \times \hat{\mathbf{p}}_{\pi^+}$ with the beam proton polarized. This normal coincides with the production normal $\mathbf{p}_b \times \mathbf{p}_{p\pi^+}$ which we have used to define $A_y(pp \rightarrow p\pi^+ n)$ in the kinematical limit of Eq. (39).

⁴⁶J. H. Gruben and B. J. Verwest, Phys. Rev. C **28**, 836 (1983).

⁴⁷The 3S_1 proton-neutron phase shift varies from 180° at threshold to $\sim 90^\circ$ at 15 MeV; this corresponds to $\Delta \cos\theta \sim 0.3$ or $\Delta M_{p\pi^+} \sim 20$ MeV. See P. Doleschall *et al.*, Nucl. Phys. **A380**, 72 (1982).

⁴⁸The integrated cross sections of Shimizu *et al.* (Ref. 3) have been corrected for our Δ^{++} mass cuts using the $M_{p\pi^+}$ dependence obtained from this experiment and from Ref. 3.

⁴⁹We verified that we could fit the $P_i\rho_{s1}, P_i\rho_{s-1}$ observables by varying the s isobars. However, it is not possible to get good fits for the ρ_{s1}, ρ_{s-1} observables simultaneously due to the strong $M_{p\pi^+}$ dependence of these moments (cf. Sec. IV B).

⁵⁰To obtain continuous curves in Fig. 19, we used smooth poly-

- nomial fits to the pion-exchange fit parameters of Table IV, and we defined the Δ^{++} band in a continuous fashion. The upper edge of the Δ^{++} band was defined by the kinematic limit or 1.28 GeV, whichever was smaller. The lower limit was defined by the upper limit minus 0.04 GeV, or 1.18 GeV, whichever was smaller.
- ⁵¹E. E. Van Fassen and J. A. Tjon, Phys. Rev. C **28**, 2354 (1983).
- ⁵²M. Lacombe, B. Loiseau, S. Morioka, and R. Vinh. Mau, Orsay Report No. IPNO/TH 84-12, 1984 (unpublished).
- ⁵³The systematic errors were taken to be $\delta a_{MN}^L = 0.015$ for all normalized moments. This implies a smaller systematic error for $A_y = 2(P_y \rho_{11} + P_y \rho_{33})$ than for $P_y \rho_{11}$ or $P_y \rho_{33}$ separately; this is appropriate in that those systematic uncertainties associated with p - Δ interference contributions cancel in A_y . In the fits, the A_y and $P_y \rho_{33}$ moments were used (not $P_y \rho_{11}$).
- ⁵⁴E. Aprile-Giboni *et al.*, Nucl. Phys. **A415**, 365 (1984).
- ⁵⁵G. Glass *et al.*, Phys. Rev. C **31**, 288 (1985).
- ⁵⁶W. B. Tippens *et al.*, in *Few Body Problems in Physics*, edited by B. Zeitnitz (North-Holland, Amsterdam, 1984), Vol. II, p. 17; G. Glass *et al.*, Phys. Rev. Lett. **53**, 1984 (1984).
- ⁵⁷J. Boswell *et al.*, Phys. Rev. C **25**, 2540 (1982); P. M. Heinz *et al.*, Phys. Rev. **167**, 1232 (1968).
- ⁵⁸E. Aprile-Gibone *et al.*, Nucl. Phys. **A431**, 637 (1984).
- ⁵⁹I. P. Auer *et al.*, Phys. Rev. Lett. **51**, 1411 (1983).
- ⁶⁰M. Arik and P. G. Williams, Nucl. Phys. **B136**, 425 (1978).
- ⁶¹D. V. Bugg, J. Phys. G **10**, 717 (1984); Nucl. Phys. **A437**, 534 (1985); **A416**, 227C (1984). For other analyses of $pp \rightarrow \pi^+ d$, see also H. Kamo and W. Watari, Prog. Theor. Phys. **62**, 1035 (1979); H. Kamo, W. Watari, and M. Yonezawa, *ibid.* **64**, 2144 (1980); N. Hiroshige, W. Watari, and M. Yonezawa *ibid.* **68**, 2074 (1982).
- ⁶²J. Hoftiezer *et al.*, Nucl. Phys. **A412**, 273 (1984).